
Frequency-Modulated Continuous-Wave Radar for Tracing Discontinuities on Transmission Lines

Björn Niclas Möhring (ORCID: 0000-0001-7691-2012). *Frequency-Modulated Continuous-Wave Radar for Tracing Discontinuities on Transmission Lines*. Dissertation. Technische Universität München, München, Deutschland, 2023.

©2023 Björn Niclas Möhring



Technische Universität München
TUM School of Computation, Information and Technology

Frequency-Modulated Continuous-Wave Radar for Tracing Discontinuities on Transmission Lines

Björn Niclas Möhring

Vollständiger Abdruck der von der TUM School of Computation, Information and
Technology der Technischen Universität München zur Erlangung des akademischen
Grades eines

– Doktors der Ingenieurwissenschaften –

genehmigten Dissertation.

Vorsitz: Prof. Dr.-Ing. habil. Dr. h.c. Alexander W. Koch
Prüfer der Dissertation: 1. Prof. Dr.-Ing. Thomas F. Eibert
2. Prof. Dr.-Ing. Madhukar Chandra

Die Dissertation wurde am 28.09.2022 bei der Technischen Universität München
eingereicht und durch die TUM School of Computation, Information and Technology am
16.5.2023 angenommen.

Abstract

A fast chirp frequency-modulated continuous-wave (FMCW) radar is presented for detecting, locating, and tracking static as well as fast varying faults, discontinuities, or bends along transmission lines. This reflectometer in a portable and compact housing is designed for in-field monitoring of car airbag deployment processes at test benches. It is motivated by providing and establishing an additional measurement technique to supplement available airbag test approaches, such as optical and mechanical methods, as well as numerical simulation models. A long-term goal of this work is to fully resolve the still present uncertainties of airbag deployments and gather a complete understanding of this highly dynamic process to improve overall car safety further.

The FMCW radar principle is employed and adopted to a transmission line-based measurement approach, which is associated with the field of frequency-domain reflectometry (FDR), which in turn is strongly related to the popular time-domain reflectometry (TDR). A radio frequency transmission line is directly attached to the surface of a car airbag, functioning as the bend sensor and fold indicator. In conjunction with the FMCW radar principle, this sensing transmission line allows for observing mechanical deformations along the line or even its bend status over time, which can indicate the unfolding behavior of an airbag during deployment.

Challenges arise from the speed of an airbag deployment which typically lasts no longer than 50 ms. Furthermore, it is difficult to reliably detect and accurately locate so-called soft-faults over time. For instance, such soft-faults arise from a bent transmission line, resulting in minor impedance variations only, therefore requiring a large dynamic range. The system concept, hardware realization, and performance specifications of the radar device are introduced. The signal generation is based on direct digital synthesis (DDS) in conjunction with an analog frequency multiplication approach to enhance bandwidth and thereby range resolution. A digital signal generation is chosen due to the needed very agile sweeping capabilities for the airbag monitoring application and due to other advantages over analog signal sources, such as an improved phase noise performance, temperature stability, and immunity against analog drifts or aging problems, as well as very linear sweeping capabilities. In this process, highly linear, fast swept chirp pulses with a duration of microseconds and a large bandwidth of 5.2 GHz are established. Those chirp pulses, which occupy frequencies from lower UHF-band up to C-band, function as the transmitting signal within the radar.

Besides the design of the FMCW radar instrument, the second part of this work deals with the investigation and design of flexible transmission line structures for the airbag

surface. Thereby, a highly flexible stencil-printed coplanar waveguide was fabricated and directly printed on the coarse nylon textile fabric of the airbag. This transmission line offers high mechanical flexibility at the cost of considerable transmission losses. In addition, twisted pair cables out of enameled wire around a dielectric core have been developed and tested for their bend sensitivity. They showed a reasonable response to mechanical deformation; however, severe losses are observed in the designated frequency range.

Laboratory test results of the radar for static and dynamic faults, bends, and discontinuities along transmission lines are presented. Besides, a monostatic FMCW radar setup has been built, and a rapidly moving corner reflector was tracked over time. The results demonstrate effectiveness, versatility, and fine-ranging capabilities on the order of 2 cm together with high sensitivity for weakly reflective targets and soft-faults in very short range. Furthermore, not just static but also time-varying faults in the form of a loose match termination or manually produced discontinuities by hammer hits were accurately tracked in very short range due to the fast sweeping capabilities of the device.

Zusammenfassung

Ein schnell frequenzmoduliertes Dauerstrichradar (FMCW) zur Erkennung, Lokalisierung und zeitlichen Beobachtung von statischen sowie schnell veränderlichen Störstellen, Diskontinuitäten oder Knicken entlang von Hochfrequenzleitungen wird vorgestellt. Dieses tragbare und kompakte Reflektometer wurde für die Beobachtung und Analyse von Airbag-Entfaltungsvorgängen an Prüfständen konzipiert. Motiviert ist diese Arbeit durch das Vorhaben, eine zusätzliche Messtechnik im Entwicklungsprozess von Airbags als Ergänzung zu den bereits verfügbaren Airbag-Testverfahren, wie z.B. optische und mechanische Methoden, oder numerische Simulationsmodelle zu entwickeln und zu etablieren. Dabei ist ein langfristiges Ziel dieses Projektes, die immer noch vorhandenen Fehler, Unsicherheiten und die fehlende Reproduzierbarkeit bei der Entfaltung von Airbags vollständig zu beseitigen und ein umfassendes Verständnis dieses hochdynamischen Prozesses zu erlangen, um die Fahrzeugsicherheit insgesamt weiter zu verbessern. Um der hohen Geschwindigkeit von Airbag-Entfaltungen gerecht zu werden, muss die Wiederholrate der frequenzmodulierten Rampen des Sendesignals entsprechend hoch sein.

Zu diesem Zweck wird das Prinzip des FMCW-Radars auf Hochfrequenzleitungen angewandt. Dabei konzentriert sich diese Arbeit auf die Anwendung der Frequenzbereichsreflektometrie (FDR), die eng mit der bekannten Zeitbereichsreflektometrie (TDR) verwandt ist. Eine flexible Hochfrequenzleitung wird dabei direkt auf der Oberfläche eines Airbags angebracht und fungiert somit als Biegesensor und Störstellenindikator. In Verbindung mit dem FMCW-Radarprinzip ermöglicht diese Sensorleitung die zeitliche Beobachtung mechanischer Verformungen entlang der Leitung und soll zudem sogar Aufschluss über ihren Biegezustand geben, welcher während der Faltung und Entfaltung auftritt. Mittels dieser Information lässt sich dann auf das zeitliche und räumliche Entfaltungsverhalten eines Airbags nach der Zündung schließen.

Da der Airbag-Entfaltungsvorgang in der Regel nicht länger als 50 ms dauert, ergeben sich aus dieser hohen Ablaufgeschwindigkeit gewisse Herausforderungen für die Messtechnik. Außerdem ist es schwierig, kleine Störstellen und Knicke entlang einer Leitung zuverlässig zu erkennen und genau zu lokalisieren. Diese entstehen zum Beispiel durch eine leicht gebogene Leitung, die nur geringe, lokale Impedanzveränderungen verursacht und somit einen großen Dynamikbereich des Sendesignals erfordert.

Das Systemkonzept, die Hardwareumsetzung und die Leistungsmerkmale des entwickelten Radargeräts werden vorgestellt. Die Signalerzeugung basiert auf der direkten digitalen Synthese (DDS) in Verbindung mit einem analogen Frequenzmultiplikationsansatz, um

die Bandbreite und damit die Ortsauflösung zu erhöhen. Die digitale Signalerzeugung wurde gewählt, weil für die geplante Anwendung der Airbag-Analyse eine sehr hohe Wiederholrate der frequenzmodulierten Rampen des Sendesignals benötigt wird und weil diese zudem weitere Vorteile gegenüber analogen Signalquellen bietet. Diese umfassen beispielsweise ein verbessertes Phasenrauschverhalten, Temperaturstabilität und Immunität gegen analoge Drifts oder Alterungsprobleme sowie die Möglichkeit, sehr linear frequenzmodulierte Signale zu generieren. Das entwickelte Radargerät erzeugt dabei hochlineare, schnell modulierte Chirp-Pulse mit einer Dauer von Mikrosekunden und einer Bandbreite von 5,2 GHz. Die untere Grenzfrequenz des Sendesignals liegt dabei im unteren UHF-Band.

Neben dem Entwurf und der Realisierung des FMCW-Radargerätes befasst sich der zweite Teil dieser Arbeit mit der Untersuchung und der Entwicklung flexibler Hochfrequenzleitungsstrukturen für das Airbaggewebe. Dabei wurde eine hochflexible koplanare Mikrostreifenleitung aus leitfähiger Tinte entwickelt, die mittels des Schablonendrucks direkt auf das grobe Nylongewebe des Airbags gedruckt wird. Diese sehr kostengünstige Leitung bietet eine hohe mechanische Flexibilität und Elastizität auf Kosten von erheblichen Übertragungsverlusten. Außerdem wurden verdrehte Zweidrahtleitungen, sogenannte Twisted-Pair Leitungen aus Lackdraht entwickelt, die um einen dielektrischen Kern gewickelt werden. Diese Leitungen wurden auch auf ihre Biegeempfindlichkeit getestet. Dabei zeigte sich eine gut messbare elektrische Reaktion auf mechanische Verformung, allerdings sind im gegebenen Frequenzbereich erhebliche Übertragungsverluste zu verzeichnen.

Verschiedene Messergebnisse des entwickelten Radars für statische und dynamische Störstellen, Knicke und Diskontinuitäten entlang von Hochfrequenzleitungen werden vorgestellt. Darüber hinaus wurde mittels des entwickelten Reflektometers ein monostatischer FMCW-Radar-Aufbau erstellt mittels dessen sich ein im Nahbereich schnell bewegender Winkelreflektor zeitlich verfolgt werden kann. Die Ergebnisse zeigen die Effektivität, die Vielseitigkeit und die genaue Ortsauflösung des Gerätes in der Größenordnung von 2 cm sowie die hohe Empfindlichkeit für schwach reflektierende Ziele und sogenannte Soft-Faults in sehr kurzer Entfernung. Zudem wurden nicht nur statische, sondern auch zeitlich veränderliche Störstellen aufgrund der hohen Wiederholrate des Sendesignals des Gerätes in sehr kurzer Entfernung genau lokalisiert und quantifiziert. Dabei handelt es sich beispielsweise um einen manuell gelockerten idealen Leitungsabschluss oder plötzlich auftretende Diskontinuitäten entlang einer Leitung, die durch Hammerschläge erzeugt wurden.

Contents

1	Introduction	1
1.1	Review of Microwave Reflectometry Techniques	1
1.1.1	Time-Domain Reflectometry	2
1.1.2	Frequency-Domain Reflectometry	4
1.2	Industrial Monitoring Usage: Airbag Deployment	6
1.3	Problem Statement	8
1.4	Contributions, Scope, and Objective of the Thesis	9
1.5	Outline of the Thesis	10
2	Theoretical Background	13
2.1	FMCW Radar Measurement Principle	13
2.1.1	Analytic Description of the FMCW Principle	17
2.1.2	Fast Chirp FMCW Radar Concept	21
2.2	Electromagnetic Field Theory and TEM Waves	22
2.2.1	Maxwell's Equations and Constitutive Relations	23
2.2.2	Skin Effect and Boundary Conditions	25
2.2.3	Helmholtz Equation and Plane Wave Solution	27
2.3	Transmission Line Theory	28
2.3.1	Derivation of Telegrapher's Equations	29
2.3.2	Reflection and Transmission at Discontinuities	32
2.4	Two-Port Scattering Parameters	34
3	FMCW Reflectometer Instrumentation	37
3.1	Application, Approach, and System Requirements	37
3.1.1	Measurement Approach	38
3.1.2	System Requirements	39
3.2	Frequency Synthesis and Multiplication Approach	41
3.2.1	Signal Generation in FMCW Radar	41
3.2.2	Digital Signal Generation	42
3.2.3	Frequency Multiplier Chain	43
3.2.4	Additional Solutions for Bandwidth Extension	49
3.3	FMCW System Concept and Hardware Realization	53
3.3.1	System Concept	53
3.3.2	Hardware Realization	56

3.3.3	Lower Level of Instrument: DC Supply Unit	56
3.3.4	Upper Level of Instrument: RF Components	58
3.4	System Specifications and TX Signal Quality	62
3.5	Chapter Summary	67
4	Sensing Transmission Line	69
4.1	Requirements for Sensing Transmission Line	69
4.2	Airbag Textile Substrate	71
4.3	Flexible Printed Coplanar Waveguide on Airbag	72
4.3.1	Overview of Printed Electronics	74
4.3.2	CPW Design and Stencil Printing Process	75
4.3.3	Numerical Simulation Model in CST	82
4.3.4	VNA Measurement Setup and Results	82
4.4	Twisted-Pair Cable out of Enameled Wire	86
4.4.1	TPC Prototype with Dielectric Core	86
4.4.2	VNA Measurement Results of TPC	88
4.5	Chapter Summary	91
5	Measurement Results	93
5.1	Static Transmission Lines in Laboratory	93
5.1.1	Transmission Lines with Match Termination	94
5.1.2	Transmission Lines with Bend Location	98
5.2	Dynamic Discontinuities along Transmission Line	101
5.2.1	Loose Match Termination	101
5.2.2	Manually Produced Faults by Hammer Hits	104
5.3	Monostatic FMCW Radar Setup	107
5.4	Chapter Summary	111
6	Conclusions and Outlook	113
6.1	Conclusion	113
6.2	Outlook and Future Research	115
	List of Symbols	117
	Glossary of Abbreviations and Acronyms	121
	Bibliography	123
	Publications by the Author	137
	List of Supervised Student Projects	139

Acknowledgment

First and foremost, I would like to thank everyone who helped and supported me during my research and in the completion of this project and thesis.

This dissertation reflects parts of my work accomplished as a research associate at the Chair of High-Frequency Engineering (HFT) of the Technical University of Munich (TUM) as part of a cooperation project of the Ingolstadt Institute of TUM (INI.TUM), a cooperation between TUM and the AUDI AG in Ingolstadt.

I would like to thank my supervisor Prof. Dr.-Ing. Thomas F. Eibert for providing me the opportunity to conduct this work, for his support, guidance, and the freedom he granted me in my work. Furthermore, I am grateful to Prof. Dr.-Ing. Madhukar Chandra for serving as a second examiner and to Prof. Dr.-Ing. habil. Dr. h.c. Alexander W. Koch for chairing the examination committee.

Besides, I am very thankful to my mentor and supervisor Dr.-Ing. Uwe Siart for guiding me throughout the last years, for his valuable support, expertise, and friendly advice.

I am very grateful to the AUDI AG for funding this project and for giving me the opportunity to conduct this work. A special thanks goes out to my supervisors from the AUDI AG, Sebastian Schweizer, Dr. techn. Harald Schluder, and Tim Schießer.

Additionally, I would like to thank Dr. rer. nat. Philipp Rinklin and Prof. Dr. rer. nat. Bernhard Wolfrum from the Neuroelectronics Group of TUM for supporting me in the field of printed electronics and manufacturing prototypes.

I would like to extend my gratitude to Thomas Mittereder and the workshop from the HFT for supporting me in various electronic, mechanical, and organizational issues. Last but not least, I would like to thank all current and former colleagues, fellow doctoral candidates, and students from the HFT and from the AUDI AG who supported and accompanied me during these exciting past years.

Munich, Summer 2023

Björn Möhring

Introduction

Reflectometry is a measurement principle that employs waves to detect, localize, or even characterize known or unknown objects, materials, or interfaces. This method is based on the reception and analysis of reflected or scattered echoes from those objects or boundary surfaces. Reflectometry methods are widely used in research and industry for plenty of applications. Those methods can be further subcategorized regarding the employed radiation or wave type. For instance, reflectometry can be performed with acoustic waves [Teele and Teele 1984], electromagnetic waves, up to X-rays, or even neutron beams [Zhou and Chen 1995].

However, electromagnetic wave reflectometry is the most common, which in turn can be divided into microwave/radio frequency (RF) reflectometry or optical reflectometry [Gilgen et al. 1989], depending on the frequency range used.

The famous and widespread radar principle [Hülsmeier 1904] and microwave reflectometry are strongly related. Radar and reflectometry methods both work on the same principle [Schiek 1999]. Thereby, radar methods employ unguided electromagnetic waves in free space with frequencies occupying the IEEE radar bands according to [IEEE 2020]. In contrast to radar, most microwave reflectometry methods use guided waves on transmission lines or cables [Furse et al. 2006].

1.1 Review of Microwave Reflectometry Techniques

Commonly, microwave reflectometers are realized as single-ended (one-port) setups. A waveguide like a cable, wire, or transmission line is connected to such a device, here denoted as transmission line under test (TLUT). Thereby, a known high-frequency signal of modest power is fed into the TLUT. Transmission line theory can be used to understand this measurement technique.

At discontinuities, inhomogeneities, faults, anomalies, material transitions, or other imperfections along the TLUT, a part of the signal is reflected back to the source due to

the local change in material or geometrical properties. This results in a local impedance mismatch. The remainder of the signal travels further along the TLUT. By receiving and analyzing the reflected echo, the distance, and the extent, as well as possible further information about the fault can be retrieved, where in particular the exact knowledge of the propagation velocity along the TLUT is important. Depending on the application and the type of TLUT, the acquired characteristics of one or more received echos can indicate or imply specific properties like attenuation or propagation characteristics [Furse et al. 2003, 2006; Furse et al. 2021; Hiebel 2016].

Therefore, this versatile measurement principle is utilized in various applications in research and industry, primarily for monitoring, diagnosis, and fault location purposes [Cataldo and De Benedetto 2011]. Among others, those applications comprise measuring soil water content and electrical conductivity [Evet 2003; Jones et al. 2002], level sensing of liquids in tanks [Nemarich 2001], evaluating burn injuries of human skin [Gao and Zoughi 2017], vector network analysis (VNA) [Hiebel 2016; Schiek 1999; Vanhamme 1990], or the measurement of permittivity or permeability of materials [Nicolson and Ross 1970]. However, the most common usage of microwave reflectometry is the detection, location, and identification of faults on cables, wires, or transmission lines [Cataldo and De Benedetto 2011; Furse et al. 2021]. This is also known as distance-to-fault (DTF) measurement and more colloquial as cable testing or even cable radar [Thomas 2006].

Microwave reflectometry can be distinguished and, as common, further subcategorized into time-domain reflectometry (TDR) and frequency-domain reflectometry (FDR). Both TDR and FDR are strongly related and interconvertible since they are based on the same principle. They are both used for similar purposes but distinguish in their hardware realization, general setup, and the employed transmitting (TX) signal. For instance, TDR is working in the time-domain, with commonly a fast step function as the input signal, acquiring the step response, and the processing of the echoes is conventionally done in the time-domain.

On the contrary, FDR operates and analyzes changes in the frequency-domain with TX signals linearly swept over a designated bandwidth. FDR results aggregate over time by obtaining the steady-state amplitude and phase information at discrete frequency samples.

Further combinations of both TDR and FDR methods as well as enhancements or modifications of either of those methods also exist [Cataldo and De Benedetto 2011; Furse et al. 2003; Shin et al. 2005]. Although highly related, either technique offers specific advantages over the other, which can be exploited for particular applications.

1.1.1 Time-Domain Reflectometry

TDR has been used since the 1930s to test cables and locate faults on wires by measuring its step response, which can be converted into the impulse response [Nemarich 2001]. Thereby, TDR employs short voltage step pulses in the time-domain and injects them into the TLUT. From a hardware point of view, a fast rise time pulse generator in the

picosecond range and a fast oscilloscope are needed to perform precise measurements together with an accurate synchronization of both devices. The accuracy and resolution of TDR depend on the rise and fall time and also on the width of the voltage step or pulse of the TX signal [Furse et al. 2003]. In general, traditional TDR needs multiple-shot operation for very accurate results. A possible single-shot operation results in reduced overall signal energy. In this process, the TX signal and received echoes from possible discontinuities are added, displayed, and monitored by an oscilloscope in the time-domain [Strickland 1970]. With TDR, the faults' locations and their nature, for instance, resistive, inductive, or capacitive, can be detected [Strickland 1970; Thomas 2006]. However, TDR results can also be precisely sampled and processed with modern digital signal processing (DSP) techniques for filtering, transformation, and other processing purposes.

Applications of and research on TDR are reported, for instance, in [Furse and Haupt 2001; Furse et al. 2006; Furse et al. 2021; Griffiths et al. 2006; Lo and Furse 2005; Mackay and Penstone 1974; Pan et al. 2002; Paulter 2001; Sharma et al. 2007; Smith et al. 2005]. Thereby, enhancements and modifications of TDR like spectral TDR [Sharma et al. 2007], spread-spectrum TDR [Smith et al. 2005], and noise-domain reflectometry [Lo and Furse 2005] are suggested.

Despite its long history and broad usage, TDR also comes with certain limitations and potential for improvement. In order to perform precise measurements, expensive and precise hardware is needed, capable of generating and sampling a clean and yet fast-rising pulse with little distortions, which is challenging to realize in practice [Furse et al. 2003; Shin et al. 2005].

Furthermore, conventional TDR has limited measurement capabilities and sensitivity in the RF domain due to the relatively small portion of high-frequency energy in the employed TX step function. The spectral content of the TX pulses is spread unevenly across a wide frequency range, and its energy is mainly concentrated at lower frequencies near direct current (DC), which results in an adverse spectral efficiency [Shin et al. 2005]. Consequently, TDR is less sensitive to changes in the RF domain and more sensitive to changes in lumped-DC characteristics, which is why TDR is sometimes referred to as a DC technique [Shin et al. 2005; Thomas 2006]. This results in a limited sensitivity when faults or discontinuities of a cable are somewhat responsive and sensitive to changes at higher than lower frequencies.

Hard faults on cables like open or short circuits result in significant impedance mismatch, and large resulting reflection coefficients, which are easy to detect and locate [Paulter 2001; Thomas 2006]. However, challenges arise in the location of so-called soft-faults like small discontinuities or anomalies, frays, chafes, damaged insulation, or bends along the TLUT. Those soft-faults can get lost easily in the noise floor due to their low reflective profile. Additionally, all reflectometry methods have difficulties measuring and detecting faults whose impedance variation is rather continuous than instantaneous, which is often the case [Griffiths et al. 2006; Zhang et al. 2011].

The detection of soft-faults is a research topic and reported, for instance, in [Dubey et al. 2021; Furse et al. 2006; Griffiths et al. 2006; Paulter 2001; Shin et al. 2005; Smith et al. 2005; Zhang et al. 2011].

Besides detecting soft-faults, TDR has problems detecting multiple and complex faults or discontinuities, especially beyond a first significant fault due to the typical step response at this initial fault location. This makes it hard to detect, analyze, and especially separate or read out these multiple faults in the time-domain [Pan et al. 2002; Shin et al. 2005; Thomas 2006]. The fact that the receiving (RX) signal of TDR contains multiple reflections and their respective superpositions together with ambient noise makes it hard to find a sharp and precise discontinuity location of each respective fault [Lee et al. 2013].

Albeit, not only does the magnitude of a fault matter, but also its physical length along the TLUT. In the case of an elongated fault, reflection occurs on both ends of the fault, which helps to detect and analyze it further [Griffiths et al. 2006].

Beyond that, TDR suffers under the standard blind spot handicap, which takes place during the launch of the TX pulse. In this case, the RX signal occurs right within the rise time of the TX signal and so impairs the detection capabilities. The blind spot length correlates with the pulse width, which in turn settles the accuracy, energy, and maximum possible TLUT lengths. Due to this blind spot, it is challenging to locate faults within the first few centimeters or meters of a TLUT, depending on the pulse width. A simple but effective remedy is just to add additional length to the TLUT [Furse et al. 2006].

The necessary, multiple-shot operation of TDR makes it difficult to resolve dynamic targets instead of static targets. The achievable accuracy of TDR depends on many factors. Still, in [Smith et al. 2005], a maximum error of 3 cm with a minimal cable length of 3.5 m due to overlap of the initial peaks is realized, while [Furse et al. 2006] reports over an error of minimum 2 inches, which corresponds to a length of 5.08 cm. In [Shin et al. 2005], an accuracy error of at best 8 cm is achieved with a combined time- and frequency-domain reflectometry technique.

1.1.2 Frequency-Domain Reflectometry

Traditional pulse radar and the TDR principle are strongly related, whereas, frequency-modulated continuous-wave (FMCW) radar or VNAs operate on the FDR principle. Furthermore, the FDR principle can be further sub-divided into phase-detection FDR [Furse et al. 2003], standing-wave reflectometry [Furse et al. 2021], mixed-signal reflectometry [Furse et al. 2006; Tsai et al. 2005], and FMCW reflectometry [Furse et al. 2003; Furse et al. 2021], which works on the same principle as FMCW radar [Stove 1992].

Apart from radar, another important usage of FDR is the network analysis performed by VNAs to determine microwave characteristics of devices under test (DUT) [Hiebel 2016; Schiek 1999]. Thereby, the standard error correction and calibration techniques of VNAs can also be used in other FDR applications. FMCW reflectometry can be considered a simple one-port VNA setup that only requires the magnitude and not the phase information of an RX signal for range measurements. However, if complex transfer functions are of interest, a one-port FMCW reflectometry system setup can be adapted to homodyne VNA arrangements by employing additional hardware [Schiek 1999].

Among other techniques, FDR has been developed to overcome the limitations of TDR [Lee et al. 2013]. Research on and applications of FDR can be found, for instance, in [Furse et al. 2003; Naik et al. 2006; Zhang et al. 2011], the explicit employment of FMCW reflectometry to transmission lines has been demonstrated in [Bao 2015; Bao et al. 2011, 2013, 2014; Möhring et al. 2022; Möhring et al. 2021].

In contrast to TDR, FDR techniques employ linearly or stepped frequency-modulated sine waves as the TX signal, which is fed into the TLUT. Often, a ramp/sawtooth or triangular modulation scheme is used for this. At occurring discontinuities along the TLUT, parts of this TX signal are reflected back, constituting the RX signal. Separating the TX from the RX signal using directional couplers and multiplying these two signals within a mixing process, frequency shifts containing the range or potential velocity information of the respective faults along the TLUT are acquired. A fast Fourier transform (FFT) converts this data from frequency-domain into time-domain or to a range scale together with the signal propagation velocity. In FDR, the fault locations are represented by individual peaks in a frequency spectrum whose heights correlate with the magnitude of the reflections [Furse et al. 2003; Furse et al. 2021; Griffiths et al. 2006].

This approach in frequency-domain is accompanied by certain advantages when compared to TDR methods. The electric and hardware architecture of FDR systems is often considered more simple, and the peak locations and hence fault positions are clearly visible and more accessible to identify than with TDR [Furse et al. 2006; Tsai et al. 2005]. Besides, FDR can measure complex signals, amplitude and phase, at discrete frequency points and thereby measure RF quantities like return or insertion loss. Comparable results and RF quantities are obtainable with TDR after sampling and processing the measured RX signal. Depending on the employed TX signal, FDR methods can cover specific and various frequency bands of interest and thereby apply uniform power at those frequencies, resulting in excellent RF measurement capabilities [Shin et al. 2005]. In general, FDR systems offer a larger dynamic range resulting in greater sensitivity for detecting low reflective targets like soft-faults. In addition, soft-faults are easier to detect at higher frequencies which also works in favor of FDR. However, it is still very challenging and a subject of research to detect minor faults with FDR techniques. This is reported, for instance, in [Dubey et al. 2021; Furse et al. 2003, 2006; Furse et al. 2021; Griffiths et al. 2006; Naik et al. 2006; Vanhamme 1990; Ybarra et al. 1995]. Unlike TDR, FDR is better suited for detecting multiple faults beyond a first significant fault and measuring possible upcoming faults further down the TLUT. Also, an assessment of these faults is more feasible with FDR since it can differentiate between minor faults of different levels and not just detect and locate catastrophic faults like opens or shorts [Thomas 2006].

Furthermore, FDR operates with constant and low transmission power due to inherent pulse compression, which causes a high measurement sensitivity in combination with the favorable small intermediate frequency (IF) bandwidth. This small IF bandwidth works also in favor of noise suppression. FDR offers high range resolution capabilities as well, especially in short range with no blind spot handicap, and has a better noise immunity than TDR [Furse et al. 2006; Naik et al. 2006].

While TDR realizations need to be accurately synchronized, FDR is often implemented with the common homodyne principle [Piper 1995] and thereby inherently accurate and enables a signal processing at relatively low frequencies, which is favorable in terms of hardware needs [Jankiraman 2018]. The resolution and accuracy of FDR are determined by the bandwidth of the TX signal employed, which is the equivalent to the rise time of the pulses in TDR [Ybarra et al. 1995]. An increase in bandwidth in FDR corresponds to a decrease in rise time of the TDR pulses [Furse et al. 2006; Shin et al. 2005]. A benefit of FDR is that a single-shot measurement obtains a full set of results. Also, dynamic targets are traceable by a fast swept FDR resulting in an excellent temporal resolution and a fast update rate for changes.

The necessary FFT serves as a pulse compression for sinusoids, which on the one hand, results in distinct peak locations for each fault, but on the other hand, introduces side lobes close to those peak locations, which can impair the accuracy and cover closely neighboring faults. This drawback can be alleviated by using appropriate window functions.

The accuracy of all reflectometry methods depends on the exact knowledge of the velocity of propagation along the TLUT and its consistency. This quantity is needed to convert the respective time- or frequency-domain results to a precise range scale [Naik et al. 2006]. An accuracy of 10 cm is reported in [Tsai et al. 2005], while the authors of [Furse et al. 2003] demonstrate a 3 cm accuracy, both for FDR techniques.

1.2 Industrial Monitoring Usage: Airbag Deployment

The automotive industry utilizes the common FMCW radar principle for many sensing applications, such as autonomous driving, safety assistance, or guidance systems [Hasch 2015; Schneider 2005]. In order to improve car and road safety, radar sensors have been widely employed as active safety systems for pre-crash sensing and collision mitigation [Wenger 2005]. In the frame of this work, an additional FMCW radar usage in the field of car safety is suggested. An airbag deployment measurement and monitoring approach is presented through a transmission line based FMCW reflectometry setup.

Car companies and automotive supplier companies have employed the airbag, which belongs to the field of passive restraint systems, as a safety device in passenger cars since the late 1980s and early 1990s to support occupants with a supplementary cushioning and restraint effect in case of accidents. The widespread equipment of passenger vehicles with airbags has led to a significant decrease in fatalities or severe injuries in car accidents worldwide [Braver and Kyrychenko 2004; Chan 2007; Crandall et al. 2001; Mikhail and Huelke 1997; Pearlman et al. 2001; Wallis and Greaves 2002].

In the early stages, only the driver seat was equipped with a frontal airbag. However, nowadays, up to a two-digit number of airbag configurations are integrated into modern passenger vehicles to protect the occupants to a maximum. Those configurations comprise side airbags, curtain airbags, knee airbags, seatbelt airbags, and pedestrian airbags. All those airbags, which possess volumes of up to 100 liters, are fired with speeds of

over 300 km/h resulting in a complete unfolding within about 20 to 50 ms after ignition [Mikhail and Huelke 1997]. Significant forces are needed to facilitate this highly dynamic deployment process, resulting in a fast and high pressuring of the bag accompanied by a quick rise in temperature.

Although the airbag has a predominantly positive effect on the overall safety of passenger vehicles, its explosive unfolding can cause severe up to fatal injuries. The literature describes several possible injuries reaching from abrasions, burns, fractures, eye injuries, hearing loss, or even fatal head and neck fractures [Crandall et al. 2001; Farmer and Jain 2007; Mikhail and Huelke 1997; Pearlman et al. 2001; Wallis and Greaves 2002].

Such Airbag attributed injuries and deaths due to improper or unreliable functioning of airbags have led to various expensive lawsuits and negative headlines against car companies and automakers. Since car safety is a critical aspect in terms of marketability, the prevention of airbag-associated injuries is of interest for further investigations in this field. Furthermore, extensive research and development are still performed by industry and scientists in order to gain a thorough understanding and to aim for a reliable reproducibility of this highly dynamic process.

The effectiveness of an airbag severely depends on its exact timing and correct unfolding. Proper timing and triggering of the inflation together with an exact knowledge of the deployment duration are crucial for the correct functioning. A deployment too soon or too late can cause significant differences regarding the protection of vehicle occupants [Chan 2007; Wallis and Greaves 2002].

Since airbags exist in various configurations and are produced by several companies worldwide, various folding techniques and packing methods exist, which all cause different unfolding behavior in shape and speed. Among those techniques are, for instance, the roll-fold, the Leporello-fold, the scrunch-fold, the ring-fold, the star-fold, the stochastic/chaotic-fold, or even origami-based fold approaches [Bruton et al. 2016; Khan and Moatamedi 2008; Mao and Appel 2002; Ruff et al. 2007]. Detailed, thorough, and excessive testing is mandatory before an airbag is approved for integration in a passenger vehicle. The automotive industry imposes safety-related devices with strict requirements and default test procedures. In general, those test and validation procedures are very time and money consuming.

The initial folded and the fully unfolded state are well understood and simple to measure. However, uncertainty, unpredictability, and unforeseen behavior still occur right between those two states during the explosive unfolding. In this process, especially the early stages of the deployment are of interest since they are crucial for the shape and speed of the deployment [Khan and Moatamedi 2008; Ruff et al. 2007].

Therefore, several measurements, tests, and monitoring methods have been utilized and invented through the years to fully understand, optimize, and visually track this deployment behavior. These methods comprise numerical simulation models [Bendjaballah et al. 2017; Khan and Moatamedi 2008; Mroz and Pipkorn 2007; Muñoz et al. 2007; Ruff et al. 2007], high-speed video or stereo cameras [Bruton et al. 2016; Mao and Appel 2002; Muñoz et al. 2007], computer tomography scans (CT), or mechanical impactor tests [Mroz and Pipkorn 2007; Ruff et al. 2007]. However, all these methods have difficulties in

capturing the deployment process in its entirety. Numerical models struggle with the high complexity, the high speed of the deployment process together with the simultaneous implementation of mechanical and thermodynamic properties and their interaction.

Therefore, up to now, the results of simulation models sometimes differ severely from the results obtained by mechanical tests and optical methods [Bendjaballah et al. 2017; Mroz and Pipkorn 2007; Muñoz et al. 2007]. High-speed video camera images taken during the deployment are a valuable alternative to simulation models. However, these optical methods also suffer from the speed of the deployment and line of sight blockage, resulting in a lack of visibility and accessibility [Muñoz et al. 2007]. Especially the critical early stages of deployment right after the firing can not be monitored by optical methods due to the blockage of the housing and the hatch. Also, extracting detailed data from an image in which a big white bag is seen, offering very little contrast, is prone to errors and only provides limited accuracy [Bendjaballah et al. 2017; Mroz and Pipkorn 2007; Muñoz et al. 2007].

In view of these reasons, additional research and an improvement of airbags and their test techniques are crucial for advances in car safety and a further reduction of fatalities in car accidents worldwide.

1.3 Problem Statement

Considering the state-of-the-art reflectometry methods for testing faults on transmission lines, it is pretty challenging to detect and locate minor faults reliably. Since such soft-faults result in a small impedance variation which is often times rather continuous than instantaneous, a large dynamic range of the TX signal and a high sensitivity of the reflectometer are needed. Furthermore, an accuracy on the order of centimeters along a TLUT is not trivial to establish. This range accuracy directly corresponds to the bandwidth employed by the TX signal when using FDR methods. For a centimeter accuracy, a bandwidth of several GHz is needed.

Additionally, detecting and tracing several closely neighboring faults on transmission lines is also challenging with both FDR and TDR methods. In particular, detecting soft-faults is crucial for the given application because bends of a transmission line due to folds of the airbag result only in minor, local impedance variations.

Another challenge is detecting, monitoring, and locating not just static faults but also fast varying and moving faults along a TLUT. If the TLUT is moving or vibrating, it is more difficult to detect faults since movement and vibration adds additional noise to the system, which can be even worse than hardware or ambient noise [Griffiths et al. 2006].

Recalling that an airbag deployment typically does not last longer than 50 ms, a fast swept TX signal and an appropriate receiver are required to capture such fast ongoing procedures. FDR methods are more suited for such applications due to their fast sweeping capabilities of the TX signal and an RX signal at comparably low frequencies. A TX signal with a sweep time in the microseconds range is mandatory to have a high update rate for such rapid ongoing procedures. A signal generation, analogously or digitally,

which provides a large dynamic range, a large bandwidth, highly linear and yet very fast-swept chirp pulses with a starting frequency in the lower UHF-band simultaneously is challenging to realize.

An additional challenge is to find and design a transmission line structure fitting for the airbag surface. This transmission line structure needs mechanical flexibility and reversibility and yet offering high electromagnetic sensitivity to bends as well as a good transmission and matching performance. Since conventional transmission line structures are made of well-conducting material, such as metal, they only offer minimal flexibility. Furthermore, all reflectometry methods have difficulties in testing short cables. TDR methods suffer under the so-called blind spot. In this case, due to the shortness of the cable, the TX overlaps the RX signal and thereby impairs a reliable detection of nearby targets. Analogous to the blind spot in TDR systems, in FDR systems, the direct spillover of the TX signal into the RX path worsens the measurement capabilities in very short range in a similar way. Additional length is often added to the TLUT, but it is challenging to acquire accurate results with reflectometry for very short-range applications [Furse et al. 2006].

1.4 Contributions, Scope, and Objective of the Thesis

In this work, a fast chirp FMCW reflectometer has been drafted, designed, and fabricated to detect and monitor fast varying discontinuities on transmission lines. The motivation of this work is grounded on the goal of testing and establishing an additional radar-based measurement approach for airbag deployment processes.

The signal generation of this FMCW reflectometer is based on direct digital synthesis (DDS) together with a subsequent analog frequency quadruplication approach to enhance bandwidth and, by that means, the range accuracy. A digital signal generation was chosen to exploit certain advantages like fast and agile sweeping capabilities, linearity, superior phase noise performance, and immunity against temperature and aging drifts which all work in favor in terms of accuracy and the given application. Especially the fast sweeping capabilities of DDS technology facilitate so-called fast chirp FMCW reflectometry to transmission lines which work in favor of the given airbag application.

Accordingly, a portable and compact FMCW reflectometer instrument for in-field measurements was built. This reflectometer operates on highly linear, broadband, and fast swept chirp signals with a sweep time on the order of microseconds and a working frequency starting at the lower UHF band, offering a bandwidth of 5.2 GHz [IEEE 2020; Möhring et al. 2021]. Besides the final setup for signal generation, four additional techniques and solutions to enlarge the bandwidth of a DDS-generated signal are presented. However, these four approaches are not further pursued due to their reduced performance compared to the DDS-driven frequency multiplier chain.

The second part of this work is the study and investigation of transmission line types suited for the designed reflectometer and the intended application. In the given airbag

application, the transmission line is attached to the surface of an airbag, functioning as a bend sensor for mechanical folds and surface deformations.

Thereby, two transmission line types and manufacturing techniques are tested in terms of their applicability for this usage, especially for their response on mechanical bends. The tested and fabricated transmission lines comprise twisted-pair cables out of enameled wire around a dielectric core and a stencil-printed coplanar waveguide from conductive ink directly printed on the airbag substrate.

The broadband and fast swept FMCW reflectometer and the sensing transmission line structure are designed with the long-term goal and motivation of this work in mind, the measurement of the deployment behavior of airbags at test benches.

1.5 Outline of the Thesis

In *Chapter 2*, the fundamental concepts and theoretical background concerning this work are presented. First, the FMCW radar and reflectometry principles are introduced and distinguished from the pulse radar principle. Subsequently, an analytic description of the FMCW measurement method is provided, and the concept of fast chirp FMCW radar is proposed. Furthermore, fundamental electromagnetic concepts are reviewed, beginning with Maxwell's equations and the corresponding Helmholtz equations. The fundamentals of wave propagation on transmission lines are drawn out in a summary on transmission line theory and the telegrapher equation. *Chapter 2* is concluded with a review of two-port scattering parameters.

The design and its hardware realization of the suggested FMCW reflectometer are presented in *Chapter 3*. The required system specifications are explained, beginning with introducing the application and the measurement approach. Based on these requirements, a design of an FMCW reflectometer is proposed and its implementation is described. Focus is laid on a digital signal generation with a subsequent analog multiplication approach. Besides the final design, additional solutions to enlarge the bandwidth of a digital synthesized signal are presented. All RF and supplementary components needed for the reflectometer like DC supply, cooling, and housing are described. At the end of *Chapter 3*, the signal quality of the reflectometer is described in terms of linearity, bandwidth, output power, and fast sweeping capabilities. The results and ideas presented in *Chapter 3* have been partially published in [Möhring et al. 2019a], [Möhring et al. 2019b], [Möhring et al. 2019c], [Möhring et al. 2021], and [Möhring et al. 2022].

Chapter 4 deals with the investigations on a flexible and bend-sensitive transmission line structure for the surface of an airbag. Two transmission line types and their vital parameters and quantities are presented, with a focus on the applicability for the airbag surface and bend sensitivity. These flexible transmission line types comprise a coplanar waveguide out of conductive ink directly stencil-printed on the tissue of an airbag and a twisted pair structure out of enameled wire around a dielectric core.

Experimental measurement results obtained with the designed and manufactured reflectometer are presented in *Chapter 5*. To demonstrate the accuracy and sensitivity

properties of the device, at the beginning of *Chapter 5*, interconnected, static, standard commercial, RF coaxial transmission lines with a match termination are investigated. Furthermore, bent transmission lines are examined, and time-varying discontinuities along a line are tracked and monitored. The chapter is concluded by providing results from dynamic measurement setups. Firstly, a monostatic radar setup is created employing a corner reflector and an antenna to reveal the dynamic measurement and tracking capabilities. Secondly, appearing and dissolving faults as produced manually along a transmission line are tracked over time. The results and ideas presented in the *Chapter 5* have been partially published in [Möhring et al. 2022; Möhring et al. 2021]. Finally, in *Chapter 6*, the main results and insights are summarized and discussed. Besides, an outlook for possible future research is provided.

Theoretical Background

The fundamental concepts and theoretical background concerning this thesis are reviewed and explained in the following. The FMCW radar measurement principle is outlined, including an analytic description, vital formulas, the concept of fast chirp FMCW radar, together with a comparison to pulse radar. Afterwards, fundamental electromagnetic concepts, including Maxwell's equations, the Helmholtz equation, transmission line theory with a review on reflection at discontinuities, are presented. The chapter closes with a survey on two-port scattering parameters.

2.1 FMCW Radar Measurement Principle

The radar principle was invented and patented in the year 1904 by the German engineer Christian Hülsmeyer [Hülsmeyer 1904]. Radar is an acronym for radio detection and ranging. It is used to locate, detect, speed measure, or further characterize objects through electromagnetic waves [IEEE 2017]. Although there are no physical bounds concerning the frequency spectrum utilized for radar applications, typically, radar frequencies range from the lower MHz range of the HF-band up to 300 GHz in the mm-wave band [IEEE 2020; Skolnik 1990].

Commonly, radar systems are subdivided into pulsed and continuous-wave (CW) systems, depending on the transmitted waveform. Pulse radars directly measure the time difference to a target in the time-domain, while FMCW systems indirectly measure the target range through a frequency shift of the TX and the RX signal [Jankiraman 2018]. Historically, pulsed radar was the prevalent technique that sends out a series of pulsed waveforms and subsequently listens for possible echoes to return to the receiver. The distance between the receiver and the target can be acquired by knowing the signal propagation speed. On the other hand, CW radars transmit and receive all the time but are limited to speed measurements of targets due to a Doppler frequency shift of a received echo signal. Further enhancements of CW radars led to FMCW radars that are capable of measuring

both, the distance and the speed of a target [Jankiraman 2018; Skolnik 2001; Stove 1992]. The FMCW radar principle has gained wide popularity over the last decades. It is utilized in various applications since it allows simultaneous detection of range and velocity information of multiple targets in a simple manner [Kronauge and Rohling 2014]. Nowadays, FMCW radars are widely utilized in research, industry, or military applications. For instance, the FMCW radar principle is made use of in the automotive industry for autonomous driving, radio altimeters, remote sensing and imaging via synthetic-aperture radar (SAR), level gauging, air surveillance purposes, or navigational tasks [Jung et al. 2021; Komarov and Smolskiy 2003; Pozar 2012; Stove 2004].

FMCW radar follows the same principle as FMCW reflectometry, which injects guided waves into transmission lines instead of operating with signals propagating in free space. Like other reflectometry methods, faults, discontinuities, bends, or other imperfections result in a local impedance mismatch or variation along the transmission line, which can be detected, localized, and quantified by the FMCW principle. Those discontinuities can be considered the targets.

The widespread usage of FMCW radar rests upon certain advantages over the traditional pulsed radar. The FMCW principle profits from a large time-bandwidth product, possible single-shot operation with a fast update rate, and high range resolution capabilities particularly in short range with no blind spot obstacle, when employing a sufficient amount of signal bandwidth. Due to the constant and commonly small transmit power, FMCW radar is rather suited for short- and mid-range operation. The constant transmit power due to inherent pulse compression causes a favorable high measurement sensitivity in combination with the advantageous small IF bandwidth. Further advantages of FMCW over pulse radar include the lower production cost, oftentimes smaller size, and a system architecture that tends to be more simple. The FMCW radar architecture is among the simplest forms of radar realizations [Komarov and Smolskiy 2003; Skolnik 1990, 2001; Stove 1992; Stove 2004].

At the same time, the inherent leakage from TX to RX due to limited isolation capabilities impairs the sensitivity and dynamic range of FMCW systems [Balon et al. 2018; Park et al. 2019; Pulutan and Marciano 2013]. This leakage leads to ghost targets in the first few range cells and degrades the dynamic range by increasing and dominating the noise floor [Park et al. 2021]. FMCW radars often employ bistatic configurations due to the limited TX-RX isolation. However, when using a single antenna or a single transmission line in monostatic setups, this limitation needs to be taken into account. Furthermore, FMCW radars reveal limitations regarding the maximum TX peak power compared to pulse radars, which can transmit high peak and average power. This leads to a limited maximum range, so FMCW radars are often used in short- and mid-range applications [Pulutan and Marciano 2013].

Various modulation schemes are employed in the field of FMCW radar. However, the most common is the usage of linearly frequency-modulated (LFM) signals in form of the sawtooth/ramp or triangular modulation, which is called chirp signal. Besides these typical LFM waveforms, other implementations exist, for instance, the stepped-frequency continuous-wave (SFCW) or the frequency-shift keying (FSK)-FMCW modulation [Hasch

2015; Kronauge and Rohling 2014; Liu and Liu 2014]. In the scope of this thesis, the LFM waveform is used in sawtooth and triangular modulation.

A generic monostatic FMCW radar setup in block diagram representation can be seen in Fig. 2.1. In this homodyne setup, the FM signal functions as the TX signal s_{TX} and also as the LO signal with which a possibly occurring RX signal s_{RX} due to a target is down-converted to the IF stage, also known as the baseband signal [Brooker 2005]. A splitter/divider or a directional coupler divides this TX signal into two paths. It directs this signal to both an antenna or transmission line and to the LO port of the receiving mixer, respectively. In such monostatic setups, a circulator is used as a duplexer so that the TX and RX paths can share the same antenna or transmission line. By mixing (heterodyning) the TX signal with the RX signal, the so-called beat signal s_{IF} is created, which contains the range and velocity information of the target in baseband. A final receiver records such IF data, and further processing is commonly performed in the digital domain employing an analog-to-digital converter (ADC) and DSP techniques [Komarov and Smolskiy 2003]. Most radars can be described in a simple manner by the so-called radar equation. This equation models the received power due to scattering from a possible target. Besides, it declares a relationship for the sensitivity of a radar by relating the transmitted power P_{TX} radiated by a transmitting antenna with gain G_{TX} to the received power P_{RX} due to scattering and re-radiation by a target with radar-cross section (RCS) σ and received by a receiving antenna with gain G_{RX} according to [Knott et al. 2004; Pozar 2012]

$$P_{\text{RX}} = \frac{P_{\text{TX}} G_{\text{TX}} G_{\text{RX}} \lambda^2 \sigma}{(4\pi)^3 r^4}. \quad (2.1)$$

In the case of a monostatic setup, as depicted in Fig. 2.1, the gain of the TX antenna matches the gain of the RX antenna, $G_{\text{TX}} = G_{\text{RX}}$. Likewise, for bistatic setups, where the gain of the receiving antenna G_{RX} can differ from G_{TX} . The variable r represents the separation between a target and the antenna, and the variable λ states the free-space wavelength [Pozar 2012].

The electromagnetic scattering behavior of any target can be characterized by its RCS. The RCS is defined under far-field conditions and as the ratio of the scattered power density S_{sca} from an object to the incident power density S_{inc} according to

$$\sigma = \lim_{r \rightarrow \infty} 4\pi r^2 \frac{S_{\text{sca}}}{S_{\text{inc}}} = \lim_{r \rightarrow \infty} 4\pi r^2 \frac{|E_{\text{sca}}|^2}{|E_{\text{inc}}|^2}. \quad (2.2)$$

The far-field condition is established in (2.2) by letting r approach infinity. Alternatively, the RCS can also be computed by taking the ratio of the squared magnitudes of the scattered electric field E_{sca} to the incident electric field E_{inc} .

The RCS can be considered as the scattering strength or effective scattering area of any given target and is a measure of how well an object scatters incident waves [Knott et al. 2004]. In this sense, the RCS depends mainly on the electrical size, the mechanical shape, and the material of an object and also on the polarization of the wave together with its incident and reflected angles. In radar applications, so-called corner reflectors are employed as reference targets, navigational aids for target localization, or for calibration

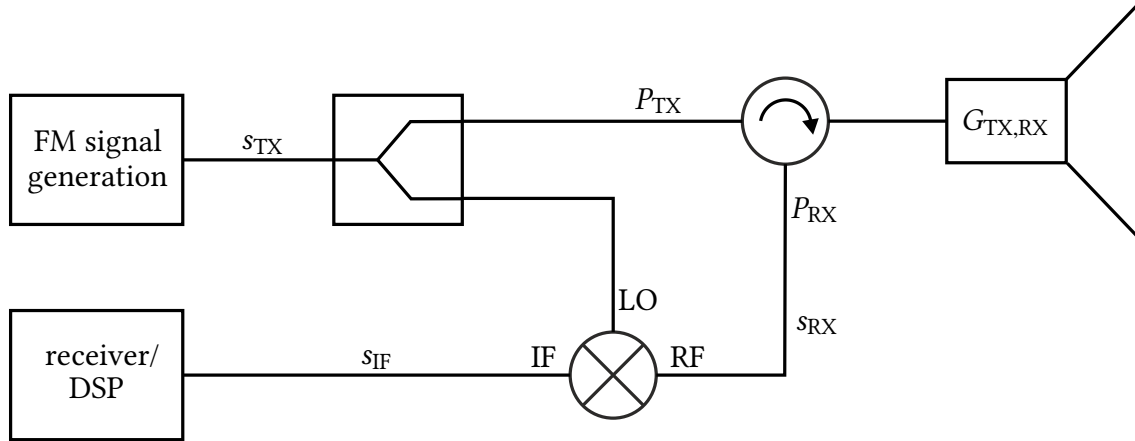


Fig. 2.1: Block diagram representation of a generic monostatic FMCW radar setup. The TX chirp signal s_{TX} is coupled through a splitter or directional coupler, passing a circulator into the antenna and to the LO port of the receiving mixer, respectively. Each target producing an echo results in an RF signal s_{RX} , which is received by the antenna and mixed (homodyne) with the TX signal. A final receiver records the down-converted baseband signal s_{IF} and converts it into the digital domain for further processing. Instead of an antenna, a TLUT can be employed to create an FMCW reflectometry setup [Komarov and Smolskiy 2003].

procedures. These reflectors scatter and direct incoming waves directly back to the source, thereby constituting a large radar echo and, hence, a large RCS. In this context, the maximum specific RCS of a trihedral corner reflector σ_{TCR} is calculated by

$$\sigma_{TCR} = \frac{4\pi l^4}{3\lambda^2}. \quad (2.3)$$

Such a reflector consists of three mutually perpendicular triangular surfaces with a respective edge length denoted by l . Corner reflectors are passive point targets in the far field and are often fabricated out of well-conducting material such as metal. Besides trihedral corner reflectors, simple plates, dihedral corner reflectors, or spheroids are also employed as reference targets [Knott et al. 2004; Pozar 2012].

2.1.1 Analytic Description of the FMCW Principle

An LFM chirp signal commonly functioning as the TX signal $s_{\text{TX}}(t)$ in FMCW radar or reflectometry setups can be written in time-domain according to [Kronauge and Rohling 2014; Möhring et al. 2021; Schroeder and Rohling 2010; Skolnik 1990; Stove 1992] as

$$s_{\text{TX}}(t) = a_{\text{TX}} \cos(\varphi(t)). \quad (2.4)$$

Thereby, the amplitude of this chirp signal is denoted by a_{TX} , and the initial phase φ_0 is set to zero. In this form, the variable $\varphi(t)$ contains the instantaneous phase term with its initial phase φ_0 at the time $t = 0$. Also, this phase term composes the initial start frequency f_{sta} at the time $t = 0$ and the chirp rate μ in the form of the instantaneous TX frequency of a generic sawtooth-modulated signal as

$$\varphi(t) = \varphi_0 + 2\pi \int_0^t f(t') dt' = \varphi_0 + 2\pi \int_0^t (f_{\text{sta}} + \mu t') dt' = \varphi_0 + 2\pi t \left(f_{\text{sta}} + \frac{\mu t}{2} \right), \quad (2.5)$$

which leads to the typical linear chirp formulation expression

$$s_{\text{TX}}(t) = a_{\text{TX}} \cos\left(2\pi t \left(f_{\text{sta}} + \frac{\mu t}{2} \right)\right). \quad (2.6)$$

The slope or chirp rate μ is an important parameter and relates the transmit signal bandwidth B_{TX} as set by the lower frequency bound f_{sta} and upper frequency bound f_{stp} to the sweep time T_s of a single chirp,

$$\mu = \frac{B_{\text{TX}}}{T_s} = \frac{f_{\text{stp}} - f_{\text{sta}}}{T_s}. \quad (2.7)$$

A schematic illustration of a generic LFM chirp signal with sawtooth modulation is shown in Fig. 2.2 in a time-domain representation. There, the effect of the linearly increasing instantaneous frequency over time can be seen. In a second plot in Fig. 2.3, in a frequency-time representation, the sawtooth modulation scheme is shown together with its vital parameters bandwidth B_{TX} and sweep time T_s . The bandwidth of the TX signal B_{TX} is an essential parameter since it determines the range resolution or range cell size Δr of a radar instrument. This range resolution is a measure for distinguishing between adjacent targets, and it is inversely proportional to the bandwidth B_{TX} of the TX signal [Kronauge and Rohling 2014]. It is calculated via the speed of propagation c of the signal, in free space or on the transmission line as

$$\Delta r = \frac{c}{2B_{\text{TX}}}. \quad (2.8)$$

Technically, this range resolution is also dependent on the linearity of the chirp. Hence, would the chirp signal not be strictly linear, as seen in Fig. 2.3, the range resolution capabilities would be degraded [Brooker 2005].

At possible targets, a portion of the TX signal is reflected back to the receiver. In this

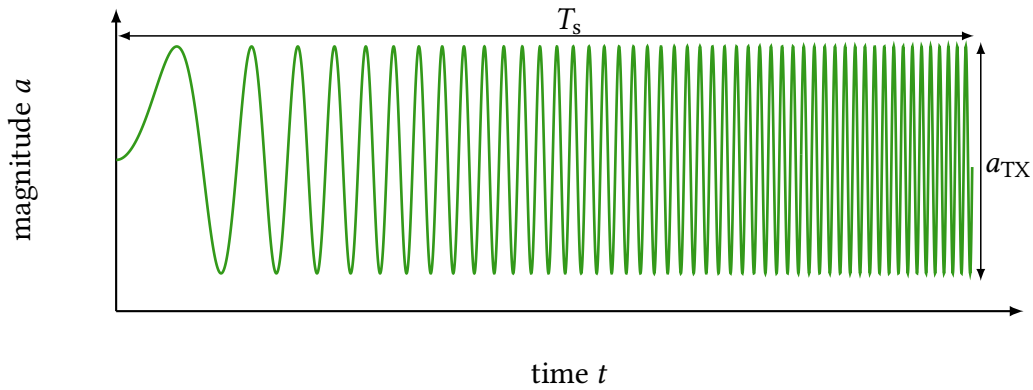


Fig. 2.2: Linearly frequency-modulated sawtooth chirp signal in the time-domain [Jankiraman 2018].

manner the RX signal $s_{RX}(t)$ can be considered and written as the sum of time-delayed and attenuated replicas of the TX signal $s_{TX}(t)$ [Balon et al. 2018; Winkler 2007],

$$s_{RX}(t) = \sum_{i=1}^M \Gamma_i s_{TX}(t - \tau_{d,i}), \quad (2.9)$$

where M is the number of targets and Γ_i are the reflection coefficients of the respective targets. The variable τ_d represents the round-trip time to a target and back.

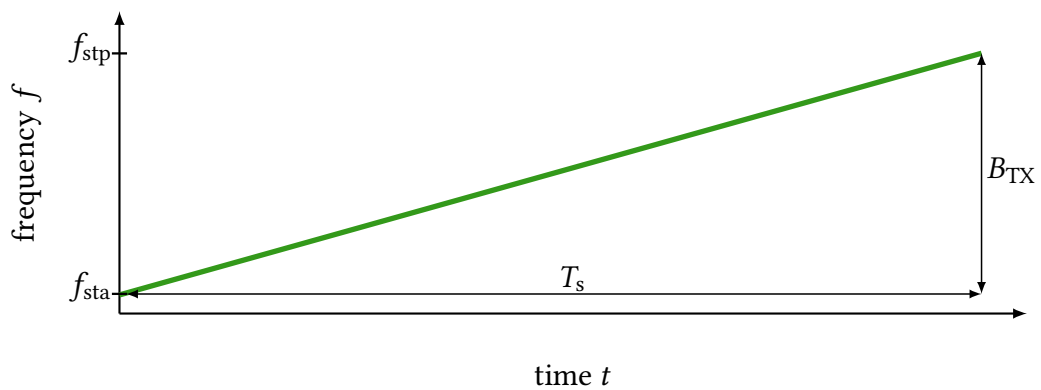


Fig. 2.3: Linearly frequency-modulated (ramp/sawtooth) chirp signal in frequency-time representation [Jankiraman 2018].

The reflection coefficient Γ_i determines the amount of power, which is reflected by a target, and thereby the amplitude of the RX signal to $a_{RX} = \Gamma a_{TX}$, under the theoretical assumption that the signals underlie no further attenuation effects. In this context, it is pointed out that multiple interactions of discontinuities along the transmission line are not included here as are attenuation effects, to not overwhelm (2.9).

Since this work deals with FMCW reflectometry, the targets to be detected are discontinuities (index d) along a TL. As such, the local reflection coefficient of such a discontinuity corresponds to a local impedance variation, with respect to the characteristic impedance of the employed transmission line Z_0 . Such a reflection coefficient from transmission line theory [Pozar 2012] can be expressed as Z_0 in relation to the impedance of the discontinuity Z_d ,

$$\Gamma_i = \frac{Z_{d,i} - Z_0}{Z_{d,i} + Z_0}, \quad (2.10)$$

where $Z_{d,i}$ is the impedance of the discontinuity. In the case of free-space FMCW radar, the radar equation of (2.1) can be employed to determine the received power of possible targets with corresponding reflection characteristics as determined by their RCS σ . Both quantities need to be incorporated into (2.9) for the FMCW radar case.

In Fig. 2.4, a plot is shown with a generic triangular-modulated TX signal in green together with two possible RX signals due to targets; one static target $s_{RX,s}$ and one dynamically moving target $s_{RX,d}$. Those targets are received with a time delay being represented by the round-trip time τ_d which is directly proportional to the frequency difference Δf which in turn is called beat frequency f_b .

Additionally, moving targets also produce a Doppler shift f_D which is the carrier of the velocity information [Pulutan and Marciano 2013]. This round-trip time to a target or discontinuity of range r_d is denoted by the variable τ_d and when considering moving targets or discontinuities also with the radial velocity v_r due to a Doppler shift by

$$\tau_d = \frac{2r_d}{c} + \frac{2v_r t}{c}. \quad (2.11)$$

As seen in Fig. 2.4, the range r_d is directly proportional to the round-trip time and is indicated by a horizontal shift along the time axis. The direction of movement with a corresponding velocity of a target produces a shift along the vertical axis. A target approaching the receiver produces a positive Doppler frequency ($f_D > 0$) as indicated in Fig. 2.4. On the other hand, a target moving away from the receiver leads to a negative Doppler frequency ($f_D < 0$). This principle works with all LFM modulation schemes. However, the Doppler information can be better separated from the range information by employing triangular instead of sawtooth modulation. The latter term in (2.11) can be neglected when considering static targets only.

Recapitulating the block diagram in Fig. 2.1, the IF signal is created by mixing and thereby down-converting the TX signal with the RX signal. The resulting IF baseband signal in time-domain $s_{IF}(t)$ can be written in a simplified form according to [Winkler 2007] by employing standard trigonometric identities, assuming no conversion loss within the mixing process and no signal propagation losses, neglecting the range-Doppler coupling,

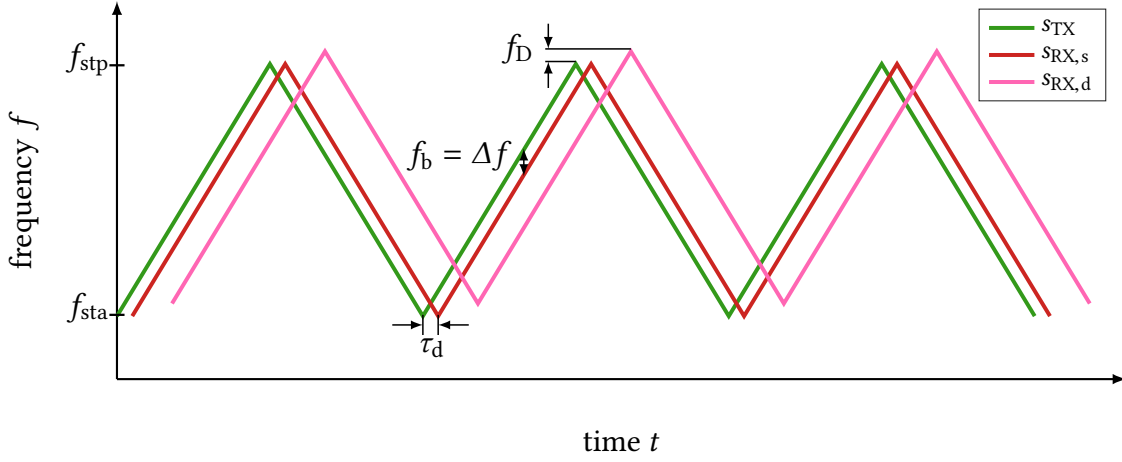


Fig. 2.4: Linearly triangular frequency-modulated TX chirp signal s_{TX} with corresponding echoes of generic static $s_{\text{RX},s}$ and generic moving target $s_{\text{RX},d}$ in frequency-time representation. The beat frequency f_b contains the range information of the target, while the velocity information is found in the Doppler frequency f_D [Jankiraman 2018].

neglecting multiple reflections, neglecting noise components, and considering $\tau_d/T_s \ll 1$ [Stove 1992; Winkler 2007],

$$s_{\text{IF}}(t) = \sum_{i=1}^M \frac{\Gamma_i a_{\text{TX}}}{2} \cos\left(2\pi\left(\frac{2f_{\text{sta}}r_{d,i}}{c} + \left(\frac{2f_{\text{sta}}v_{r,i}}{c} + \frac{2\mu r_{d,i}}{c}\right)t\right)\right). \quad (2.12)$$

Range and Doppler information are obviously embedded into the phase information of this IF signal. Extracting the phase information yields the beat frequency f_b , which can be separated into a range component f_r and into a Doppler component f_D , according to

$$f_{b,i} = f_{r,i} + f_{D,i} = \frac{2\mu r_{d,i}}{c} + \frac{2f_{\text{sta}}v_{r,i}}{c}. \quad (2.13)$$

Especially for the short ranges, the round trip time τ_d is small compared to the sweep time of a chirp T_s [Anghel et al. 2014]. The range and Doppler profile are computed by employing a two-dimensional FFT of the IF beat signal to display the corresponding range and Doppler profiles [Schroeder and Rohling 2010]. As seen in (2.13), the beat frequency f_b is influenced by both the target range but also by the velocity of the target. However, separating the range and velocity information of multiple targets unambiguously and simultaneously is not trivial. Various approaches are reported in the literature. For instance, employing multiple chirps of different slopes or special waveforms are utilized to resolve this issue [Kronauge and Rohling 2014; Lutz et al. 2014; Rohling and Meinecke

2001; Roos et al. 2019; Thurn et al. 2016; Winkler 2007]. The maximum range r_{\max} of an FMCW radar is set, besides signal power boundaries, by the maximum possible beat frequency $f_{b_{\max}}$. Any receiver containing an ADC for conversion into the digital domain must provide a sampling frequency f_{SMP} that satisfies the Nyquist theorem according to

$$f_{\text{SMP}} > 2f_{b_{\max}} = \frac{4B_{\text{TX}}}{c T_s} r_{\max}. \quad (2.14)$$

Thereby, the bandwidth of the IF signal is much smaller than the bandwidth of the TX signal since, in homodyne and coherent FMCW radars, the RX signal is down-converted with the TX signal [Kronauge and Rohling 2014].

The velocity resolution or Doppler resolution Δv is similar to the range resolution Δr in (2.8). This quantity states that two moving targets can be distinguished by their different radial velocities v_r if these are separated larger than [Kronauge and Rohling 2014; Roos et al. 2019]

$$\Delta v = \frac{c}{2fT_sL} = \frac{\Delta f_D \lambda}{2}. \quad (2.15)$$

Thereby, in the frame of this work, the total measurement time $t_{\text{mt}} = LT_s$ is defined by the number of transmitted chirps L with the chirp duration T_s .

2.1.2 Fast Chirp FMCW Radar Concept

The need to separate the velocity information from the range information reliably and simultaneously, especially in multitarget situations as typical in the automotive context, has led to new waveform designs and implementations [Kronauge and Rohling 2014; Rohling and Meinecke 2001; Roos et al. 2019; Thurn et al. 2016]. Since in the field of FMCW radar, the beat frequency comprises both range and velocity information of a target simultaneously, in accordance with (2.13), special waveforms are required to distinguish between these two quantities reliably. This has been achieved, for instance, by employing chirps with different ramp slopes or by using multiple frequency shift keying (MFSK) [Kronauge and Rohling 2014; Lutz et al. 2014; Rohling and Meinecke 2001]. However, with these approaches, only a limited number of targets can be differentiated, or in the case of MFSK, the estimation accuracy is very low [Kronauge and Rohling 2014; Roos et al. 2019].

Nowadays, in contrast to the conventional slow-ramp modulation waveforms, so-called fast chirp modulation waveforms emerged over the years. These fast chirp FMCW waveforms date back to the year 1992 and were suggested, for instance, in [Kronauge and Rohling 2014; Lutz et al. 2014; Möhring et al. 2021; Schroeder and Rohling 2010; Stove 1992; Tong et al. 2015; Winkler 2007]. They make use of a sequence of L successive very fast swept sawtooth-modulated chirps of equal slope with a sweep time in the range of 100 μs down to 1 μs . The traditional, slow-ramp FMCW modulation employs chirps with respective sweep times in the millisecond to second range [Tong et al. 2015].

These very short sweep times T_s in the μs -range facilitate a reliable separation of range and velocity information because now the range information is found in a far higher frequency range than the Doppler information when looking at (2.13). The beat frequency f_b is now dominated by the range and not so much by the radial velocity v_r of a target [Kronauge and Rohling 2014]. Therefore, for simple range measurements, this Doppler contribution can be neglected [Kronauge and Rohling 2014; Lutz et al. 2014; Schroeder and Rohling 2010; Thurn et al. 2016].

At the same time, the frequency shift of the beat frequency to the MHz range demands faster sampling ADCs when looking at (2.14). This leads to higher sampling efforts and an increase of the IF bandwidth which in turn extends the hardware costs and complexity, as well as signal processing power [Hasch 2015; Roos et al. 2019]. Additionally, the increased IF signal bandwidth facilitates the deployment of single-channel receivers (I-channel), reducing hardware and calibration complexity according to [Kronauge and Rohling 2014; Schroeder and Rohling 2010]. Furthermore, fast swept and highly linear ramps are difficult to generate or synthesize, especially with analog sources like phase-locked loops (PLL) [Hasch 2015; Roos et al. 2019; Thurn et al. 2016].

Another application of the fast chirp modulation waveform lies in the monitoring and tracking of quickly moving targets or fast ongoing procedures. The very fast sweep times allow measurements with a rapid update rate on the order of, e.g., 100.000 transmitted chirps per second. By this means, possible targets are recorded much quicker [Tong et al. 2015]. This quicker capturing of targets leads to a lower duty cycle and enhances the signal-to-noise ratio (SNR) of the whole radar device.

Furthermore, the common DC offset problem in FMCW systems is alleviated by fast chirp modulation since the beat frequency is shifted to higher frequency bands and thereby further away from the DC bin. Also, fast chirps facilitate higher selectivity of neighboring targets due to less overlap and a better separation of targets [Möhring et al. 2021; Tong et al. 2015].

2.2 Electromagnetic Field Theory and TEM Waves

Since this work deals with wave propagation on transmission lines, Maxwell's equations which are the foundation for all classical electromagnetic phenomena and electromagnetic wave propagation, are briefly recapped [Orfanidis 2016]. Transmission line theory and the so-called telegrapher's equations are derived on that groundwork, which provide the basics for wave propagation on transmission lines. Also, the equivalent circuit for TLs with all its vital parameters is presented together with the reflection and transmission behavior at discontinuities. In the end, two-port scattering parameters are introduced.

2.2.1 Maxwell's Equations and Constitutive Relations

Maxwell's equations in differential form can be written and distinguished into four different equations. In this manner, the Ampère-Maxwell law

$$\nabla \times \mathbf{H} = j\omega\mathbf{D} + \mathbf{J} \quad (2.16)$$

relates the displacement current density $j\omega\mathbf{D}$ and the electric current density \mathbf{J} to the magnetic field \mathbf{H} . Thereby, $\nabla \times$ represents the curl operator. The Faraday equation connects the electric field \mathbf{E} to the time-derivative of the magnetic flux density \mathbf{B} according to

$$\nabla \times \mathbf{E} = -j\omega\mathbf{B}. \quad (2.17)$$

The last two equations incorporate the divergence operator $\nabla \cdot$ and are named Gauss' law for electric and magnetic fields

$$\nabla \cdot \mathbf{D} = \rho, \quad (2.18)$$

$$\nabla \cdot \mathbf{B} = 0. \quad (2.19)$$

Therein, the electric displacement or flux density \mathbf{D} is related to the electric charge density ρ . All the above-stated vector quantities are assumed to be location dependent, i.e., $\mathbf{H} = \mathbf{H}(\mathbf{r})$. The observation point is represented by \mathbf{r} . All fields are considered time-harmonic with a time dependence according to $e^{j\omega t}$, ω being the angular frequency and t is the time. However, this time dependence is suppressed throughout this work [Detlefsen and Siart 2012; Jin 2015; Orfanidis 2016; Pozar 2012; Zinke and Brunswig 1965].

Additional equations are declared, so-called constitutive relations [Jin 2015; Orfanidis 2016; Pozar 2012; Zinke and Brunswig 1965], to consider two other phenomena, namely the electric polarization and the magnetization, as well as the electric conductivity κ of materials. These constitutive relations describe the electromagnetic response of materials and connect the flux densities with the fields taking the given material properties into account according to

$$\mathbf{D} = \varepsilon_0\mathbf{E} + \mathbf{P} = \varepsilon_0(1 + \chi_e)\mathbf{E} = \varepsilon\mathbf{E} = \varepsilon_0\varepsilon_r\mathbf{E}, \quad (2.20)$$

$$\mathbf{B} = \mu_0(\mathbf{H} + \mathbf{M}) = \mu_0(1 + \chi_m)\mathbf{H} = \mu\mathbf{H} = \mu_0\mu_r\mathbf{H}. \quad (2.21)$$

Therein, the considered material is specified by its permittivity ε and its permeability μ . The permittivity ε is a measure of polarizability, which is incorporated in (2.20) by the polarization density \mathbf{P} and electric susceptibility χ_e . The variable ε_0 denotes the vacuum permittivity, while the relative permittivity, also referred to as the dielectric constant [Pozar 2012] of a medium, is characterized by ε_r .

Analogous to the effect of electric polarization for dielectric materials, the magnetization effect applies to magnetic materials. This magnetization is expressed by the magnetization intensity or also magnetization vector \mathbf{M} and the magnetic susceptibility χ_m , as stated in (2.21). Thereby, the vacuum permeability is expressed by μ_0 , and the variable μ_r denotes

the relative permeability [Detlefsen and Siart 2012; Jin 2015; Orfanidis 2016; Zinke and Brunswig 1965].

The third relevant and material-dependent equation in this context is Ohm's law. It relates the electric field E to the current density J , taking the given material's conductivity κ into account and considering the impressed current density J_i [Orfanidis 2016],

$$J = \kappa E + J_i . \quad (2.22)$$

Together with the electric conductivity κ , the permittivity ε and the permeability μ of a material are known as constitutive parameters. In free-space, the permittivity reduces to the vacuum permittivity $\varepsilon = \varepsilon_0 \approx 8.854 \cdot 10^{-12}$ As/Vm and the permeability reduces to the vacuum permeability $\mu = \mu_0 = 4\pi \cdot 10^{-7}$ Vs/Am. With the aid of these two vacuum quantities, two fundamental physical constants are derived [Orfanidis 2016]. The speed of light in vacuum c_0 is stated by

$$c_0 = \frac{1}{\sqrt{\mu_0 \varepsilon_0}} = 299\,792\,458 \text{ m/s} \quad (2.23)$$

and the impedance of free space or also known as the characteristic impedance of vacuum η_0 or Z_0 , is calculated by

$$\eta_0 = Z_0 = \frac{|E|}{|H|} = \sqrt{\frac{\mu_0}{\varepsilon_0}} = 120\pi \Omega \approx 376.730 \Omega . \quad (2.24)$$

In the case of not considering vacuum, the material properties of the material, as expressed by its relative permittivity ε_r and relative permeability μ_r , need to be taken into account when calculating the propagation speed of the wave c in this given medium according to

$$c = \frac{1}{\sqrt{\mu \varepsilon}} = \frac{1}{\sqrt{\mu_0 \mu_r \varepsilon_0 \varepsilon_r}} , \quad (2.25)$$

and analogously when determining the characteristic impedance η of this material to

$$\eta = Z = \frac{|E|}{|H|} = \sqrt{\frac{\mu_0 \mu_r}{\varepsilon_0 \varepsilon_r}} . \quad (2.26)$$

Both material parameters, relative permittivity ε_r and relative permeability μ_r , can be complex quantities in case of considering losses. Then, the relative permittivity ε_r of a medium can be written as

$$\varepsilon_r = \varepsilon_r' - j\varepsilon_r'' , \quad (2.27)$$

where the imaginary part ε_r'' accounts for the energy losses. With the aid of this complex relative permittivity, the electric loss tangent is calculated to

$$\tan \delta_e = \frac{\varepsilon_r''}{\varepsilon_r'} . \quad (2.28)$$

Furthermore, when dealing with time-harmonic fields, the losses due to the conductivity of a material can also be incorporated into the dielectric losses as expressed by the

complex permittivity [Jin 2015; Orfanidis 2016; Pozar 2012]. The combination of these two loss mechanisms is apparent when employing the complex permittivity of (2.27) and the conductivity relationship of (2.22), neglecting the impressed current density and substituting both into (2.16), which yields to

$$\nabla \times \mathbf{H} = j\omega\epsilon\mathbf{E} + \kappa\mathbf{E} = j\omega\epsilon_0\epsilon'_r\mathbf{E} + (\omega\epsilon_0\epsilon''_r + \kappa)\mathbf{E}. \quad (2.29)$$

This gives rise to an extension of the electric loss tangent formulation of (2.28), now taking both the dielectric and conductivity losses into account [Jin 2015], resulting in

$$\tan \delta_e = \frac{\epsilon''_r}{\epsilon'_r} + \frac{\kappa}{\omega\epsilon'_r\epsilon_0}. \quad (2.30)$$

Analogously, the complex relative permeability μ_r is formulated according to [Jin 2015]

$$\mu_r = \mu'_r - j\mu''_r, \quad (2.31)$$

which leads to the formula for the magnetic loss tangent

$$\tan \delta_m = \frac{\mu''_r}{\mu'_r}. \quad (2.32)$$

Commonly, linear, homogeneous, stationary, non-dispersive, and isotropic media are considered leading to a scalar and simple formulation of the respective constitutive parameters permittivity ϵ , permeability μ , and conductivity κ [Jin 2015]. In this context, linear states that the field intensities and the flux intensities are linearly dependent. A homogeneous medium suggests that the parameters ϵ , μ , and κ are independent of the location or position within the medium. Besides, non-dispersive and stationary implies that ϵ , μ , and κ are independent of frequency and time, respectively. Finally, isotropic means that the directions of the respective fluxes and fields coincide. Hence \mathbf{D} is parallel to \mathbf{E} , as well as \mathbf{B} is parallel to \mathbf{H} . In anisotropic media, the respective constitutive parameters need to be expressed by dyadics which are second-order tensors [Jin 2015; Orfanidis 2016; Pozar 2012].

2.2.2 Skin Effect and Boundary Conditions

The two constitutive parameters permeability μ and electrical conductivity κ cause another electromagnetic effect when considering conductive material at high frequencies, the so-called skin effect.

Eddy currents induce this effect due to induction mechanisms following the Faraday equation of (2.17). As a result, the currents predominantly flow close to the surface of a conductor and decay exponentially with e^{-z/δ_s} , when entering the conductor further. Thereby, the variable z represents the radial axis of the conductor. By this means, the skin

depth δ_s states the penetration depth of the current in conducting material depending on the frequency f and is calculated via [Pozar 2012; Wheeler 1942]

$$\delta_s = \sqrt{\frac{2}{\omega\mu\kappa}} = \frac{1}{\sqrt{\pi f\mu\kappa}}. \quad (2.33)$$

That implies that the current densities are concentrated at very high frequencies at a thin region near the outer surface of well-conducting material. The inner of the conductor can be considered free of fields and currents. This results in an increase in electrical resistance due to the reduction of the effective cross-section. The related quantity of surface resistance is also provoked by the skin effect [Detlefsen and Siart 2012; Orfanidis 2016; Pozar 2012; Wheeler 1942].

Boundary conditions at media interfaces are essential criteria in solving Maxwell's equations. At such an interface involving two different media, medium 1 and medium 2, respectively, the electric and magnetic fields \mathbf{E} and \mathbf{H} and the corresponding flux densities \mathbf{D} and \mathbf{B} obey the boundary conditions [Detlefsen and Siart 2012; Jin 2015; Orfanidis 2016]

$$\hat{\mathbf{n}} \times (\mathbf{E}_2 - \mathbf{E}_1) = 0, \quad (2.34)$$

$$\hat{\mathbf{n}} \times (\mathbf{H}_2 - \mathbf{H}_1) = \mathbf{J}_s, \quad (2.35)$$

$$\hat{\mathbf{n}} \cdot (\mathbf{D}_2 - \mathbf{D}_1) = \rho_s, \quad (2.36)$$

$$\hat{\mathbf{n}} \cdot (\mathbf{B}_2 - \mathbf{B}_1) = 0. \quad (2.37)$$

In this context, the vector $\hat{\mathbf{n}}$ represents the normal unit vector at the media interface pointing from medium 1 to medium 2. The surface current density at the interface is denoted by \mathbf{J}_s , and the variable ρ_s states the surface charge density. From (2.34) and (2.37), it is evident that the tangential components of the electric field \mathbf{E} are continuous across the media interface, and likewise the normal components of the magnetic flux density \mathbf{B} . On the other hand, a present electric surface charge density ρ_s induces a corresponding jump of the normal component of the electric flux density \mathbf{D} according to (2.36). Analogously, the tangential components of the magnetic field \mathbf{H} also jump due to the electric surface current density \mathbf{J}_s when examining (2.35).

In case of no electric surface current density \mathbf{J}_s and no electric surface charge density ρ_s at the media interface, the so-called source-free boundary condition applies. Then, the normal components of the flux densities are continuous, and so are the tangential components of the respective fields [Detlefsen and Siart 2012; Jin 2015; Orfanidis 2016; Pozar 2012; Zinke and Brunswig 1965].

2.2.3 Helmholtz Equation and Plane Wave Solution

Maxwell's equations of (2.16) to (2.19) can be solved by some basic mathematical expressions embracing specific prerequisites [Zinke and Brunswig 1965]. By utilizing the constitutive relations of (2.20) and (2.21), the Ampère-Maxwell law of (2.16) and the Faraday's law of (2.17) can be rewritten to

$$\nabla \times \mathbf{H} = j\omega\epsilon\mathbf{E}, \quad (2.38)$$

$$\nabla \times \mathbf{E} = -j\omega\mu\mathbf{H}. \quad (2.39)$$

These two equations hold for a source-free ($\mathbf{J} = 0$, $\rho = 0$), isotropic, homogeneous, linear, and time-invariant region [Pozar 2012]. Applying the curl operator ($\nabla \times$) to (2.39) and substituting (2.38) into (2.39) leads to an equation for the electric field \mathbf{E} only

$$\nabla \times (\nabla \times \mathbf{E}) = -j\omega\mu (\nabla \times \mathbf{H}) = \omega^2\epsilon\mu\mathbf{E}. \quad (2.40)$$

Utilizing the vector calculus identity $\nabla \times (\nabla \times \mathbf{X}) = \nabla(\nabla \cdot \mathbf{X}) - \nabla^2\mathbf{X}$ [Bronstein et al. 2001], and highlighting the source-free assumption ($\nabla \cdot \mathbf{E} = 0$) leads to the Helmholtz equation for the electric field \mathbf{E} and magnetic field \mathbf{H} , respectively [Orfanidis 2016; Pozar 2012; Zinke and Brunswig 1965],

$$\nabla^2\mathbf{E} + \omega^2\epsilon\mu\mathbf{E} = 0, \quad (2.41)$$

$$\nabla^2\mathbf{H} + \omega^2\epsilon\mu\mathbf{H} = 0. \quad (2.42)$$

These two equations can also be formulated with the Laplace operator Δ since it holds $\nabla^2\mathbf{X} = \Delta\mathbf{X}$ [Bronstein et al. 2001]. Furthermore, these two equations contain the wavenumber k , which is calculated via the angular frequency ω and the permittivity $\epsilon = \epsilon_0\epsilon_r$ and the permeability $\mu = \mu_0\mu_r$ of the considered material according to

$$k = \omega\sqrt{\epsilon\mu} = \omega\sqrt{\epsilon_0\epsilon_r\mu_0\mu_r} = \frac{2\pi}{\lambda}. \quad (2.43)$$

In this context, the variable λ represents the wavelength. Also, the wavenumber is related to the complex propagation constant γ , which comprises an attenuation constant α and a phase constant β [Jin 2015],

$$\gamma = jk = \alpha + j\beta. \quad (2.44)$$

One possible and straightforward solution to (2.41) is obtained by utilizing the method of separation of variables and yielding the fields of plane waves which can be written as

$$\mathbf{E}(\mathbf{r}) = \mathbf{E}_{\text{fw}}e^{-jk \cdot \mathbf{r}} + \mathbf{E}_{\text{bw}}e^{+jk \cdot \mathbf{r}}. \quad (2.45)$$

Therein, the vector \mathbf{r} is a location vector for a generic observations point. In a standard three-dimensional environment $\mathbf{r} \in \mathbb{R}^3$ holds, and \mathbf{r} can be expressed in Cartesian coordinates to $\mathbf{r} = x\hat{\mathbf{e}}_x + y\hat{\mathbf{e}}_y + z\hat{\mathbf{e}}_z$. The wave number \mathbf{k} is written in Cartesian coordinates

as $\mathbf{k} = k_x \hat{\mathbf{e}}_x + k_y \hat{\mathbf{e}}_y + k_z \hat{\mathbf{e}}_z$. From there, the dispersion relation can be obtained, which relates the wave number to the frequency in the form of

$$\mathbf{k} \cdot \mathbf{k} = k_x^2 + k_y^2 + k_z^2 = k^2. \quad (2.46)$$

The plane wave solution of (2.45) is a superposition of two waves, one propagating forward in $+\mathbf{k}$ and one propagation backward in $-\mathbf{k}$ direction. Thereby, the two vectors \mathbf{E}_{fw} and \mathbf{E}_{bw} are the field amplitude vectors of each wave which also contain the polarization of the wave. These two field vectors must be perpendicular to the direction of propagation \mathbf{k} [Jin 2015; Pozar 2012].

The phase velocity v_p is a material-dependent quantity and states the propagation speed of planes of constant phase. In the case of vacuum, the phase velocity is equal to the speed of light c_0 , besides it is calculated with the angular frequency ω and the phase constant β to [Pozar 2012]

$$v_p = \frac{\omega}{\beta} = \frac{c_0}{\sqrt{\epsilon_r \mu_r}}. \quad (2.47)$$

The velocity of the overall envelope of a wave is specified by the group velocity according to [Jin 2015]

$$v_g = \left(\frac{\partial \beta}{\partial \omega} \right)^{-1}. \quad (2.48)$$

In case of no dispersion, the phase velocity v_p and the group velocity v_g are identical [Detlefsen and Siart 2012; Jin 2015; Orfanidis 2016; Pozar 2012].

2.3 Transmission Line Theory

Next, the transmission line theory is introduced, which addresses the propagation and distribution of electromagnetic waves on transmission lines. Thereby, transmission lines are cables or similar structures with commonly two conductors, in which one-dimensional transverse electromagnetic (TEM) wave propagation takes place in a contained manner. In addition to classical two-conductor transmission lines, further waveguide realizations exist, such as hollow waveguides or optical fibers. However, the latter two types do not support TEM waves but instead, among others, also transverse electric (TE) or transverse magnetic (TM) waves. In this sense, transmission line theory connects the classic field theory with the basic circuit theory by taking wave propagation phenomena into account. In transmission line theory, voltages and currents are considered along the transmission line whose wavelength is on the order of the dimension of the considered transmission line [Detlefsen and Siart 2012; Jin 2015; Marcuvitz 1951; Pozar 2012; Unger and Hinken 1991; Zinke and Brunswig 1965].

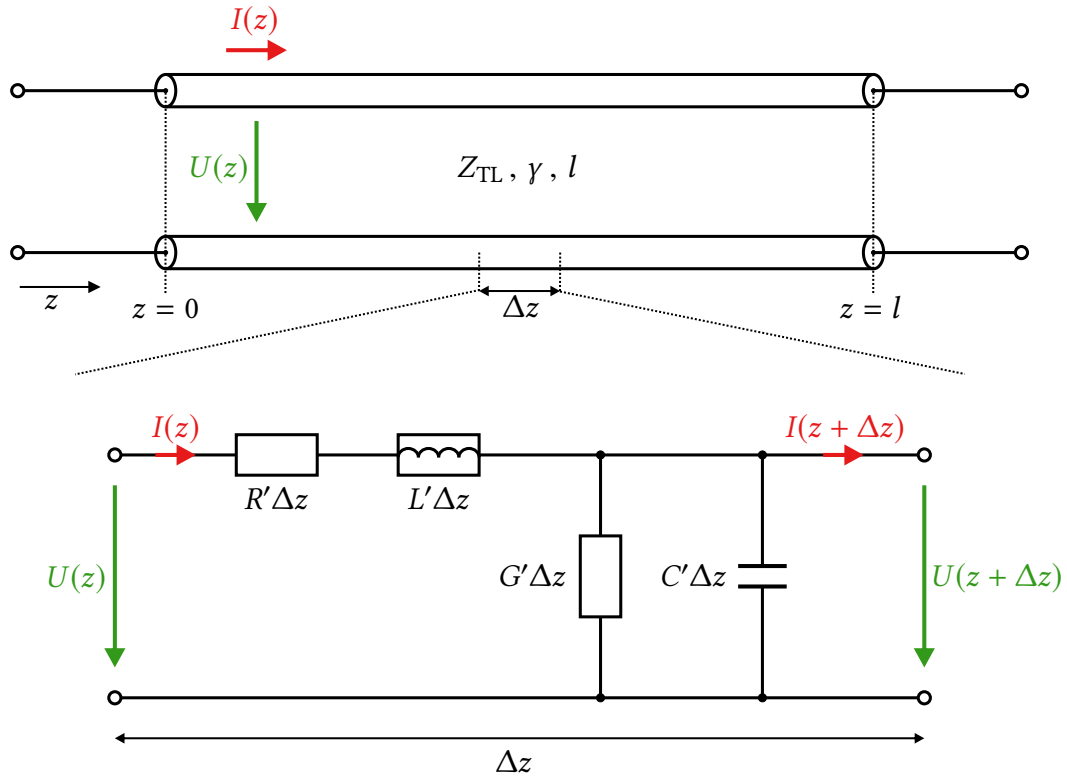


Fig. 2.5: Block diagram of generic transmission line of length l along the z -axis with voltage $U(z)$ and current $I(z)$ definitions on top. Below, the equivalent circuit model with lumped elements representing an infinitesimal small piece of length Δz of transmission line [Detlefsen and Siart 2012; Pozar 2012].

2.3.1 Derivation of Telegrapher's Equations

An infinitesimally small piece of a generic transmission line can be modeled by a lumped element circuit, as shown in Fig. 2.5. When examining the top of Fig. 2.5, a generic transmission line of length l is shown together with its characterizing parameters, the propagation constant γ , and its characteristic impedance Z_{TL} , comparable to the free-space quantities of (2.44) and (2.26), respectively. The bottom of Fig. 2.5 depicts an equivalent circuit representation with lumped elements, representing an infinitesimally short transmission line of length Δz .

The shown transmission line extends along the z -axis along which the voltages $U(z)$ and currents $I(z)$ travel [Jin 2015; Papazyan et al. 2004; Pozar 2012]. In that respect, the variables R' and L' stand for the series resistance and series inductance per unit length,

respectively. In contrast, the variables G' and C' denote the shunt conductance and capacitance per unit length. In an ideal lossless case, the series resistance R' and shunt conductance G' are zero since these two quantities account for the losses. Thereby, the variable R' represents the ohmic losses of the conductors due to their finite conductivity, and G' denotes the polarization losses of the dielectric between the two conductors. The capacitive effect of two conductors arranged in close proximity to form a transmission line is represented by the shunt capacitance C' . In comparison, the series inductance L' stands for the self-inductance of the two conductors. These four quantities, R' , L' , G' , and C' , are also referred to as primary line constants [Detlefsen and Siart 2012; Pozar 2012; Unger and Hinken 1991].

In this case, only a small fraction of length Δz is considered; a real transmission line can be assumed a cascaded version of the equivalent circuit of Fig. 2.5. Recalling this equivalent circuit and employing Kirchhoff's circuit laws for voltages and currents leads to the so-called Telegrapher's equations in time-domain which relate the voltages $U(z)$ and currents $I(z)$ along the transmission line to the parameters of the equivalent circuit to [Detlefsen and Siart 2012; Jin 2015; Pozar 2012]

$$\frac{\partial U(z)}{\partial z} = -(R' + j\omega L')I(z), \quad (2.49)$$

$$\frac{\partial I(z)}{\partial z} = -(G' + j\omega C')U(z). \quad (2.50)$$

These two linear partial differential equations reveal a high similarity to the two Maxwell's equations of (2.38) and (2.39) from which the Helmholtz equation is derived [Jin 2015; Pozar 2012]. Furthermore, these two linear partial differential equations can be combined into a set of second-order differential equations with each containing only one dependent variable, either voltage U or current I [Jin 2015; Marcuvitz 1951; Pozar 2012].

These resulting equations are nothing else than one-dimensional Helmholtz equations of transmission lines and compose of

$$\frac{\partial^2 U(z)}{\partial z^2} - \gamma^2 U(z) = 0, \quad (2.51)$$

$$\frac{\partial^2 I(z)}{\partial z^2} - \gamma^2 I(z) = 0. \quad (2.52)$$

The variable γ denotes the complex propagation constant of a transmission line, analogously to (2.44), also comprising the constant α and phase constant β . It can be written as [Pozar 2012]

$$\gamma = \alpha + j\beta = \sqrt{(j\omega L' + R')(j\omega C' + G')}. \quad (2.53)$$

Besides the propagation constant γ , the characteristic impedance Z_{TL} is also dependent on the transmission line's lumped-element quantities. It is the ratio of voltage and current of a single wave along the transmission line. It is calculated to [Pozar 2012; Zinke and Brunswig 1965]

$$Z_{\text{TL}} = \frac{R' + j\omega L'}{\gamma} = \sqrt{\frac{j\omega L' + R'}{j\omega C' + G'}} = \frac{U(z)}{I(z)}. \quad (2.54)$$

Together with the propagation constant γ , the characteristic impedance Z_{TL} forms the group of secondary line constants. Its geometry and the employed material usually determine this characteristic impedance of a transmission line and in case of a homogeneous line it is independent of its length [Detlefsen and Siart 2012].

At high frequencies or in the lossless case, the characteristic impedance is dominated rather by the inductance L' and the capacitance C' per unit length, while the resistance R' and the conductance G' are negligible ($\omega L' \gg R'$, $\omega C' \gg G'$). Then, the characteristic impedance can be approximated by a real number according to

$$Z_{\text{TL}} \approx \sqrt{\frac{L'}{C'}}. \quad (2.55)$$

Analogously to the solution of the two homogeneous Helmholtz equations of (2.41) and (2.42), solving the two transmission line Helmholtz equations of (2.51) and (2.52) also leads to a superposition of two voltage and two current waves. Again, the first term states a wave propagating in $+z$ -direction, while the second term stands for a wave traveling in $-z$ -direction following Fig. 2.5, both for voltages and currents [Detlefsen and Siart 2012; Orfanidis 2016; Pozar 2012],

$$U(z) = U_1 e^{-\gamma z} + U_2 e^{+\gamma z}, \quad (2.56)$$

$$I(z) = \frac{U_1}{Z_{\text{TL}}} e^{-\gamma z} - \frac{U_2}{Z_{\text{TL}}} e^{+\gamma z}. \quad (2.57)$$

The two constants U_1 and U_2 are arbitrary constants of integration and are to be determined by employing two boundary conditions [Unger and Hinken 1991].

The velocity factor (VF) is used to take into account the impact of the dielectric material of a transmission line on the speed of propagation of the wave. The VF is defined as the ratio of the velocity of propagation on the transmission line v_p to the speed of light in vacuum c_0 as

$$\text{VF} = \frac{v_p}{c_0} = \frac{1}{\sqrt{\mu_r \epsilon_r}}, \quad (2.58)$$

where commonly non-ferromagnetic materials are considered, such as dielectrics with $\mu_r = 1$. A VF relates the mechanical length to the electrical length of a transmission line. This quantity is essential for reflectometry methods due to the need for the exact travel time of a wave along a transmission line [Orfanidis 2016]. Typically, the speed of the wave on the transmission line v_p is approximately 0.6 to 0.8 times the speed of light in vacuum c_0 , depending on the employed dielectric (e.g., Teflon) [Furse et al. 2003].

In order to achieve a transmission line completely free of distortion, the Heaviside condition must be fulfilled according to [Lundstedt 1995; Pozar 2012]

$$\frac{G'}{C'} = \frac{R'}{L'}. \quad (2.59)$$

2.3.2 Reflection and Transmission at Discontinuities

In order to study the behavior of wave propagation along transmission lines with a discontinuity, two infinitely long and interconnected transmission lines are considered, as depicted in Fig. 2.6. This setup is comparable to a plane wave impinging normally on a planar interface between two homogeneous half-spaces filled with different media in free-space [Jin 2015].

In this case, the joint location is set to $z = d$, both lines extend along the z -axis, and both lines reveal different characteristic impedances $Z_{TL,1}$ and $Z_{TL,2}$, respectively, with $Z_{TL,1} \neq Z_{TL,2}$. Now considering a voltage wave $U_{inc}(z)$ propagating along positive z -direction from the left side $z < d$, in accordance with (2.56) and (2.57) and impinging on the joint location.

The joint location represents a local impedance discontinuity at which a part of the wave is reflected $U_{ref}(z)$, and the remaining $U_{tra}(z)$ is transmitted traveling further down the line. Such a local change in characteristic impedance along a transmission line is called discontinuity or inhomogeneity. In the case of a homogeneous transmission line, the characteristic impedance is considered consistent and independent of the location along the line. Besides an interconnection of transmission lines, such a local discontinuity or inhomogeneity can represent a local impurity, fault, bent, defect, or kink of cable [Detlefsen and Siart 2012; Jin 2015; Pozar 2012].

In transmission line theory, the reflection coefficient Γ_d is defined as the ratio of the complex amplitudes of the incident and reflected wave according to [Detlefsen and Siart 2012]

$$\Gamma_d = \frac{U_{ref}(z = d + \Delta z)}{U_{inc}(z = d)} = \frac{Z_{TL,2} - Z_{TL,1}}{Z_{TL,2} + Z_{TL,1}}. \quad (2.60)$$

It results from enforcing the boundary condition at the discontinuity $z = d$, which requires the voltages and currents on either side to be equal. On the other hand, the transmission coefficient T_d , which is related to the reflection coefficient, measures how much of the incident wave is transmitted beyond the discontinuity.

This transmission coefficient relates the incident wave to the transmitted wave, which travels further in positive z -direction [Detlefsen and Siart 2012; Jin 2015; Pozar 2012] in accordance to

$$T_d = 1 - \Gamma_d = \frac{U_{tra}(z = d + \Delta z)}{U_{inc}(z = d)} = \frac{2Z_{TL,2}}{Z_{TL,2} + Z_{TL,1}}. \quad (2.61)$$

Thereby, the reflected wave superimposes the incident wave and travels back in the negative z -direction. This superposition of incident and reflected waves leads to a standing wave. It is commonly expressed with the voltage standing wave ratio (*VSWR*) by taking the maximum wave magnitude $|U_{max}|$ and minimum wave magnitude $|U_{min}|$ into a ratio as [Pozar 2012]

$$VSWR = \frac{|U_{max}|}{|U_{min}|} = \frac{1 + |\Gamma_d|}{1 - |\Gamma_d|}. \quad (2.62)$$

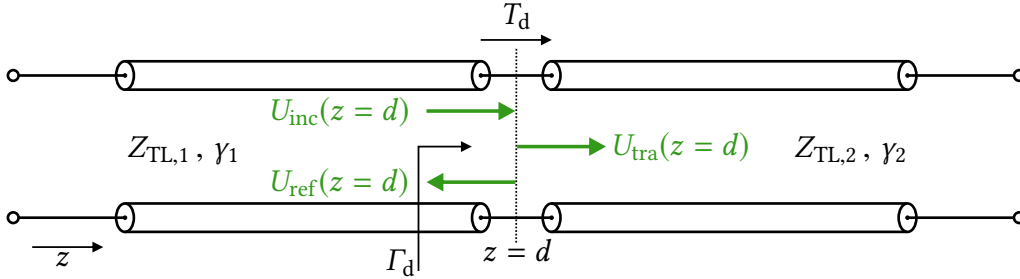


Fig. 2.6: Block diagram of two interconnected transmission lines with different characteristic impedances, $Z_{TL,1}$ and $Z_{TL,2}$, respectively, representing a local discontinuity at position $z = d$. At this location, an incident voltage wave U_{inc} is divided, resulting in a partially reflected U_{ref} and partially transmitted wave U_{tra} , depending on the corresponding reflection Γ_d and transmission coefficient T_d [Orfanidis 2016].

Two interconnected transmission lines are referred to as perfectly matched if their respective characteristic impedances match, hence $Z_{TL,1} = Z_{TL,2}$. The same result is obtained by removing the latter line of Fig. 2.6 and instead terminating the first line by a load impedance Z_L . Now, if this load impedance matches the characteristic impedance $Z_L = Z_{TL,1}$, no wave will be reflected at the location of interconnection $z = d$ of Fig. 2.6. This would result in an ideal $VSWR$ of 1 due to a reflection coefficient of $\Gamma_d = 0$.

Usually, when interconnecting transmission lines, a small $VSWR$ is desirable due to a corresponding small reflected wave. However, a total reflection from the location of the discontinuity $z = d$ is achieved by either short-circuiting the load, $Z_L = 0$, resulting in a reflection coefficient of $\Gamma_d = -1$, or by leaving the load open-circuited, $Z_L = \infty$, producing a reflection coefficient of $\Gamma_d = +1$ [Detlefsen and Siart 2012; Jin 2015; Pozar 2012].

Besides the $VSWR$, the quantity of mismatch can also be expressed by the return loss (RL), which is also dependent on the reflection coefficient Γ_d and is calculated as

$$RL \text{ (dB)} = 10 \log_{10} \frac{P_{inc}}{P_{ref}} = -20 \log_{10} |\Gamma_d|. \quad (2.63)$$

The RL is commonly defined in decibels (dB), and so is the according quantity for the transmission coefficient T_d , the insertion loss (IL)

$$IL \text{ (dB)} = 10 \log_{10} \frac{P_{\text{tra}}}{P_{\text{inc}}} = -20 \log_{10} |T_d|. \quad (2.64)$$

In the last two loss quantities RL and IL , related power quantities are employed instead of taking the incident, reflected, and transmitted voltage waves. Thereby, the incident power P_{inc} , the reflected power P_{ref} , and the transmitted power P_{tra} are connected to the voltage quantities by the characteristic impedances [Detlefsen and Siart 2012; Jin 2015; Orfanidis 2016; Pozar 2012; Unger and Hinken 1991].

2.4 Two-Port Scattering Parameters

The behavior of linear electrical networks is commonly described by employing equivalent circuit parameters such as impedance matrices, admittance matrices, or transfer matrices. At low frequencies, the present port voltages and currents are used to describe such networks.

However, commonly power waves are employed at high frequencies in the RF domain because directly measuring voltages and currents at the respective ports is quite challenging since it involves magnitude and phase measurements of location-dependent traveling and standing waves [Detlefsen and Siart 2012; Orfanidis 2016; Pozar 2012].

For this reason, in microwave engineering, when the wave nature of the signal must be taken into account, like in transmission line theory, so-called scattering parameters (S -parameters) are used to describe the behavior of linear networks. The S -parameter description is an approach to combine circuit theory analysis with transmission line and field theory concepts.

These S -parameters describe networks completely and can express vital quantities such as RL , IL , isolation, coupling, directivity, or gain behavior of individual components. Standard RF devices such as transmission lines, directional couplers, filters, mixers, amplifiers, or similar are often characterized by S -parameters [Hiebel 2016; Orfanidis 2016; Pozar 2012].

In Fig. 2.7, a generic two-port network in block diagram representation is seen, including the corresponding scattering parameters together with port voltages U_i , currents I_i , and wave quantities a_i, b_i . Each port offers incident and reflected power waves a and b together with a reference impedance Z_0 which is usually 50Ω [Papazyan et al. 2004; Pozar 2012].

The normalized incident power wave is denoted by a , while the normalized reflected power wave is represented by b . Both are calculated over the respective port voltages, currents, and reference impedance of the line according to [Orfanidis 2016]

$$a_1 = \frac{U_1 + I_1 Z_0}{2\sqrt{Z_0}}, \quad a_2 = \frac{U_2 + I_2 Z_0}{2\sqrt{Z_0}}, \quad (2.65)$$

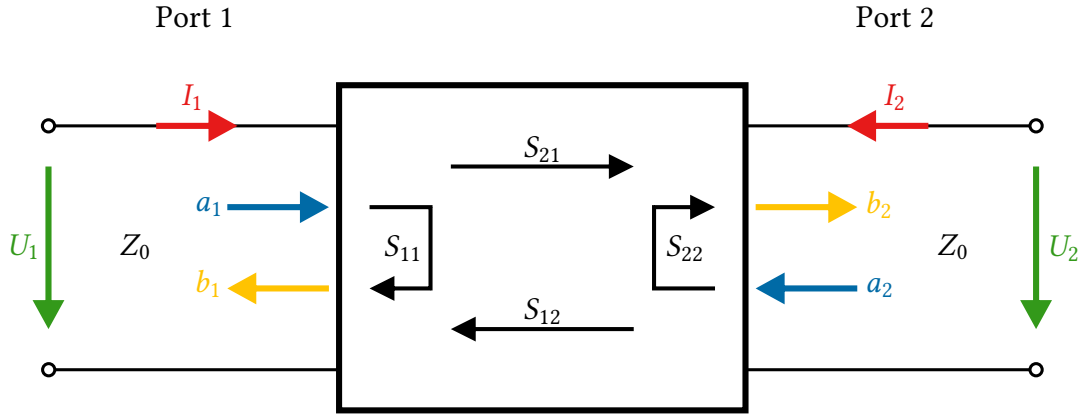


Fig. 2.7: S-parameter definition of generic two-port in block diagram representation [Papazyan et al. 2004; Pozar 2012].

$$b_1 = \frac{U_1 - I_1 Z_0}{2\sqrt{Z_0}}, \quad b_2 = \frac{U_2 - I_2 Z_0}{2\sqrt{Z_0}}. \quad (2.66)$$

Port 1 is considered the input in this two-port network, and port 2 as the output. The input and output reflection coefficients at port 1 and port 2, respectively, are defined by S_{11} and S_{22} according to

$$S_{11} = \left. \frac{b_1}{a_1} \right|_{a_2=0}, \quad S_{22} = \left. \frac{b_2}{a_2} \right|_{a_1=0}, \quad (2.67)$$

under the condition that the incident wave at the respective other port is zero, $a_2 = 0$ and $a_1 = 0$, which is established by matching these ports [Marcuvitz 1951; Pozar 2012]. On the other hand, the forward transmission coefficient from port 1 to port 2 is denoted by S_{21} , and the reverse transmission coefficient from port 2 to port 1 is stated by S_{12} , according to

$$S_{21} = \left. \frac{b_2}{a_1} \right|_{a_2=0}, \quad S_{12} = \left. \frac{b_1}{a_2} \right|_{a_1=0}. \quad (2.68)$$

Analogously, this \mathbf{S} -matrix definition can be extended to any N -port with a corresponding \mathbf{S} -matrix of dimension $N \times N$. For the given two-port, the complete \mathbf{S} -matrix in matrix-vector notation is written as

$$\begin{pmatrix} b_1 \\ b_2 \end{pmatrix} = \mathbf{S} \begin{pmatrix} a_1 \\ a_2 \end{pmatrix} = \begin{pmatrix} S_{11} & S_{12} \\ S_{21} & S_{22} \end{pmatrix} \begin{pmatrix} a_1 \\ a_2 \end{pmatrix}. \quad (2.69)$$

In common microwave network analysis, VNAs are employed to measure the complex S -parameters of any given active or passive N -port. Transmission lines like a coaxial cable are passive and linear two-ports [Papazyan et al. 2004]. For instance, a perfectly matched transmission line of length l and propagation constant γ reveals the \mathbf{S} -matrix [Detlefsen and Siart 2012]

$$\mathbf{S}_{\text{TL}} = \begin{pmatrix} 0 & e^{-j\gamma l} \\ e^{-j\gamma l} & 0 \end{pmatrix}. \quad (2.70)$$

The perfect matching at both ends is denoted by $S_{11} = S_{22} = 0$ while the transmission behavior of S_{21} and S_{12} is represented by the wave propagation term $e^{-j\gamma l}$. Employing the S -parameters of such a two-port transmission line, the quantities IL and RL as defined in (2.63) and (2.64) can be rewritten to [Pozar 2012]

$$RL \text{ (dB)} = -20 \log_{10} |S_{11}|, \quad IL \text{ (dB)} = -20 \log_{10} |S_{21}|. \quad (2.71)$$

Furthermore, a general microwave two-port as seen in Fig. 2.7 can also be described by its impedance matrix (\mathbf{Z} -matrix), which relates the port voltages to the port currents according to [Pozar 2012] and the corresponding admittance matrix \mathbf{Y} , which is just the inverse of the \mathbf{Z} -matrix, $\mathbf{Y} = \mathbf{Z}^{-1}$,

$$\begin{pmatrix} U_1 \\ U_2 \end{pmatrix} = \mathbf{Z} \begin{pmatrix} I_1 \\ I_2 \end{pmatrix} = \begin{pmatrix} Z_{11} & Z_{12} \\ Z_{21} & Z_{22} \end{pmatrix} \begin{pmatrix} I_1 \\ I_2 \end{pmatrix}. \quad (2.72)$$

In addition, the \mathbf{S} -matrix can be converted into other related parameter representations like, for instance, into the \mathbf{ABCD} -matrix, the \mathbf{Z} -matrix, or the \mathbf{Y} -matrix [Pozar 2012]. Further information about S -parameters can be found, for example, in [Detlefsen and Siart 2012; Hiebel 2016; Marcuvitz 1951; Orfanidis 2016; Pozar 2012].

FMCW Reflectometer Instrumentation

The concept and the implementation of a portable FMCW reflectometer measurement device are presented next. Design ideas, system requirements due to the proposed application, and the suggested measurement approach are stated and explained in Section 3.1. In Section 3.2, the signal generation approach is presented based on a DDS-driven frequency multiplier chain together with additional techniques of enlarging the bandwidth of a DDS generated chirp signal. Section 3.3 deals with the hardware realization of the multiplier chain and the whole FMCW reflectometer, and presents all employed RF components, the power supply unit, the housing, and cooling devices for the reflectometer. The chapter closes with Section 3.4, presenting the system specifications, measurement capabilities, and the quality of the TX signal of the proposed FMCW reflectometer. Ideas, content, and preliminary results of this chapter have been published in [Möhring et al. 2019a], [Möhring et al. 2019b], [Möhring et al. 2019c], [Möhring et al. 2021], and [Möhring et al. 2022].

3.1 Application, Approach, and System Requirements

As previously stated, the FMCW radar principle has been widely used for various ranging and detection tasks. In the scope of this work, the FMCW radar principle is employed for guided waves propagating on RF transmission lines (TL) or cables instead of using unguided signals in free space. This technique is known as FMCW reflectometry, which belongs to the field of FDR, which in turn is strongly related to the more popular TDR [Furse et al. 2003].

This research is motivated by developing an additional measurement method for airbag deployment processes in order to overcome the still present uncertainties regarding its deployment. Furthermore, the method shall provide information and insights about the deployment, which other current methods can not. In the long term, the results of this measurement technique shall be used to learn more about the deployment process in

general, investigate various existing folding techniques, provide additional input for simulation tools, and thereby help to improve the overall car safety further [Möhring et al. 2022].

The initial idea for employing the FMCW radar principle to TLs and thereby measure airbag deployment processes, along with previous research in this field, has been developed by the Technical University of Munich (TUM), Munich, Germany, in cooperation with the German car company AUDI AG. The outcome of this research has been published in [Bao 2015; Bao et al. 2011, 2013, 2014]. The current work has been performed and partially funded in cooperation with the development department of airbag systems, I/EK-542, of the AUDI AG in Ingolstadt, Germany.

3.1.1 Measurement Approach

Before an airbag is deployed, regardless of whether at a test bench or in a car in case of an accident, it is folded, packed, and compressed multiple times to fit into the limited housing volume of its module. For the proposed measurement approach to work and before the folding and packing procedure takes place, an RF TL is directly attached to the surface of an airbag. This TL functions as a bend sensor for the multiple folds that occur and dissolve during the folding and rapid unfolding process, respectively. Since in case the airbag surface is folded or unfolded, the TL obeys this mechanical deformation.

At the specific fold or bend location, minor local impedance variations occur due to the mechanical deformation, which deviate from the employed TL's characteristic impedance and result in a local reflection coefficient. Due to this impedance mismatch at these locations, a signal traveling down the TL is partially reflected and partially transmitted. In other words, the bend locations of the TL produce minor local discontinuities, impurities, or faults at which signals are partially reflected. The magnitude of this reflection directly corresponds to the extent of a fold of an airbag, which in turn is directly related to the local reflection coefficient of the TL. The larger the reflection coefficient, the larger or stronger the fold.

Employing the ranging capabilities of an FMCW reflectometer, these bends along the line can be localized and, by this means, also the fold locations of the airbag. These fold locations and their rapid development during deployment can be considered the targets to be detected and monitored with the FMCW reflectometer. It needs to be stated that depending on the TL structure employed, even severe bends of a TL only result in minor impedance variations, hence weakly reflective targets. Such minor impedance variations along the TL are also known as soft-faults.

A sketch of the proposed monostatic, single-ended reflectometry measurement setup is depicted in Fig. 3.1. There, an exemplary airbag is shown with an attached sensing TL on its surface.

The TL's exact pathway is adjustable and depends on the airbag type, the employed folding method, and the strategy of what regions of the surface area to investigate. A feed line connects the sensing TL with the FMCW reflectometer measurement device. At test benches, the distance between the reflectometer and the to-be-fired airbag can count

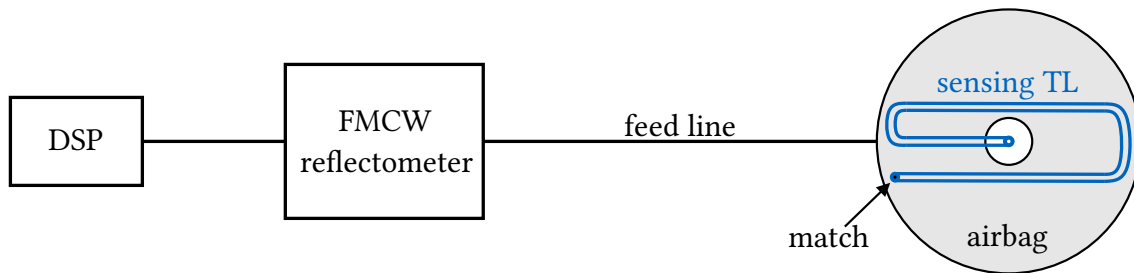


Fig. 3.1: Schematic block diagram of proposed TL-based FMCW measurement approach to monitor airbag deployment scenarios at test benches. A sensing TL, attached to the surface of an airbag, functions as the bend sensor. A feed line connects the TL to the reflectometer. Bends along the sensing TL can be tracked and traced with the FMCW reflectometer, thereby indicating a deploying airbag's current bend status, suggesting its deployment behavior. The measurement data is recorded and further processed with DSP techniques.

for several meters. The obtained measurement results are first converted into the digital domain employing an ADC or a digital storage oscilloscope (DSO) and then processed with DSP techniques. A match terminates the sensing TL. Consequently and ideally, if the TL is not bent at all, no signal will be reflected, and the match will ideally absorb all energy.

The reflectometer operates in one direction only, and the overall received signal is the sum of all partially reflected signals by each discontinuity. Given the suggested application, several system requirements concerning the reflectometer are needed. Those system requirements are discussed in the next subsection.

3.1.2 System Requirements

Before dealing with the actual design of the FMCW reflectometer, first, the system requirements are outlined based on the proposed application.

The airbag deployment process typically lasts no longer than 20 ms to 50 ms. Therefore, the FMCW reflectometer must be capable of detecting and capturing such very fast ongoing procedures. This is challenging and new, since most FMCW applications deal with targets that are moving at comparably low speeds. Measuring such fast varying

targets requires a very fast swept TX signal on the order of microseconds to have a large amount of signals injected into the TL during the deployment process. Recalling (2.4) and (2.6), such fast swept TX signals enable the aimed for high update-rate and hence precise temporal resolution, in accordance with (2.7). Considering a sweep time on the order of microseconds, e.g., $T_s = 20 \mu\text{s}$, a number of 1000 chirps can be injected into the sensing TL, resulting in 1000 samples taken during one deployment process. For that reason, a matching signal source offering such agile chirp signals is needed.

In addition to a good temporal resolution, a high range resolution along the TL is required for detecting multiple bends and folds along the airbag's surface. A generic diver airbag has a maximum diameter in the unfolded state of about 65 cm. Folding and thereby bisecting its dimensions at least three to four times to fit into its housing leads to a scale on the order of 4 cm. In FMCW reflectometry, the range resolution or range cell size directly corresponds to the bandwidth of the employed TX signal [Stove 1992]. An aimed for range cell size below 3 cm to resolve the multiple folds of an airbag, when being fully packed, is equivalent to a bandwidth of several gigahertz of the TX signal, in accordance with (2.8).

While the system requirements for temporal and range resolution are pretty demanding, the maximum range distance of the reflectometer has to extend over several meters only. At test benches, the sensing TL with the airbag is in close proximity to the reflectometer. Together with the feed line, the overall length of both lines does not exceed a distance of 15 m. This short measurement range of several meters only results in moderate TX power requirements, as typical for such short-range reflectometers. Furthermore, a signal propagating along a TL suffers less attenuation than a signal propagating in free space. Another essential criterion for the application of detecting weakly reflective targets, such as those mentioned soft-faults due to bends along the TL, is the spurious-free dynamic range (SFDR) of the TX signal. Hard faults such as opens or shorts produce significant reflection coefficients, which can be detected reliably with several standard reflectometry techniques. However, detecting weakly reflective targets is challenging and requires a large SFDR of the TX signal and high receiver sensitivity.

Besides a large SFDR, a good phase noise performance of the TX signal is also essential for detecting soft-faults along a TL. Often, the signal source in FMCW radars or reflectometers is the most significant source for phase noise. Phase noise limits the sensitivity of the radar. It compromises the detection of weakly reflective targets since the noise sidebands of larger targets cover the response of smaller targets and also elevate the noise floor [Dao et al. 2013].

Another limiting factor in terms of range accuracy in FMCW radars and reflectometers is the prominent nonlinear relationship of frequency and time concerning the TX signal, also known as ramp-nonlinearities, often times associated with analog signal sources. Those nonlinearities lead to a degradation in range resolution by broadening the beat frequency spectrum, causing a non-constant beat frequency, making it hard to detect weakly reflective targets and perform precise measurements [Ayhan et al. 2016].

Another critical design consideration concerning the reflectometer is the frequency range of operation. Many standard cable and TL types have a significant loss at high frequen-

cies, and those losses increase with frequency. As a consequence, a relatively small operating frequency is desirable as opposed to multiple other radar applications. Such a low-frequency range of operation is accompanied by certain benefits in the manner of greater flexibility concerning the TL type. The variety of employable TL types increases because cables or TLs with moderate or even poor RF transmission characteristics can also be used when the frequency of operation is relatively small. Besides, the lower the frequency of operation, the fewer the losses along the TL, the better the wave guidance, and the less radiation occurs in the case of employing an open TL structure.

To achieve good and reliable measurement results with the reflectometer, the employed TL structure, working as the bend sensor for the airbag surface, needs to fulfill certain properties as well. Most importantly, its local characteristic impedance must react sensitively to mechanical deformation, bends, kinks, or flexing. Ideally and desirable would be a linear relationship between the degree of bending or deformation and the degree of its local change of impedance. Consequently, the current fold status of the airbag during deployment could be determined accurately. Moreover, the TL structure must be reversible and must not break during the folding and unfolding. The TL structure must also withstand the strong forces during deployment and resulting high temperatures. *Chapter 4* deals with possible sensing TL structures and their realizations designed or adapted for this airbag application.

In summary, the reflectometer system requirements comprise a fast-swept, broadband, highly linear, low phase noise TX chirp signal with high spectral purity and an operating frequency in the lower gigahertz region. In addition, a compact, portable, and robust housing with its own power supply and cooling units is aimed for, facilitating a stable, autonomous, and long-term operation for performing in-field measurements at test benches.

3.2 Frequency Synthesis and Multiplication Approach

3.2.1 Signal Generation in FMCW Radar

The quality and properties of the TX signal of an FMCW radar or reflectometer determine, for the most part over its measurement capabilities, accuracy, and sensitivity. Hence, the choice of a proper signal source is an essential step in its design process.

Relevant attributes like frequency range, output power, phase noise performance, spurious content, sweep time capabilities, stability, and costs must suit the given application. Commonly, analog signal sources for generating RF signals are employed in FMCW applications. They comprise, for example, voltage-controlled oscillators (VCOs), crystal oscillators, PLLs with an integrated VCO, or yttrium-iron-garnet (YIG) oscillator solutions. Although widely used in various applications, those analog signal sources and generation methods come along with certain drawbacks [Chenakin 2007; Skolnik 1990; Stove 2004]. The most popular constraint is the presence of a nonlinear relationship between frequency and time in ramp/sawtooth or triangular LFM chirp signals, when recalling Fig. 2.3 and Fig. 2.4. Those nonlinearities in the TX chirp signal are a significant obstacle as they

impair the range resolution by broadening the beat frequency spectrum, resulting in a non-constant beat frequency. This poses a problem in detecting weakly reflective and closely spaced targets and rules out the possibility of performing precise measurements [Jankiraman 2018; Meta et al. 2007].

To remedy this constraint, various linearization, correction, or compensation techniques, algorithms, and methods are reported in the literature, for instance, in [Anghel et al. 2014; Ayhan et al. 2016; Dao et al. 2013; Jiang et al. 2012; Komarov and Smolskiy 2003; Meta et al. 2007; Scheibelhofer et al. 2007]. Such techniques include employing PLL synthesizer concepts [Ayhan et al. 2016; Thurn et al. 2016], pre-distortion of VCOs [Bao 2015; Komarov and Smolskiy 2003; Scheibelhofer et al. 2007], DDS-driven PLLs [Dao et al. 2013; Scheibelhofer et al. 2007], or closed loop-compensation of VCOs [Gomez-Garcia et al. 2014].

However, those linearization techniques are accompanied by an increase in computational cost or hardware complexity and thereby financial expenses. Besides, they rule out the possibility of performing very fast swept chirp signals due to the inertia of the system. Especially PLL solutions are slow due to limited dynamics, system delay, and locking time, making it hard to implement broadband solutions together with fast sweeping times in the microsecond scale.

In addition to the need for linearization techniques, analog frequency sources also suffer under temperature drifts, susceptibility to aging problems, and often poor phase noise properties [Dao et al. 2013; Thurn et al. 2016]. On the other hand, analog sources can cover extensive frequency bandwidths in various high-frequency bands and are not restricted to lower frequency ranges, as are digital sources.

3.2.2 Digital Signal Generation

In recent decades, apart from analog signal sources, the direct use of DDS technology [Tierney et al. 1971] for signal generation has gained wide popularity in various FMCW radar applications. In the literature, several application examples in which DDS technology is exploited are reported, for instance, in [Aguasca et al. 2013; Ash et al. 2015; Balon et al. 2018; Dill et al. 2019; Gomez-Garcia et al. 2014; Jung et al. 2021; Kim et al. 2022; Li et al. 2012; Liu et al. 2009; Rodriguez-Morales et al. 2020; Stove 2004; Yan et al. 2017].

A DDS is a digital frequency synthesizer that fundamentally comprises of a phase accumulator, a look-up table, and a digital-to-analog converter (DAC). Together with essential input parameters, such as a reference clock signal and a tuning word, high precision, high resolution, and very agile analog output sinusoidal waveforms or other waveforms in frequency and phase can be generated. Profiting from its digital nature, DDS realizations are often available as a fully integrated, single-chip solution at a modest price. However, their most striking features for FMCW applications are the very fast sweeping and highly linear modulated chirp signal generation capabilities, exceptionally fine frequency resolution, and good phase noise performance compared to wideband analog frequency sources. The phase noise performance of a DDS is determined by the phase noise performance of

its clock frequency source. In addition to that, those DDS chips are temperature stable and immune against analog drifts or aging problems [Analog Devices 2022a; Chenakin 2007; Cordesses 2004a,b].

On the other hand, this technology comes with two main drawbacks, the limited usable bandwidth, and inherent spurious performance. Limitations of DDS technology arise from the performance limitations of the built-in DAC. The DAC diminishes the achievable SFDR due to the quantization process and DAC conversion errors. With today's DDS implementations on the market, an SFDR level of -50 dBc to -60 dBc can be achieved, while analog solutions can offer a larger SFDR. The typical sinc roll-off frequency response of the built-in DAC leads to an attenuation of the output signals at higher frequencies.

Furthermore, the maximum frequency and thus the maximum achievable bandwidth is limited by the Nyquist frequency of the DAC. Latest commercial solutions offer a maximum clock frequency of 3.5 GHz [Analog Devices 2022a]. Considering specific output power and spurious performance values, signals of up to approximately 40% of the Nyquist frequency are realizable, which results in a maximum operating frequency and maximum bandwidth of about 1.4 GHz [Balon et al. 2018; Chenakin 2007; Cordesses 2004a,b].

Bearing FMCW radar applications in mind, this maximum achievable bandwidth and particularly the relatively low frequency range in the megahertz to lower gigahertz range state a problem, since a large bandwidth of the TX signal is crucial for precise range measurements. Solutions to tackle these shortcomings are reported in the literature. To expand bandwidth and hence range resolution, analog multiplication approaches of a DDS-generated signal are performed, for example, in [Aguasca et al. 2013; Gomez-Garcia et al. 2014; Li et al. 2012; Lin et al. 2006; Yan et al. 2017]. Also, upconversion of a DDS-generated baseband signal in order to use it in higher frequency bands is reported, for instance, in [Aguasca et al. 2013; Balon et al. 2018; Kim et al. 2022; Lin et al. 2006; Liu et al. 2009; Park et al. 2019].

3.2.3 Frequency Multiplier Chain

Recalling the given application and the above-specified system requirements for the proposed FMCW reflectometer design, a signal generation based on DDS comes to mind. Except for a large signal bandwidth and a large SFDR, this technique is promising due to the mentioned advantages over other analog signal sources like perfect linearity, fast sweeping capabilities, phase noise performance, and moderate costs.

For that reason, in the scope of this work, various approaches were conducted to enlarge the bandwidth of a DDS-generated signal in order to employ it as the TX signal to perform fast chirp FMCW radar. Those bandwidth extension solutions are briefly described and motivated in the upcoming subsection. However, due to the results of those solutions and due to the insights gained over time and research, another approach was developed, conducted, fabricated, and put into practice.

A frequency multiplier chain comprising an up-conversion, an analog frequency quadru-

plication, and a subsequent down-conversion of a DDS-generated baseband signal was established. A block diagram representation of this chain can be seen in Fig. 3.2. In the following, a detailed explanation of the concept, considerations, and the implementation are provided. Similar approaches of such frequency multiplication implementations are found in the literature, for instance, in [Aguasca et al. 2013; Dill et al. 2019; Kim et al. 2022; Li et al. 2012; Yan et al. 2017]. The idea and a detailed explanation of this design have already been published in [Möhring et al. 2019a, 2022; Möhring et al. 2021].

In the design process of this chain, according circuit simulations were performed with the electronic design automation (EDA) software tool Advanced Design System (ADS) by Keysight Technologies [Keysight Technologies, Inc. 2022] and the numeric computing environment Matlab [The MathWorks, Inc. 2022] by MathWorks, Inc. to optimize, simulate, and test the behavior and interaction of several potential components. Especially, the non-linear behavior of mixers, amplifiers, or frequency multipliers was investigated, together with the impact of passive components like attenuators, filters, or isolators.

An evaluation board by Analog Devices of type AD9914 [Analog Devices 2022a] equipped with a 12 bit DAC and a DDS chip is employed as the signal source for the needed LFM chirp signal. Given the current market situation, this chip offers the largest possible clock rate of $f_{\text{clk}} = 3.5$ GHz and, by this means, the largest achievable signal bandwidth. Its reference clock signal with a frequency of $f_{\text{clk}} = 3.5$ GHz is supplied by a wideband synthesizer with an integrated low phase noise VCO realized as a PLL, also fabricated by Analog Devices of type ADF4351 [Analog Devices 2022b], as seen on the top left of Fig. 3.2. In this process, the DDS signal is swept from 0.15 GHz up to 1.45 GHz, offering a signal bandwidth of $B_{\text{DDS}} = 1.3$ GHz and an output power level of about +2 dBm down to -3 dBm within one chirp.

The maximum possible bandwidth is not exploited intentionally to have sufficient separation from the DC bin. This separation is needed for the subsequent up-conversion process so that the LO signal and the swept signal have a spacing of at least 0.15 GHz, while the upper and lower sidebands share a separation of not less than 0.3 GHz. In order to suppress the occurring Nyquist images of the built-in DAC, the DDS signal is, first of all, low-pass filtered. The selection of this filter considers the trade-off of not distorting the output power level of the DDS further but also suppressing the images as much as possible to preserve the inherent SFDR.

In the next step, a heterodyning process is employed to up-convert the signal into X-band with a passive double balanced mixer of type MM1-0312S by Marki Microwave. Another PLL with an integrated VCO by Analog Devices of type HMC764LP6CE is utilized to drive the LO port of the mixer with a frequency of $f_{\text{LO}_1} = 7.9$ GHz and an output power of about $P_{\text{LO}_1} = 15$ dBm. First, the DDS signal is attenuated by 18 dB prior to the mixing, to keep the power levels of the intermodulation products, the lower sideband, and all other spurious content due to mixing process in relation to the up-converted signal as small as possible. The resulting upconverted signal B_X in X-band now reaches from 8.05 GHz to 9.35 GHz.

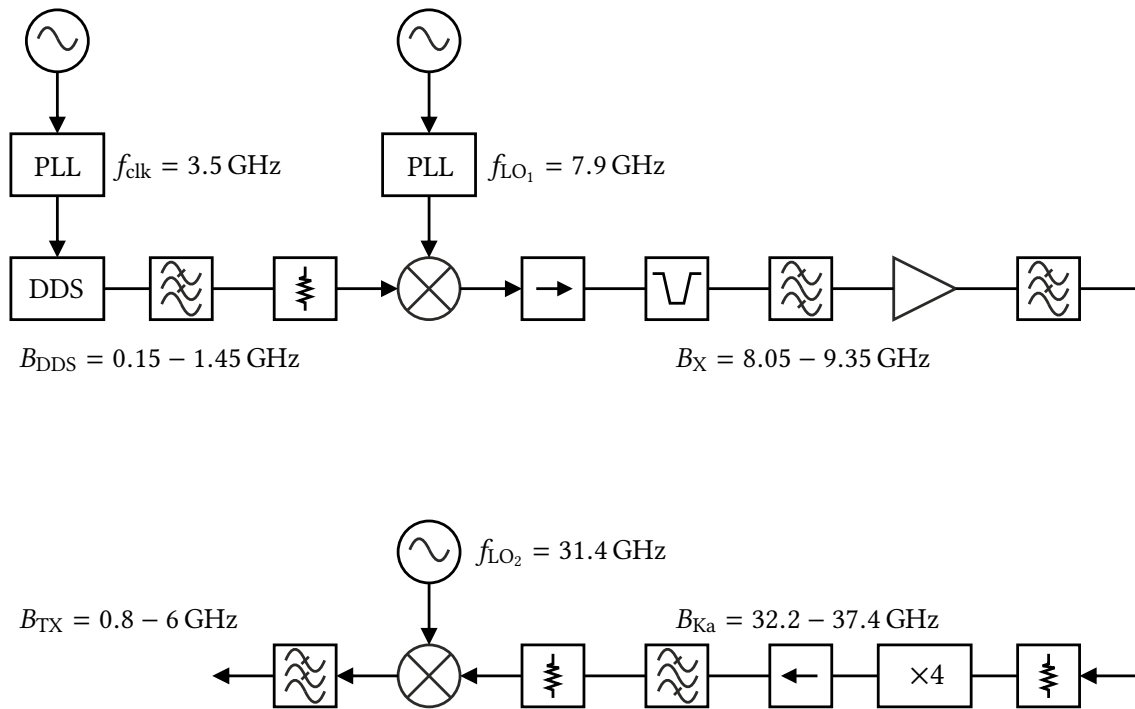


Fig. 3.2: Block diagram representation of TX signal generation using a DDS and a frequency quadruplication approach. The DDS-generated chirp of bandwidth B_{DDS} is upconverted into X-band, quadrupled into Ka-band, and downmixed into the P-band, now offering a bandwidth of $B_{TX} = 5.2$ GHz [Möhrling et al. 2021], © 2021 IEEE.

Custom-made combline cavity notch and band-pass filters by Wainwright Instruments GmbH are employed to suppress the undesired lower sideband, the feedthrough of the LO, and all other spurious content and mixing products in this heterodyning process. The notch filter is of order 10 with a center frequency equal to the frequency of the LO of $f_{LO_1} = 7.9$ GHz and rejects at least 60 dB of this break-through LO signal while offering a passband loss of not more than 1.5 dB.

The band-pass filter is of order 11 and offers a stopband rejection of at least 55 dB. This stopband reaches from DC to 7.7 GHz and from 10.5 GHz to 18 GHz, respectively. As a result of this, only the desired up-converted signal is precisely filtered out.

Special attention was paid to the design process of these two filters. These high-order filters offer a non-constant group-delay response through a nonlinear phase response, which can lead to frequency nonlinearities within the desired frequency range. The frequency ranges and filter characteristics are designed to keep the swept signal's nonlinear distortion effects to a minimum. However, a totally flat group delay of filters for such wideband signals is almost impossible to achieve [F. Perez-Martinez et al. 2001].

A single junction isolator by Pasternack Enterprises, Inc. of type PE8303 working in the upper C- and the whole X-band with an insertion loss of about 0.6 dB is incorporated to isolate/attenuate the band rejected content of the two filters from the output port of the mixer.

Due to an attenuation of the DDS-generated signal of 18 dB prior to the mixing process, the additional conversion loss of the mixing process, the insertion loss of the isolator, and the passband losses of the two filters, this X-band LFM signal now offers power values of about -40 dBm and below.

Two lined-up power amplifiers, manufactured by Mini-Circuits and Pasternack Enterprises, Inc., with a gain of 13 dB and 41 dB, respectively, reinforce the power of this signal. These two amplifiers are chosen because they meet the requirements regarding gain, gain-flatness, noise-figure (NF), and signal compression behavior.

After the two amplifiers, a suspended substrate stripline low-pass filter is employed to suppress the emerging harmonics of the two amplifiers. The filter offers a high stop-band rejection of typically 90 dB, and its stopband reaches up to 33 GHz. An additional attenuator is used to further down-regulate the power of this LFM signal in order to meet the specific and strict power level requirements of the succeeding active frequency quadrupler.

This wideband, active, amplified frequency quadrupler by Marki Microwave of type AQA-2040 is designed to maximize the fourth harmonics output power of its input signal. Simultaneously, it minimizes the power of the emerging first-, second-, third-, and fifth-order harmonics. The LFM input signal in X-band B_X is quadrupled into Ka-band, now offering a signal bandwidth of 5.2 GHz, reaching from 32.2 GHz to 37.4 GHz. The LFM output signal is further coupled into a Ka-band hollow waveguide structure of type WR-28 employing a coaxial-waveguide transition. The signal transmission in the Ka-band frequency range is realized in hollow waveguide technology because of smaller losses, its simple and shielded environment, and a wider variety of available RF equipment compared to coaxial components in that frequency range.

The desired 4th harmonic is filtered out by a waveguide band-pass filter particularly designed by SAGE Millimeter, Inc. It offers a very flat group delay in the passband, a minimum rejection of 45 dB in the stopband, which is specified up to 46 GHz, and an insertion loss of under 3 dB. An isolator by Mi-Wave with isolation values of typically 25 dB and an insertion loss of about 1 dB is placed before the band-pass filter to isolate its band-rejected content from the output port of the power sensible quadrupler.

A second heterodyning process is employed to down-convert the broadband LFM signal from the Ka-band to a signal starting in P-band. Now, a broadband, balanced mixer working in full Ka-band is utilized. This mixer is based on GaAs Schottky beam-lead

diodes and offers a moderate conversion loss of about 11 dB. Both the LO and RF ports are equipped with WR-28 waveguide connectors, while the IF port is realized with an SMA connector. The needed LO signal of frequency $f_{LO_2} = 31.4$ GHz is generated by a GaAs Gunn high quality factor cavity oscillator which offers good phase noise performance together with high power stability with an output power of $P_{LO_2} = 12$ dBm and a low power harmonic emission. The mixer and the second LO source are also manufactured and purchased from SAGE Millimeter, Inc.

By mixing the Ka-band signal B_{Ka} with the second LO of frequency $f_{LO_2} = 31.4$ GHz, the desired, broadband LFM TX signal, B_{TX} for this FMCW reflectometer is achieved. It now reaches from 0.8 GHz to 6 GHz. Behind the IF port of the mixer, a low-pass filter is employed to suppress any higher frequency content from this TX signal, like harmonics, intermodulation products, or the feedthrough LO signal.

To visualize this process further, a schematic frequency plan of the frequency multiplier chain is depicted in Fig. 3.3. Starting at the top left of this figure, the output signal of the DDS is first low-pass filtered and then up-converted. The filter curves are sketched schematically in blue, while the two LOs are expressed by two black vertical lines. Before the quadruplication process, the X-band signal is precisely band-pass and the feedthrough LO is accurately notch filtered. The quadruplication is marked by the green arrow, while a black arrow denotes up- and down-conversion. The second row of Fig. 3.3 illustrates the band-pass filtering in Ka-band before down-conversion to P-band through a second LO. A final low-pass filter cuts out the desired signal, now reaching from 0.8 GHz to 6 GHz.

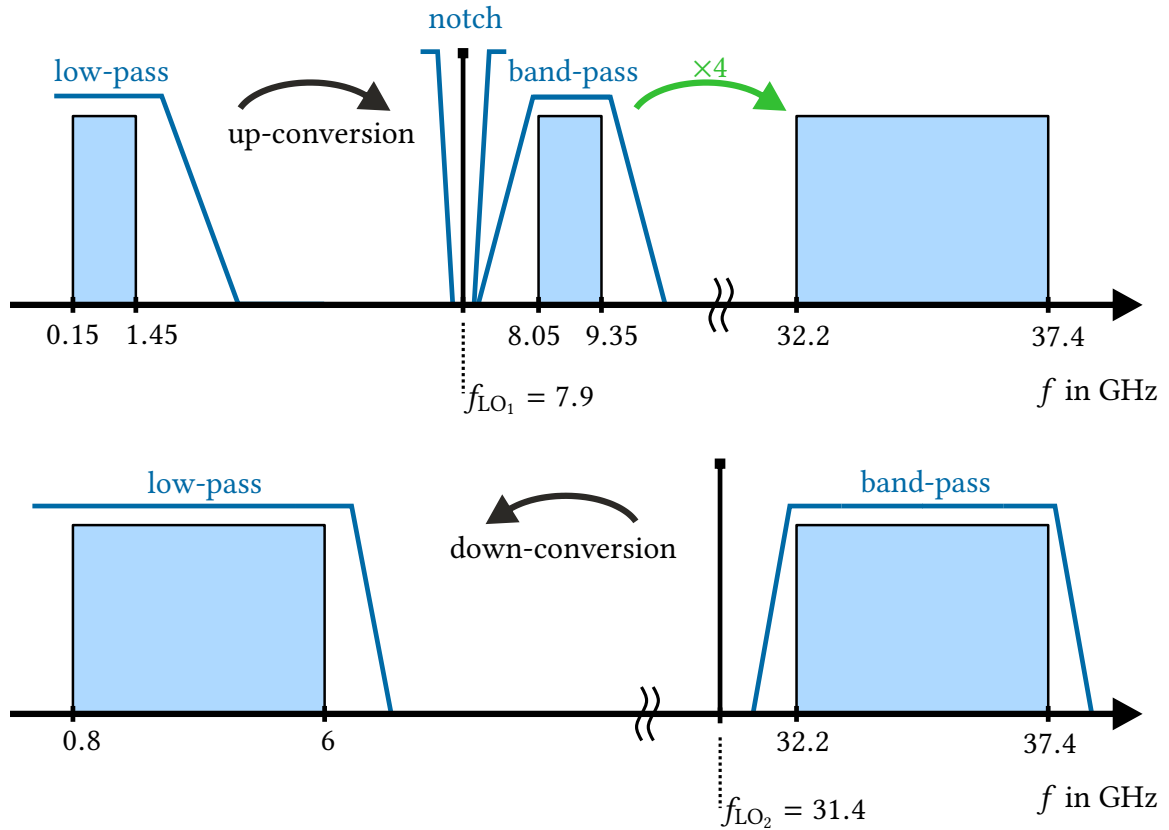


Fig. 3.3: Schematic frequency plan of quadruplication approach. The low-pass filtered DDS output signal is up-converted into X-band and subsequently quadrupled into Ka-band. Notch and band-pass filters suppress the feedthrough of the first LO, $f_{LO_1} = 7.9$ GHz, harmonics, the lower sideband, and intermodulation products. A Ka-band band-pass filter filters out the desired fourth harmonic before the signal is downmixed into P-band using a second LO, $f_{LO_2} = 31.4$ GHz. A final low-pass filter suppresses any spurious higher frequency content above 6.5 GHz [Möhring et al. 2019a].

3.2.4 Additional Solutions for Bandwidth Extension

Before implementing the DDS-driven frequency multiplier chain, various bandwidth enhancement solutions were conducted to enlarge the inherent bandwidth of a DDS while preserving its favorable signal features for the application, such as fast sweep time, good SFDR, low phase noise, or high ramp linearity.

However, the designed analog DDS-driven frequency multiplier chain outperformed those possible system architectures and bandwidth extension solutions. For the sake of completeness and for providing scientific insights, those solutions are briefly explained and motivated in this section. Detailed descriptions of the experiential setups and complete results are excluded from this thesis due to conciseness and brevity reasons.

Direct Duplication and Self-Mixing

A block diagram represents the four additional methods as suggested and conducted in this work of directly enlarging the bandwidth of a DDS, on the one hand, or shifting the DDS signal from baseband into a higher frequency band for further processing like multiplication, on the other hand, are depicted in Fig. 3.4.

On the top left of Fig. 3.4, a direct frequency duplication in baseband is shown (I), while on the bottom left, a self-mixing approach employing a Gilbert cell-based mixer is depicted (III). On the top right of Fig. 3.4, a super-Nyquist operation (SNO) is shown (II) by exploiting a spectral image of the fundamental DDS signal in its 3rd Nyquist zone. In contrast, the bottom right displays an IQ up-conversion method employing a single-sideband mixer (SSM) (IV).

In all four approaches, the DDS chip from Analog Devices of type AD9914 [Analog Devices 2022a] was used as a signal source together with a reference clock realized as a PLL of type ADF4351 [Analog Devices 2022b] from the same company.

The direct duplication of a DDS signal in baseband, as performed for instance by [Dill et al. 2019], is done here by first low-pass filtering the DDS output, which is swept from 100 MHz to 1.45 GHz, to suppress the occurring Nyquist images of the built-in DAC. Subsequently, the signal is duplicated passively employing diode-based frequency multipliers/doublers, such as the FK-3000+ by Mini-Circuits, the FX-05-410 by Pulsar, or the FD26C by Macom. By this means, duplication of bandwidth is achieved. However, due to the limited suppression of other emerging harmonics like the nearby first, third, and fourth-order harmonics, the SFDR of the signal is heavily degraded. Thereby, a worst-case separation of the desired second-order harmonic to other spurious in-band harmonics of only -10 dBc is noticed. The duplication of bandwidth is accompanied by a severe impairment of the SFDR, which can not be borne in this application due to high demands concerning sensitivity. However, this technique might be beneficial for other applications with fewer demands regarding the SFDR or signal bandwidth.

A similar outcome was obtained by the self-mixing approach, as outlined on the bottom left of Fig. 3.4. In this process, the DDS output signal is again low-pass filtered and then divided by a resistive passive power divider of type ZFRSC-42+ by Mini-Circuits. Other

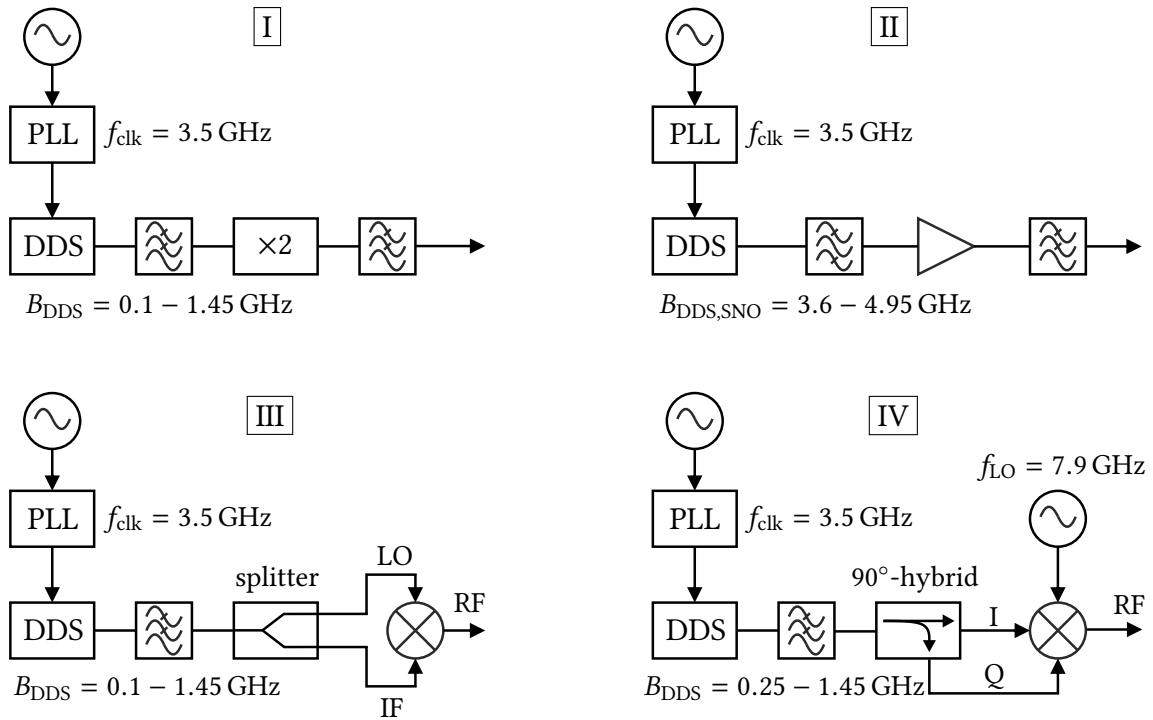


Fig. 3.4: Block diagram representation of bandwidth enhancement approaches employing a DDS as a signal source. Those methods comprise a direct multiplication in base-band (I), a super-Nyquist operation (II), self-mixing (III), and IQ up-conversion with a SSM (IV).

splitter or coupler structures can also be used for this. However, resistive dividers are capable of covering such wide frequency ranges at such low frequencies at the cost of high losses. Afterwards, these two in-phase signals are fed to the LO and the IF port, respectively, of a Gilbert cell-based active mixer by Analog Devices of type ADL5801 [Analog Devices 2022c]. This mixer incorporates an integrated LO amplifier which is needed due to the low power level of the LO signal of about -10 dBm after the splitting and filtering. This approach also results in a duplication of bandwidth at the RF port of the mixer. As in the case before, the spurious harmonics of the particular mixing products also impair the SFDR of the RF signal severely. This results from the relatively low starting frequency of the DDS chirp of 100 MHz and the wide sweeping range of the signal covering almost 4 octaves up to 1450 MHz . Due to the little separation to the DC bin of only 100 MHz , the LO signal, as well as the lower sideband, are in close proximity

to the intended mixing product. Especially at the lower frequency bound, the undesired spurious harmonics are closely adjacent to the intended mixing product or duplication products.

Therefore, bearing this issue in mind, the next two techniques, as shown on the right in Fig. 3.4 under II and IV, aim to increase the separation of the signal to the DC bin due to a shift into a higher frequency band and thereby reducing the number of octaves over which one chirp is spanning while preserving the inherent DDS bandwidth of 1350 MHz.

Super-Nyquist Operation and IQ Mixing

The usage of higher Nyquist zones besides the first one is also known as super-Nyquist operation (SNO) and is suggested in [Gentile 2007]. Other groups, for instance, [Kim et al. 2022], [Aguasca et al. 2013], and [Ash et al. 2015], also utilized the SNO mode of a DDS to reach higher frequencies. In the SNO, not the fundamental signal in the first Nyquist zone is used, but instead its respective spectral images in higher-order Nyquist zones.

In this work, the second spectral image in the 3rd Nyquist zone is utilized, which reaches from 3.6 GHz to 4.95 GHz, spanning over less than one octave and offering sufficient separation to the DC bin. This image corresponds to the fundamental output signal of the DDS spanning from 100 MHz to 1450 MHz. Band-pass filters are used to filter out this second image and suppress the fundamental signal and remaining undesired images, as seen in II in Fig. 3.4. Thereby, band-pass filters by Mini-Circuits of type VBF-4440+ and VBFZ-3590-S+ are employed, which offer pass-bands in the desired frequency range of the second image.

Two shortcomings are observed when operating a DDS in the SNO mode. Firstly, due to the sinc-roll off response of the built-in DAC, this second Nyquist image is highly attenuated compared to the fundamental signal, which is why a subsequent power amplifier is depicted in Fig. 3.4. In addition to that, the sinc-roll off frequency response worsens the SFDR of the whole chirp. Various intermodulation products are present in the 3rd Nyquist zone, impairing the SFDR. Thereby, a worst-case SFDR of about -30 dBc was measured within one chirp spanning from 3.6 GHz to 4.95 GHz. As also stated by [Gentile 2007] and [Aguasca et al. 2013], the overall SFDR performance decreases with an increasing number of Nyquist zones.

Summing up, the SNO mode is a powerful method when employing DDS for signal generation. However, it is rather suited for small bandwidths or single tone operation than for the usage over large signal bandwidths due to the limits regarding the SFDR. Since this application demands a large amount of bandwidth in conjunction with a large SFDR, the SNO mode not further pursued in this work.

The final approach, depicted in Fig. 3.4 under IV, aims to exploit the advantages of an in-phase and quadrature (IQ) mixer when used as a single-sideband mixer (SSM) for an upconversion process of the DDS baseband signal into X-band.

SSMs are IQ mixers fed by an IF signal split into an I and a Q component. This is done

in order to suppress the lower sideband in an upconversion process due to phase cancellation. Especially at lower IF frequencies, SSMs are very useful since they reduce or sometimes even remove the filter needs after the upconversion process. Thereby, the amount of sideband suppression of an SSM hardly depends on the amplitude and phase balance of the IF signal [Henderson and Cook 1985; Jorgesen 2018].

Therefore, the DDS signal is first of all split into an I and a Q component using a 90° -hybrid coupler. This coupler is custom made by TTE Europe for the given frequency range spanning from 250 MHz up to 1450 MHz. A lower frequency limit below 250 MHz was aimed for but not achievable. It offers a mean coupling value of 3 dB with a corresponding amplitude balance of up to ± 1.2 dB, a phase balance of up to $\pm 3^\circ$, an insertion loss of 0.5 dB, and a minimum isolation of 20 dB.

The broadband and passive IQ mixer used in this work, the MMIQ-0520L by Marki Microwave, offers a sideband suppression of up to 40 dB when used as an SSM. The needed LO signal for upconversion offers a frequency of 7.9 GHz and is supplied by a signal generator SMR40 by Rohde & Schwarz with a corresponding power level of 11 dBm. After performing several measurements and sweeping the DDS from 250 MHz to 1450 MHz, constituting the IF signal, a sideband suppression was well seen after the upconversion process into X-band.

However, due to the amplitude and phase imbalance of the I and Q signal resulting from the employed 90° -hybrid coupler, the desired upper and undesired lower sideband are also strongly fluctuating in power. As a consequence, no constant power level of the upper sideband was noticed as needed for the application. Though, it needs to be stated that a perfect amplitude and phase balance over such a large bandwidth is challenging to achieve with a coupler structure.

A remedy would be using two synchronized DDS chips with a fixed phase shift of 90° for an SSM upconversion process instead of a hybrid coupler. However, according to the manufacturer, the here used AD9914 DDS chip does not support multi-chip synchronization. Furthermore, besides this strong fluctuation in power of the upper sideband, the spurious mixing product of $2 \times \text{IF}$, $1 \times \text{LO}$ was suppressed only by about 40 dB, thereby degrading the overall SFDR. Due to the strong fluctuation in power of the desired upper sideband and the degraded SFDR, this SSM upconversion strategy was not further pursued in this work. Upconverting a DDS generated signal utilizing an SSM, has also been done in [Balon et al. 2018].

Due to the outcome of these additional four solutions for the given application and corresponding requirements, the DDS-driven frequency multiplier chain was set up and put into practice. Overall, the DDS-driven frequency multiplier chain outperformed the suggested four bandwidth extension solutions regarding the airbag application. Especially the SFDR suffered due to spurious harmonics and intermodulation products caused by these four techniques. Also, a signal bandwidth of the aimed for several gigahertz bandwidth was not feasible to achieve. However, these approaches might be convenient and useful for other applications, especially those with smaller requirements concerning signal bandwidth.

3.3 FMCW System Concept and Hardware Realization

3.3.1 System Concept

The system concept and the design aspects of the FMCW reflectometer are presented and described. The DDS generated and by means of the frequency multiplier chain quadrupled LFM signal functions as the TX signal in the reflectometer. A block diagram of the realized FMCW reflectometer instrument is seen in Fig. 3.5. The TX signal synthesis of the block diagram of Fig. 3.2 is represented by the top left block of Fig. 3.5.

A coherent, homodyne system architecture is employed, meaning that the same signal is used as the TX signal and the LO signal of the receiving mixer, respectively [Piper 1993, 1995; Skolnik 1990].

With the aid of employing two broadband directional couplers placed back-to-back, also known as a dual-directional coupler, the TX signal is coupled into the sensing TL and into the receiving mixer as well. An antenna can also be employed instead of the sensing TL. In this case, a monostatic FMCW radar is created instead of an FMCW reflectometer. In many monostatic FMCW radars or reflectometers, a circulator working as a duplexer is employed to isolate the RX signal from the TX signal. By this means, the TX and the RX can share the same TL or antenna [Lin et al. 2006]. However, due to the large signal bandwidth of our reflectometer of over 5.2 GHz spanning over almost three octaves, circulators are commercially not available and unfeasible to fabricate with appropriate requirements regarding the isolation. Instead, the dual-directional-coupler structure is used as a substitute.

The coupling value of 6 dB of the first coupler is chosen to meet the power requirements of the LO port of the mixer. The second coupler has a coupling value of 3 dB to keep the overall losses of the system architecture at a minimum since any reflected signal from a target has to pass the coupler two times. The mainline insertion loss of the two couplers adds up to about 4.5 dB. Thereby, 1.5 dB account for the 6 dB-coupler and another 3 dB for the 3 dB-coupler. The two couplers were custom-made for this application. Student projects aimed to investigate, design, and manufacture such broadband couplers were carried out in the frame of this work.

Measurements with a VNA were performed to investigate transmission, coupling, and isolation properties of the dual-directional-coupler, where a VNA of model ZVA 24 by Rohde & Schwarz together with the calibration unit of model ZV-Z52 were used. The port description of the passive and reciprocal 4-port can be seen in Fig. 3.5. The crucial S -parameters for the reflectometer in the frequency range from 500 MHz to 6.5 GHz are depicted in Fig. 3.6. However, the employed TX signal only ranges from 800 MHz to 6 GHz.

The TX signal $s_{TX}(t)$ undergoes an attenuation, represented by S_{21} , when passing through both couplers from port 1 to port 2, accounting for about -5 dB. The TX signal is also coupled to the LO port, power driving this port of the mixer, represented by S_{41} . The losses are a bit larger than the aimed for -6 dB. In addition to that, the S -parameter S_{32} ,

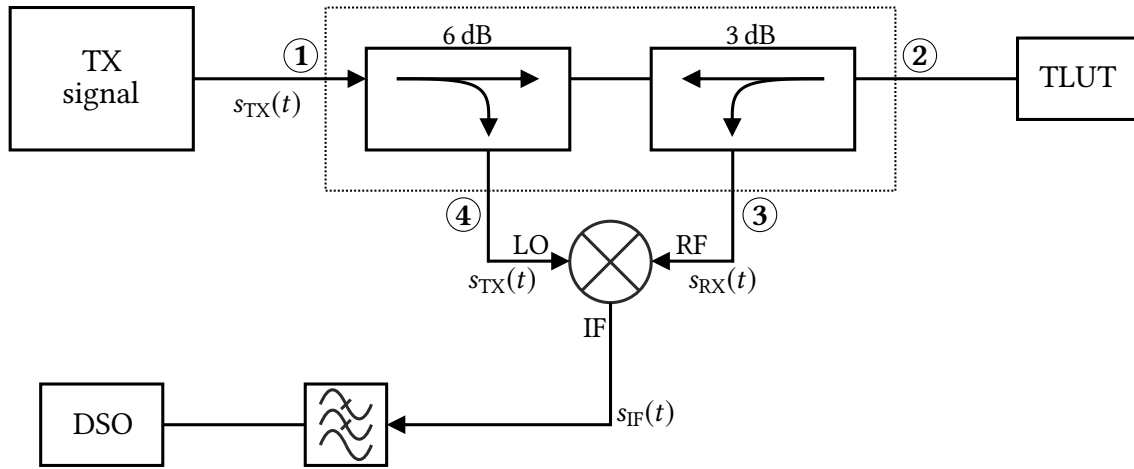


Fig. 3.5: Block diagram representation of FMCW reflectometer with according port descriptions. The TX signal is coupled through two directional couplers with coupling values of 6 dB and 3 dB, respectively, into the TLUT and the receiving mixer's LO port. Each bend or discontinuity along the TLUT results in a reflection and an RF signal mixed with the TX signal. A final DSO or ADC records the data and converts it into the digital-domain for further processing [Möhrling et al. 2021], © 2021 IEEE.

characterizes the path from port 2 to port 3. Occurring discontinuities along the TLUT resulting in partially reflected signals are directed to the RF port of the receiving mixer and experience an attenuation related to S_{32} of about -3 dB.

Besides the presented coupling and transmission losses, the isolation properties of the coupler structure are of particular interest in order to handle weakly reflective targets and hence weak reflected signals. A significant drawback of FMCW systems is the direct spillover of the TX signal into the RX path, also known as TX-to-RX-spillover or TX-leakage. This drawback is especially noticeable for the short-ranges since the first few range cells are affected by this inevitable spillover.

Commonly, monostatic homodyne FMCW systems employ circulators instead of directional couplers to separate the TX from the RX path. Limited and insufficient isolation of these circulator ports results in a degradation of the system performance. Therefore, the literature reports various approaches to increase the isolation of circulators and so mitigate the common TX-leakage problem [Li and Wu 2008]. Typical isolation values of circulators are on the order of 25 dB to 30 dB [Li and Wu 2008; Lin et al. 2006].

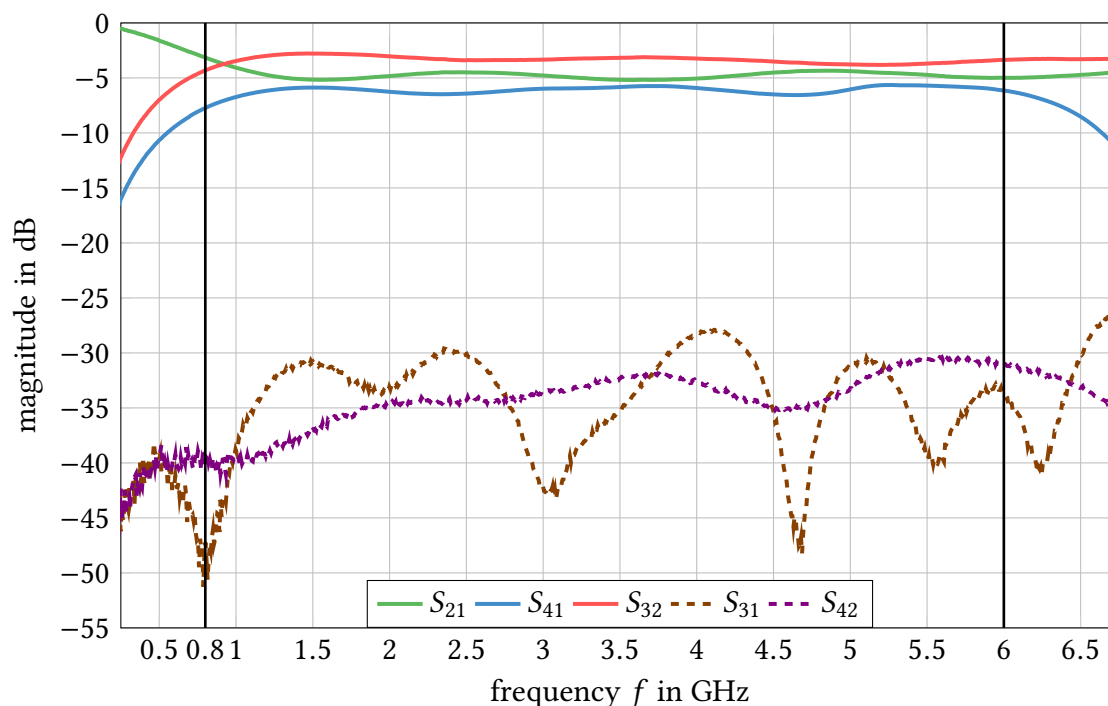


Fig. 3.6: Measured S -parameters of two-coupler structure arranged back-to-back with the port description according to Fig. 3.5, revealing the transmission, coupling, and isolation properties of the reflectometer setup [Möhring et al. 2021].

After all, those isolation values can vary depending on the employed frequency range and bandwidth. In [Porrnzl et al. 2015], an isolation of 16 dB over a large signal bandwidth of 8 GHz employing a quasi-circulator is reported. At the same time, [Huang et al. 2012] reports isolation values of 30 dB and better also by utilizing a quasi-circulator. In [Lin et al. 2006], an adaptive DSP-based leakage cancellation method is suggested ensuring more than 30 dB isolation over a signal bandwidth of 1.7 GHz in Ka-band.

In this system, the receiving port 3 of the mixer is isolated from the TX signal port 1 by at least -27 dB when inspecting S_{31} of Fig. 3.6. In certain frequency ranges, it offers values below -40 dB. These good isolation values of the TX leakage are promising, considering the large signal bandwidth of 5.2 GHz spanning over almost three octaves and the lower frequency limit in the UHF band. The isolation of port 2 and port 4 is denoted by S_{42} . This isolation describes the attenuation of an occurring RX signal due to targets when entering the LO path via the coupler structure. This isolation is throughout better than -30 dB. The isolation of the ports 4 and 3, characterized by S_{43} , is not shown in Fig. 3.6

since they reveal throughout low values of -55 dB and below. In summary, the good isolation properties of the coupler structure are beneficial for the measurement accuracy of the reflectometer. However, due to two couplers, relatively high transmission and coupling losses are to be taken into account. On the other hand, these are tolerable due to the short-range application.

Due to the homodyne principle, the IF signal $s_{IF}(t)$, containing the range and velocity information of the respective targets, is created by mixing the TX signal $s_{TX}(t)$ with the respective RX signals $s_{RX}(t)$. An active, broadband, double-balanced mixer with an integrated LO amplifier by Analog Devices of model ADL5801 [Analog Devices 2022c] is used as the receiving mixer. This mixer is chosen because of its integrated LO amplifier, which compensates for the present variations in power of the LO signal due to the coupler and the power variations of the TX signal itself, as shown by S_{41} in Fig. 3.6. On top of that, the broadband mixer offers a good input linearity, an conversion gain of about 2 dB, and provides good LO-to-RF and LO-to-IF leakage of better than -40 dB.

A connected low-pass filter suppresses any high-frequency content of the down-converted IF signal. An ADC or DSO records the low-pass filtered data in the time-domain from reflections due to the faults and discontinuities of the TLUT. Further measurement data processing is done by DSP techniques and via the software tool Matlab [The MathWorks, Inc. 2022]. In this application, the phase information of the reflected signals is not of interest. Otherwise, the standard mixer can be replaced easily by an IQ mixer to retrieve the phase information.

3.3.2 Hardware Realization

The FMCW reflectometer is designed as a portable measurement device for in-field monitoring of airbag deployment processes. Moreover, it can be used for various other reflectometry applications or radar tasks in the short-range.

Therefore, a portable and compact aluminum housing was fabricated, which contains all needed components comprising the RF and all supporting DC or cooling devices. The housing has dimensions of 440 mm \times 380 mm \times 250 mm and is divided into two levels. The lower level is equipped with all the needed DC supply structures, and the top-level houses the RF equipment. For performing measurements, an additional PC is needed that controls the DDS, the PLLs, the triggering, and the ADC/DSO, which record and process the data.

3.3.3 Lower Level of Instrument: DC Supply Unit

A picture of the lower level of the instrument is depicted in Fig. 3.7. The DC supply unit is seen there, comprising two switched power supplies, multiple printed circuit boards (PCB), cooling fans, and wiring. The layouts of the FR-4 PCBs were designed with the EDA tool EAGLE [Autodesk 2022] and fabricated with an LPKF laser structurer [LPKF

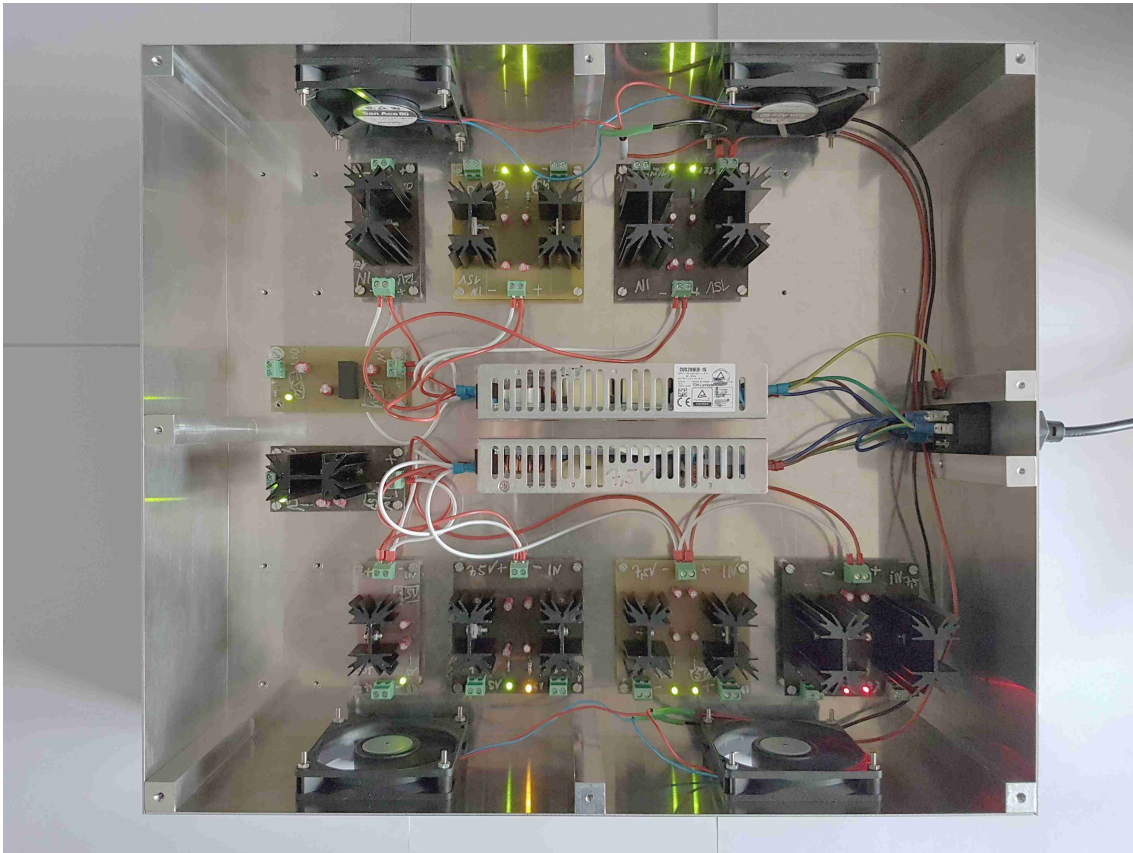


Fig. 3.7: Picture of the lower level of the FMCW reflectometer, showing the DC supply unit. Two switched power supplies placed in the middle voltage convert the domestic AC power and supply several PCBs equipped with LDO or DC-DC-converting circuits. Together with smoothing/decoupling capacitors, heat sinks, and status indicating LEDs, stable and clean DC supply voltages for the various RF components are established.

Laser & Electronics AG 2022] at the Chair of High-Frequency Engineering (HFT) of the TUM. A switch with a C14 connector, including a fuse, connects the device to the domestic power grid. The switched power supplies are employed to transform the AC domestic supply voltage of 230 V (50 Hz) to DC values of 7.5 V and 15 V, respectively. The various PCBs are equipped with linear low-dropout (LDO) voltage regulators and DC-DC-converter circuits, all realized in a through-hole technology mounting scheme. Additional electrolytic capacitors are employed as decoupling, smoothing, and bulk ca-

capacitors to further stabilize, smooth, buffer, and noise filter these voltages. The regulator circuits on the PCBs are also equipped with heat-sinks and status indicating LEDs. All in all, the PCBs enable a long-term and stable operation and compensate for possible variations and disturbances in the power grid [Rincon-Mora 2009].

The circuitry is employed and needed because many RF components are sensitive to power supply noise. Noise or other spurious content arising from DC sources like switching-noise of switched power supplies can degrade the performance of the RF components and the whole circuit. It can lead to additional spurious signals in the RF domain [Aguasca et al. 2013]. LDO and DC-DC-converter circuits in conjunction with smoothing capacitors prevent that power supply noise from entering the RF components. In particular, the DDS-clock or other signal sources are very sensitive to such noise [Ayhan et al. 2016]. The various RF components housed on the upper level of the instrument need over 12 stable, constant, and accurate power supply voltages reaching from 1.8 V up to 12 V. One negative supply voltage of -5 V is also needed for balancing the active frequency quadrupler. The RF amplifiers draw peak currents of close to 1.5 A, resulting in a power consumption of 18 W. The maximum occurring heat loss in the LDO circuits adds up to about 5 W. Various passive heat sinks dissipate this heat loss within the LDO and DC-DC-converter circuits in combination with the active fans in the lower level of the instrument [Beaty and Fink 2012].

The thermal resistance R_{th} of the respective passive heat sinks needed to dissipate the thermal energy is calculated according to the thermal-electrical analogy. By this means, extruded heat sinks with a thermal resistance of down to $R_{th} = 4.5$ K/W are chosen and employed to the packaging (TO-220) of the LDOs [Shabany 2010]. These heat sinks are necessary so that the maximum allowable operating temperature of the LDOs and DC-DC-converters is never exceeded.

The cables from the lower level, carrying the supply for the various RF components to the upper level of the instrument, are twisted and equipped with ferrite cores for electromagnetic interference (EMI) reasons. The ferrite core is a special type of an electromagnetic choke that suppresses unintended high-frequency noise in the DC supply. The twisting of wires is performed to reduce its susceptibility to noise, achieve magnetic field cancellation, and to reduce electric field radiation or pickup [Beaty and Fink 2012].

3.3.4 Upper Level of Instrument: RF Components

A picture of the upper level of the instrument depicting the employed RF components is seen in Fig. 3.8. All parts of the frequency multiplier chain of Fig. 3.2 can be seen there, as well as the TX and RX branch together with the receiving mixer of Fig. 3.5.

For testing and modular adaption purposes, in addition to their widespread commercial availability, discrete components with primarily 50 Ω -SMA-connectors are used. Little holes are drilled into the aluminum plate on which the components are mounted so that the DC supply cables can be fed through from the level below. Covering aluminum walls

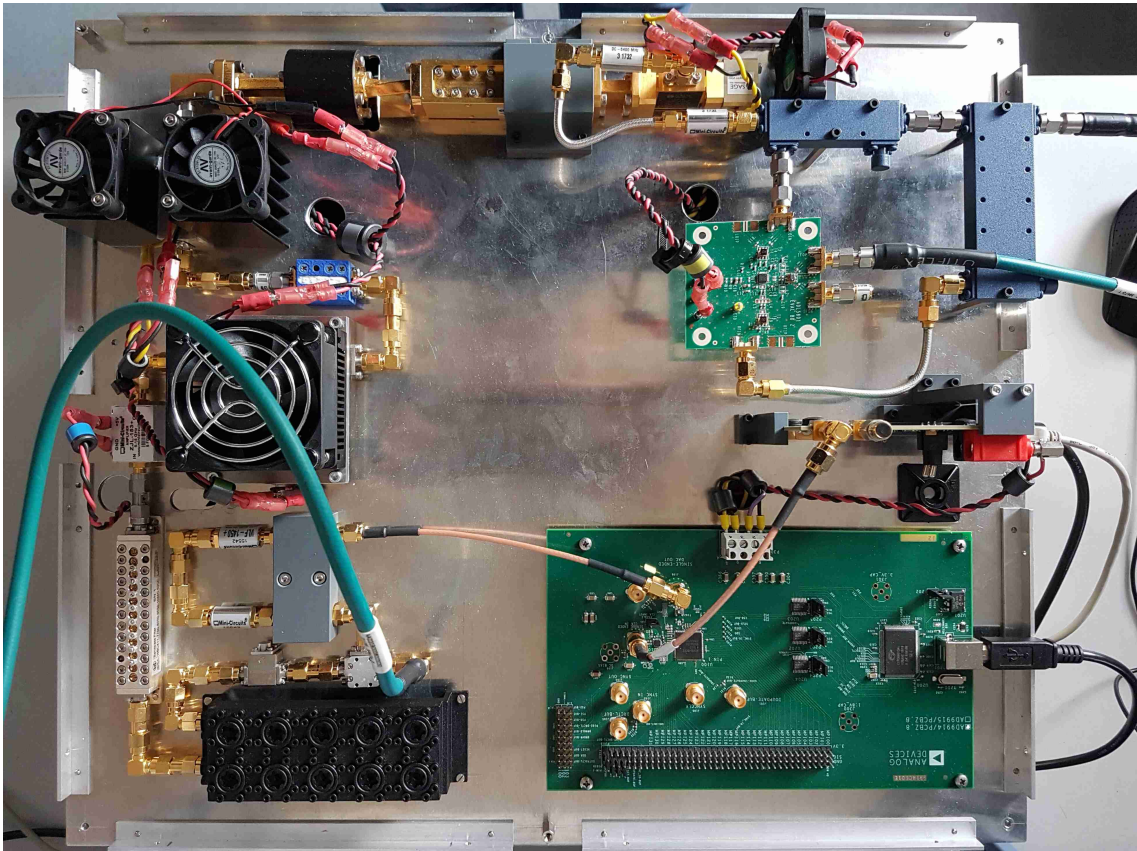


Fig. 3.8: Picture of the upper level of the FMCW reflectometer containing all employed RF hardware components. The DDS board and its reference clock are seen on the bottom right, while the bottom left shows the up-conversion mixer with the followed notch and band-pass filters. The devices with the fans on top are the two amplifiers and the active quadrupler. The Ka-band parts are seen on the top, such as the coaxial-to-waveguide transition, the isolator, the band-pass filter, the down-converting mixer, and the GaAs Gunn oscillator. The top right shows the two directional couplers and the active receiving mixer.

are attached to all four sides and the top of the instrument. However, the wall on the right-hand side is equipped with holes to connect the domestic power cable, the control cables for the DDS, and the two PLLs, the output port of the receiving mixer, and the TLUT to the instrument.

On the bottom right of Fig. 3.8, the DDS evaluation board of type AD9914 by Analog

Devices [Analog Devices 2022a] can be seen together with its reference clock of type ADF4351 [Analog Devices 2022b] placed right next to it but mounted vertically. A coaxial cable carries the DDS output signal to the subsequent low-pass filters and attenuators, visible as the golden parts in a u-shaped arrangement on the bottom left of Fig. 3.8.

The two following quadratic, silver components are the mixer used for up-conversion and the isolator. The high-order, custom-made cavity notch and band-pass filters can be seen as the black- and silver-colored, rectangular-shaped devices on the bottom left of Fig. 3.8.

The active frequency quadrupler is seen on the top left of the picture together with the attached heat sinks and the two fans on top of it. Arranged just below is the high power amplifier which is cooled by a single large fan. The parts realized in WR28 waveguide technology are seen in the top row of Fig. 3.8, comprising the coaxial-to-waveguide transition, a subsequent isolator, a band-pass filter, and a down-converting mixer, which is fed by the GaAs Gunn oscillator acting as the LO.

The two blue parts on the top right show the two directional couplers with coupling values of 3 dB and 6 dB, respectively, together with an attached generic TLUT and the active receiving mixer. A picture showing the FMCW reflectometer with an exemplary driver airbag and a commercial coaxial sensing TL is depicted in Fig. 3.9. The image shows the actual measurement setup, except for the feeding line, for monitoring airbag deployment scenarios as indicated with the block diagram of Fig. 3.1.



Fig. 3.9: FMCW reflectometer instrument in the laboratory with exemplary unfolded driver airbag and a commercial coaxial sensing TL attached to it, functioning as the bend sensor. A match terminates the TL.

3.4 System Specifications and TX Signal Quality

In order to assess the characteristics and quality of the TX signal of the FMCW reflectometer and in order to investigate the influence of the proposed frequency multiplier chain, measurements at the output of the chain were performed with a high-speed DSO by Teledyne LeCroy of type WaveMaster 808Zi-A [LeCroy Corporation 2022]. This DSO offers a sampling rate of up to 40 GS/s, a bandwidth of 8 GHz, and a memory depth of 20 MS. The recorded data is post-processed in Matlab to display the TX signal chirps and investigate them further in terms of linearity, SFDR, output power, and possible other spurious effects. In this process, an LFM chirp signal is generated with a bandwidth of 5.2 GHz reaching from 0.8 GHz to 6 GHz and a generic sweep time of $T_s = 400 \mu\text{s}$. The

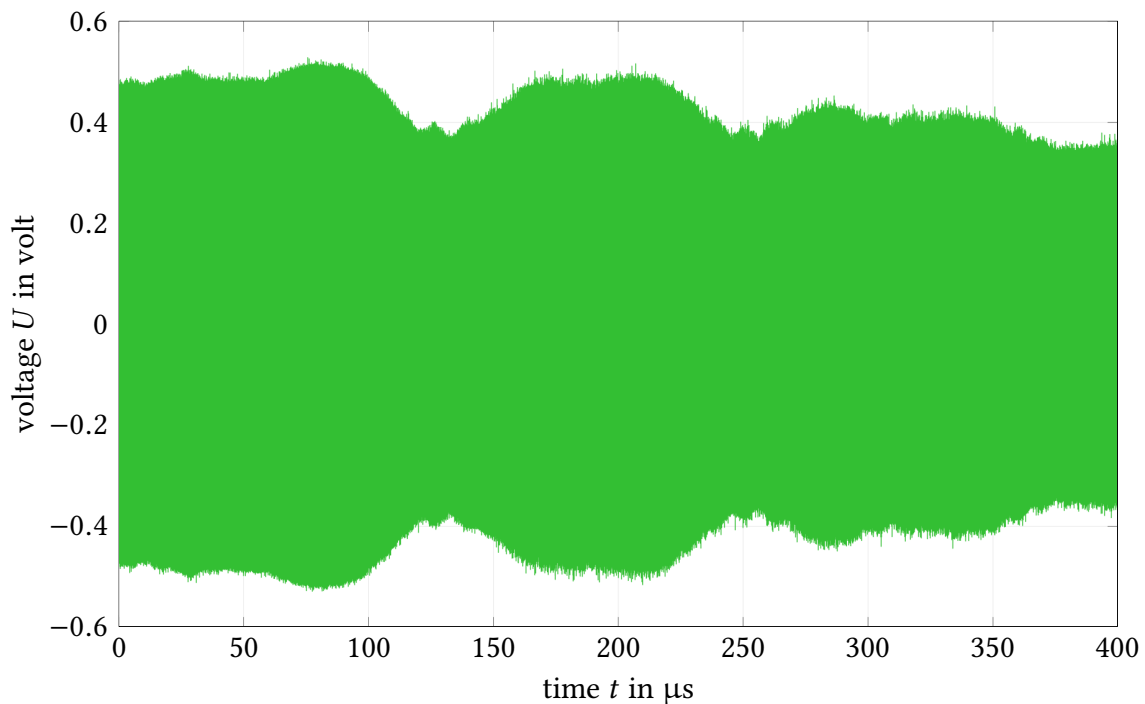


Fig. 3.10: Time-domain representation of TX chirp signal with an LFM sawtooth/ramp-modulation of 5.2 GHz bandwidth reaching from 0.8 GHz to 6 GHz and a sweep time of $T_s = 400 \mu\text{s}$ as recorded by a DSO.

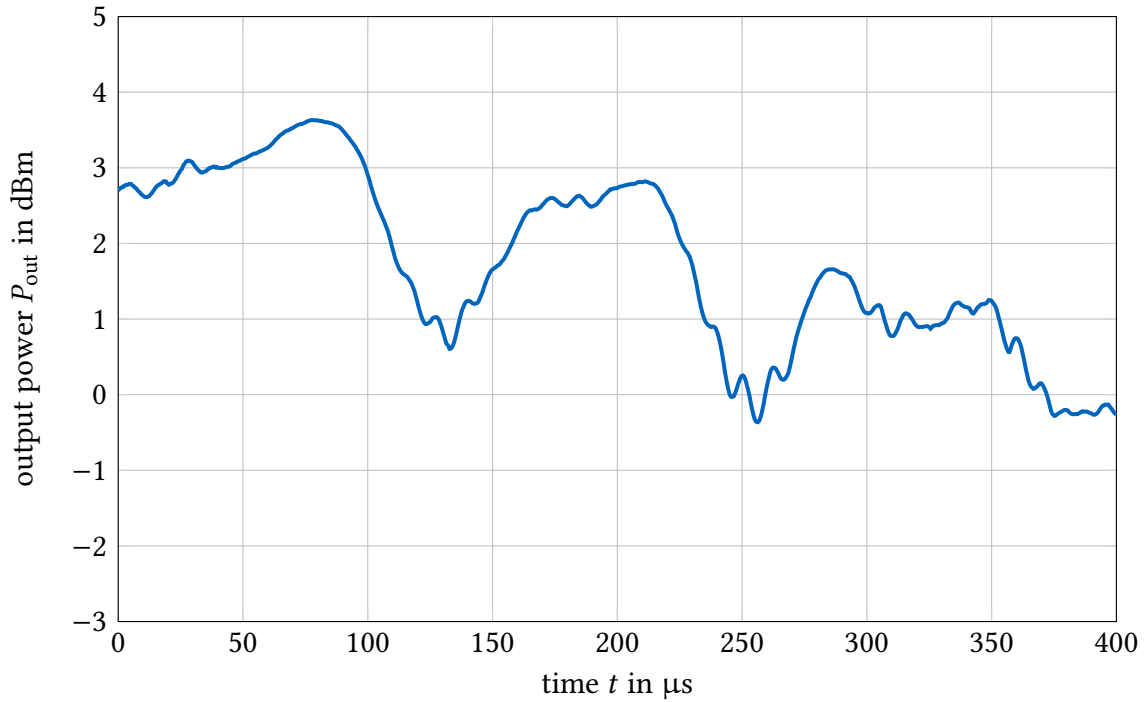


Fig. 3.11: Output power distribution of TX chirp signal over one modulation period with a sweep time of $T_s = 400 \mu\text{s}$ and a bandwidth of 5.2 GHz reaching from 0.8 GHz to 6 GHz.

signal as recorded by the DSO can be seen in Fig. 3.10, in a time-domain representation and in Fig. 3.11 converted into a power scale. Due to the limited memory of the DSO, the highest sampling rate of 40 GS/s is only accessible for signals up to a temporal length of 500 μs . A consistent decrease in voltage towards the end of this period is observed when inspecting the plot in Fig. 3.10. This decrease in voltage and hence power originates from the built-in DAC of the employed DDS. Due to the high frequency of the signal, the time dependence is hard to read out from Fig. 3.10; however, the visible envelope of the entire chirp is still insightful. DACs offer a non-flat but sinc roll-off frequency response, which attenuates signals at higher frequencies. Since the DDS is operated over a wide bandwidth and close to its own Nyquist limit, this non-flat trend must be taken into account.

The additional voltage variations within one period arise from the various components utilized in the frequency multiplier chain. Among these components are, for instance,

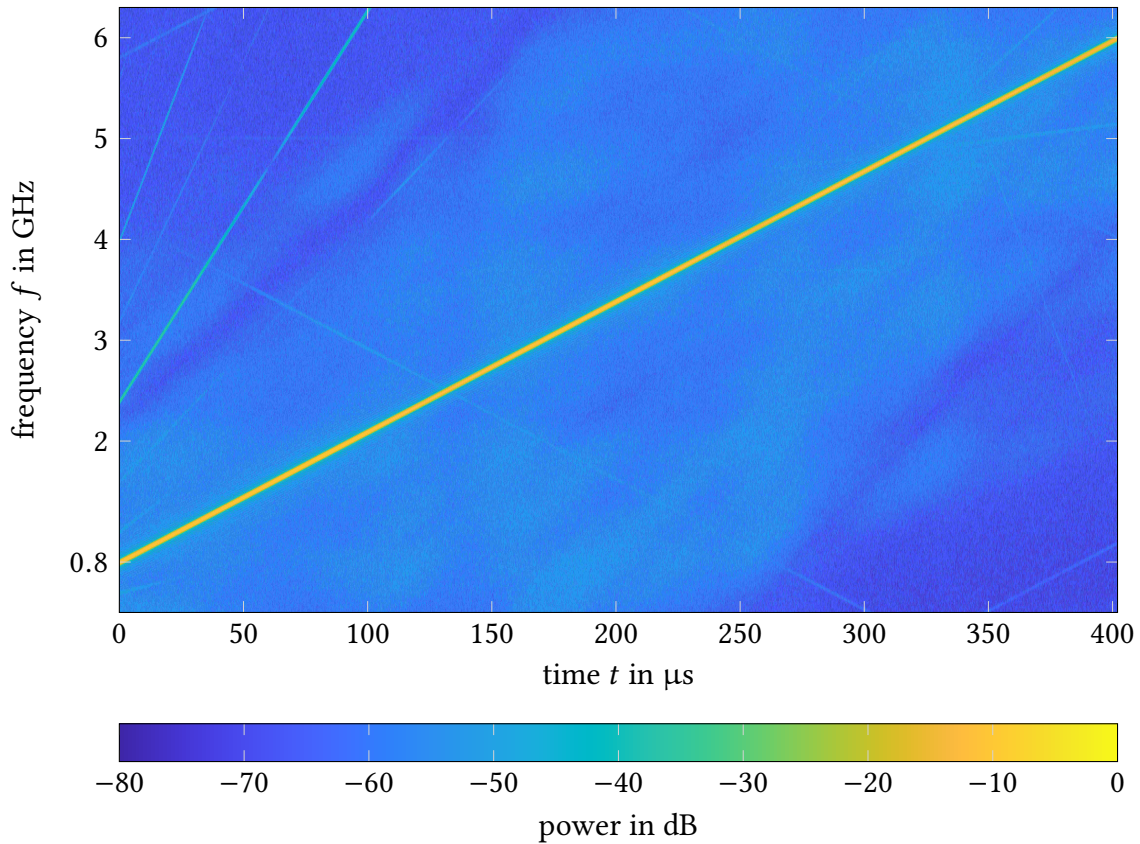


Fig. 3.12: Spectrogram representation of TX chirp signal with an LFM sawtooth/ramp-modulation of 5.2 GHz bandwidth reaching from 0.8 GHz to 6 GHz and a sweep time of $T_s = 400 \mu\text{s}$ [Möhrling et al. 2021], © 2021 IEEE.

amplifiers, filters, isolators, attenuators, or mixers, which can not offer a totally flat gain or attenuation curve over such large bandwidths of 5.2 GHz. However, a large bandwidth is of greater interest to the given airbag monitoring application and more valuable than a flat output power curve. The corresponding power distribution P_{out} in a dBm scale is computed by taking the envelope of the plot of Fig. 3.10 and smoothing the ripple-affected measurement data by taking a filter to ensure better readability. The power variation over the modulation period can be seen in Fig. 3.11, where values from 3.5 dBm down to about 0 dBm within one chirp are seen.

A spectrogram plot of the signal can be seen in Fig. 3.12. The spectrogram is computed

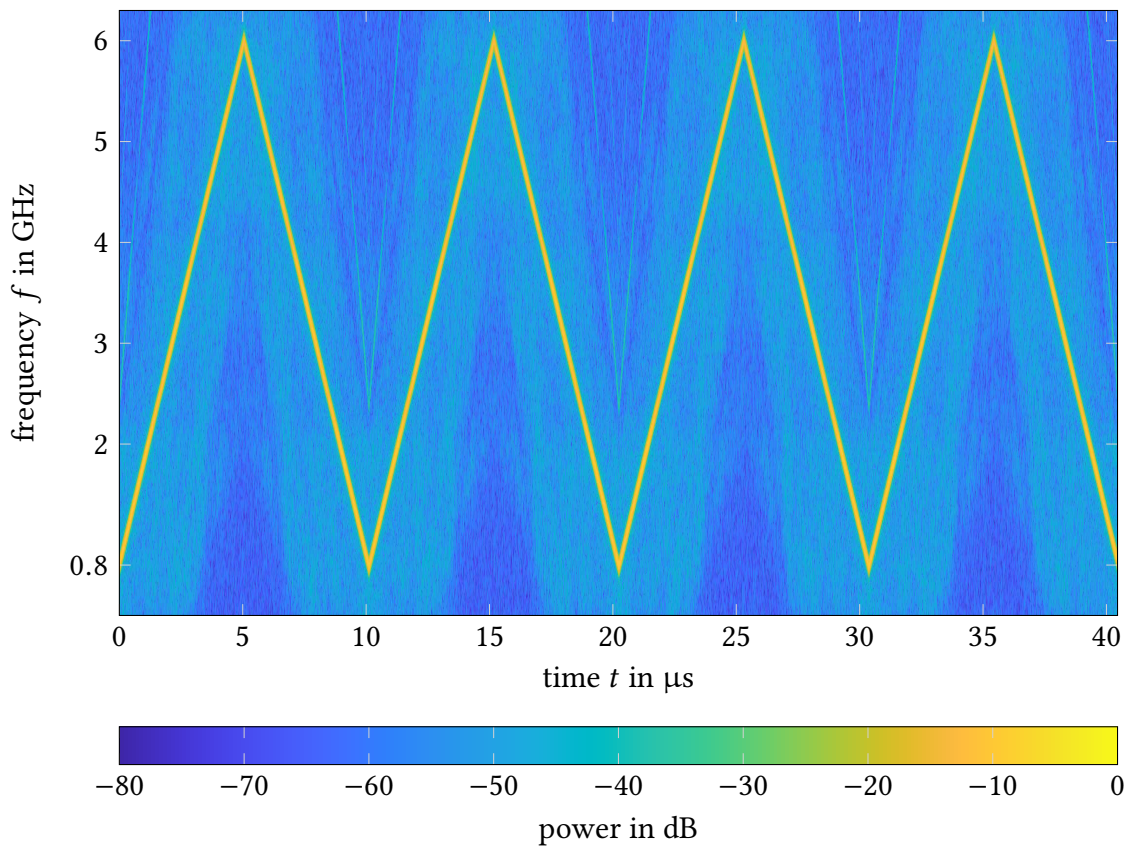


Fig. 3.13: Spectrogram representation of four TX chirp signals with an LFM triangular-modulation of 5.2 GHz bandwidth reaching from 0.8 GHz to 6 GHz and a sweep time of $T_s = 10 \mu\text{s}$ each [Möhrling et al. 2021], © 2021 IEEE.

with Matlab [The MathWorks, Inc. 2022] and represents the short-time Fourier transform of the signal. In this plot, the highly linear relationship of frequency and time of the chirp is apparent. No non-linear behavior as common with analog signal sources is visible. Moreover, the bandwidth of 5.2 GHz of the signal can be detected, reaching from 0.8 GHz to 6 GHz.

In addition to the intended signal, other spurious signals can be spotted arising from the DDS and the frequency multiplier chain, which impair the SFDR. For instance, in the top left corner of Fig. 3.12, four intermodulation products due to the up-conversion process with respective larger slopes can be seen. Also, a line with a negative slope is visible in

the spectrogram. This signal is the suppressed lower sideband also originating from the up-conversion process. Overall, the chirp signal offers an SFDR of more than 48 dB, and in some regions, it even offers an SFDR better than 55 dB.

Balon *et al.* [Balon et al. 2018] show similar spectrogram representations of a TX chirp signal with a bandwidth of 2 GHz, also employing an AD9914 [Analog Devices 2022a] as a signal source. There, an SFDR of at least -22 dBc is reported due to in-band spurious and LO leakage. The work of [Kim et al. 2022] also displays such spectrogram plots of a 6 GHz chirp in Ku-band offering an average SFDR of -45.5 dBc.

Four fast swept LFM TX chirp signals with a triangular-modulation scheme are shown in Fig. 3.13. This plot demonstrates the fast sweeping capabilities of the employed DDS-based signal generation, which facilitates the performance of fast chirp FMCW radar or reflectometry. For instance, a triangular-modulation scheme is beneficial when detecting and tracking moving targets. The overall resulting system specifications and performance features of the presented FMCW reflectometer are summarized in Table 3.1. There, the vital parameters of the FMCW can be found. Due to the DDS signal source, the modulation scheme and its sweep time T_s and herewith the number of chirps N can be adjusted to the given application.

The presented results of the TX chirp signal are well repeatable. A settling time is needed for the operation, during which a slight frequency shift of the LOs is noticeable since the

Table 3.1: FMCW reflectometer system characteristics [Möhring et al. 2022], ©2022 IEEE.

Parameter:	Specification:
modulation scheme	sawtooth/triangular FMCW
frequency range	800 MHz – 6 GHz
bandwidth B_{TX}	5.2 GHz
sweep time T_s	10 μ s to 1 s
number of chirps N	1 to 10^6
range resolution Δr	2 cm (TL with $\epsilon_r = 2$)
SFDR	min. 45 dB
beat frequency f_{beat}	DC to 50 MHz
max. range r_{max}	15 m
output power P_{out}	-5 dBm to -1 dBm

two PLLs and the Gunn oscillator employed as an LO are temperature sensitive. However, these frequency drifts cancel out due to the FMCW self-heterodyning architecture. In the design process, occurring temperature drifts were taken into account, and active fans are used to cool the delicate devices. The device is built for indoor operations assuming a temperature on the order of 20 °Celsius (68 °Fahrenheit).

3.5 Chapter Summary

A broadband, highly linear, and fast swept FMCW reflectometer in a portable housing for in-field measurements has been presented. The intended application of monitoring airbag deployment processes employing the TL-based FMCW reflectometry approach motivates the signal generation by DDS techniques due to its fast sweeping capabilities and other advantages like linearity, phase noise performance, or temperature stability. Several different bandwidth enhancement solutions are suggested, however, those were not further pursued due to a more promising performance of a designed analog frequency multiplier chain, which was then implemented and put into practice. This chain was developed with the aim of enlarging bandwidth and thereby range resolution while preserving SFDR and linearity of a DDS-generated signal. The frequency multiplier chain including all hardware components was described and explained. Measurements of the so generated TX chirp signal were presented to showcase its signal quality in terms of linearity, power, SFDR determining the device's associated measurement sensitivity and capability. Thereby, a highly linear LFM TX chirp signal, either in sawtooth or triangular modulation, of bandwidth 5.2 GHz spanning from 800 MHz to 6 GHz was realized with an SFDR of over 45 dB and sweep times in the microsecond range. The presented FMCW reflectometer is also adaptable for monostatic FMCW radar applications to monitor short-range static or fast varying targets.

Sensing Transmission Line

Possible transmission line (TL) types, designs, and manufacturing methods fitting to the airbag substrate for the given monitoring application are investigated and presented in the following. Numerical simulation results and measurement results employing a VNA are provided, comprising, for instance, a flexible stencil-printed coplanar waveguide (CPW) and a twisted-pair cable (TPC) with a dielectric core out of enameled wire.

4.1 Requirements for Sensing Transmission Line

As stated before and recalling the block diagram in Fig. 3.1, the TL shall function as a bend sensor and kink indicator by directly attaching it to the surface of an airbag, therefore, named sensing TL.

The TL shall indicate and sense surface deformations, which arise from the rapid inflation process of the airbag. The ideal sensing TL design must fulfill specific properties and demanding requirements, bearing the industrial monitoring application in mind.

First of all, it must be highly flexible, stretchable, and it must withstand strong forces which can occur during airbag deployment scenarios. In that respect, it should also be reversible to mechanical deformation, meaning that it can be bent, compressed, flexed, or strained multiple times without impairing or altering mechanical or electrical performance parameters permanently. This is rather challenging to achieve since commercially available and most common RF TL types are rather stiff and often offer limited flexibility only, since they are usually made out of metal. In general, well-conducting material is rather stiff and only offers a restricted flexibility. However, this flexibility property is the most important one since a too stiff or rigid TL would impair the unfolding behavior of the airbag too much.

Additionally, the characteristic impedance of a sensing TL must react sensitively to mechanical deformation, in particular to bending. Ideally and desirable would be a

deterministic relationship between the rate of bending/kinking and the rate of change of the local characteristic impedance. Such a relationship of mechanical and electrical parameters is needed in order to differentiate, for instance, a severe bend in the state of maximum folding and packing at the beginning of the deployment process from a slight or resolving bend or fold at the final stages of the deployment.

Besides, due to the explosive unfolding after igniting an airbag, strong occurring forces result in a quick rise in temperature, which must be withstood by the sensing TL. In this study, round airbags, as utilized in steering wheels to protect the driver, are considered, as sketched in Fig. 3.1, revealing a maximum diameter of about 65 cm in the fully unfolded state. Such driver airbags are folded and compressed up to 4 times to fit into its housing, also called module. A photograph of such a cut-up airbag module of a driver airbag from AUDI is depicted in Fig. 4.1. The module includes a multiply folded and compressed airbag, a gas generator providing the propellant, and control cables that trigger the ignition. The picture highlights the need for a highly flexible, compact, and yet enduring sensing TL.

The maximum diameter of the airbags of about 65 cm conditions the length dimensions of possible sensing TLs. A minimum extent accounts for the length of at least one diameter, whereas, in the case of attaching a sensing TL along two times the diameter, as depicted in Fig. 3.1, a maximum length of about 1 m to 1.5 m is needed.

Furthermore, a compact, dense, and low-profile TL geometry is favorable, which is simple to attach to airbag substrates and besides cost-effective in terms of material and manufacturing needs. Besides these declared mechanical requirements and constraints arising from the given application, a well-fitting sensing TL needs to fulfill additional electrical demands. As the sensing TL should be operated with the designed FMCW reflectometer presented in *Chapter 3*, it must also work well with little dispersion in the given frequency range of the reflectometer, spanning from 800 MHz to 6 GHz.

Additionally, the output port of the reflectometer and the corresponding feed-line provide an unbalanced TX signal via a coaxial SMA connector with a characteristic impedance of 50Ω . The sensing TL should have a characteristic impedance on the order of 50Ω , as well, in order to ensure a good matching performance to standard commercial RF equipment. Due to the large bandwidth reaching over almost three octaves, baluns are commercially unavailable and challenging to fabricate, so balanced sensing TL designs are unfavorable in terms of broadband matching.

Moreover, a shielded TL structure is preferred over an unshielded or open one. As seen in Fig. 4.1, the housing of an airbag at least partially consists of metal. Especially in the initial state, a multiply folded and compressed sensing TL can contact these metal parts and also get in contact with itself. Therefore, open and unshielded TL designs can suffer under the contact with metal or itself, resulting in a short-circuited state. Furthermore, open TL structures are more susceptible to radiation, cross-talk, and coupling effects and can suffer from the possible reception of spurious signals.

Due to the relatively short physical length of 1.5 m maximum, considerable transmission losses along the line are bearable. However, they should be kept to a minimum. The output power of the FMCW reflectometer of *Chapter 3* accounts for about $P_{\text{TX}} \approx -3 \text{ dBm}$.

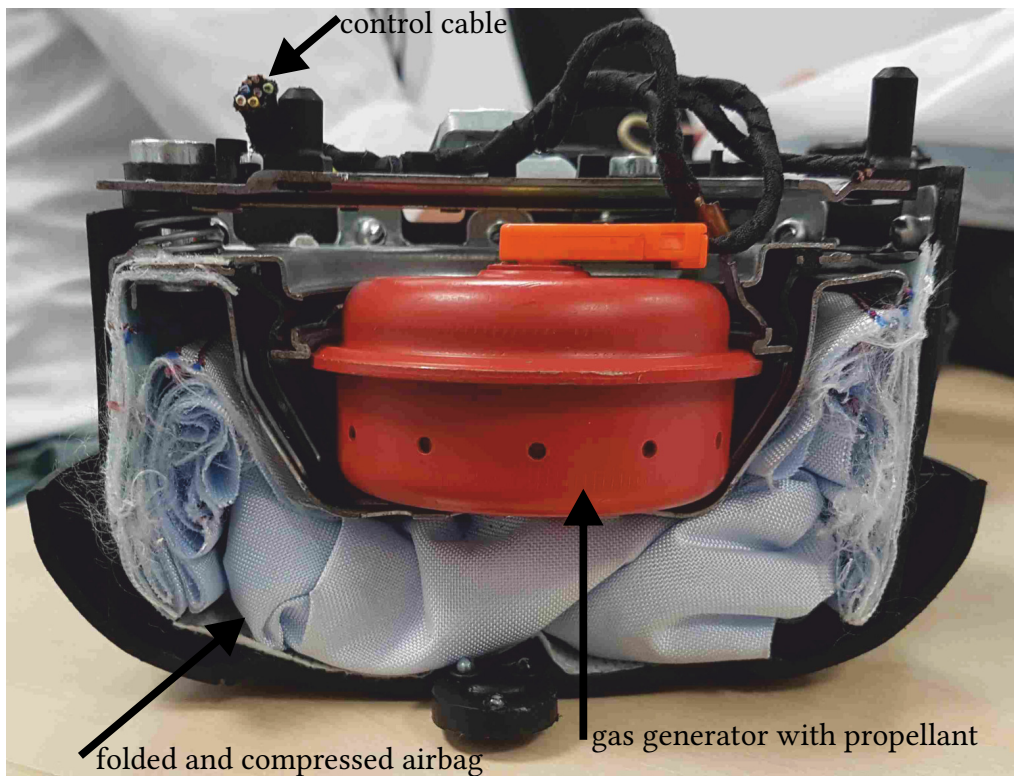


Fig. 4.1: Photograph of steering wheel airbag module in cross-section view, containing a multiply folded and compressed airbag fitted into its housing. Also, a red gas generator is seen and control cables.

Also, a relatively constant transmission behavior over the whole frequency range is aimed for in the frequency range of operation.

4.2 Airbag Textile Substrate

The textile fabric out of which most of the commercially available airbags are manufactured is a polyvinyl chloride (PVC) coated nylon/polyamide (PA) 66 fabric/yarn textile with a significant fabric pitch width on the order of 0.5 mm due to its woven structure. This blue-colored textile can be seen in Fig. 4.1.

The coating is performed to prevent the fabric from sticking together and for heat shielding reasons. Various airbag configurations in passenger vehicles are fabricated out of

this or similar materials in the automotive industry. This coarse and rugged fabric is primarily used for its excellent and enduring mechanical performance, which can withstand significant forces. Our project partners designed and manufactured the substrates used in this study, the Swedish-American automotive safety supplier Autoliv Inc. and the German company Global Safety Textiles GmbH. The thicknesses of the employed textiles vary and are on the order of 250 μm to 500 μm .

From an electrical point of view, such PA66 textiles reveal a real part of permittivity of about $\epsilon'_r \approx 3$ according to [Ku et al. 1999] at frequencies in C-band. Furthermore, the imaginary part ϵ''_r accounting for the losses and conditioning the loss tangent $\tan \delta$ is diverging, frequency-dependent, and also affected by the PVC coating. For instance, the authors of [Ku et al. 1999] report an imaginary part ϵ''_r for PA66 spanning from 0.02 up to 0.12 for frequencies from 7 GHz to 12 GHz, resulting in a loss tangent of 0.006 up to 0.04. In addition, the author of [Curtis 1961] reports on the dielectric properties of PA 66 for frequencies up to 10 MHz. Thereby, the real part ϵ'_r varies from 3.0 up to 3.2, while the imaginary part ϵ''_r ranges from 0.05 up to 0.07, which results in a loss tangent $\tan \delta$ of 0.015 up to 0.023.

4.3 Flexible Printed Coplanar Waveguide on Airbag

Recalling the demands for a possible sensing TL on an airbag dielectric substrate, planar TL technology comes to mind. Planar TLs comprise, for instance, the famous and widespread microstrip line, the slotline, the coplanar stripline (CPS), or the CPW [Gupta 1996; Simons 2001].

In this work, a CPW as a possible sensing TL is selected since it offers certain advantages over other planar TL implementations. The advantages of CPWs comprise, e.g., a simple fabrication, a dense and low-profile geometry, little radiation losses and dispersion, weak cross-talk, zero-cutoff frequency, which is beneficial for wideband operations, and most importantly, all conductors lie in the same plane upon the substrate (uniplanar). Especially, the last fact is desirable considering the given airbag application and the great variety of manufacturing processes [Gupta 1996; Simons 2001]. According to [Gupta 1996], CPWs reveal certain disadvantages as well, such as the existence of parasitic modes, lower power handling capabilities, and a non-confinement of fields.

A schematic illustration of a CPW attached directly to an airbag substrate is seen in Fig. 4.2. A CPW consists of a center conductor of width w_c and two adjacent semi-infinite ground conductor strips, each of width w_g . Thereby, the center conductor is separated by the two ground conductors by a slot of width s , while all three uniplanar strips reveal a thickness of t . The length of the CPW is denoted by l_{CPW} . The dielectric substrate of material PA 66 of the airbag is characterized by its complex permittivity $\epsilon'_r - j\epsilon''_r$ and its height h [Simons 2001].

Typical CPWs are unbalanced TLs that allow a quasi-TEM mode to propagate. This mode is referred to as quasi-TEM mode due to the existence of a longitudinal component of the magnetic field [Gupta 1996; Simons 2001]. Thereby, a part of the mode is propagating

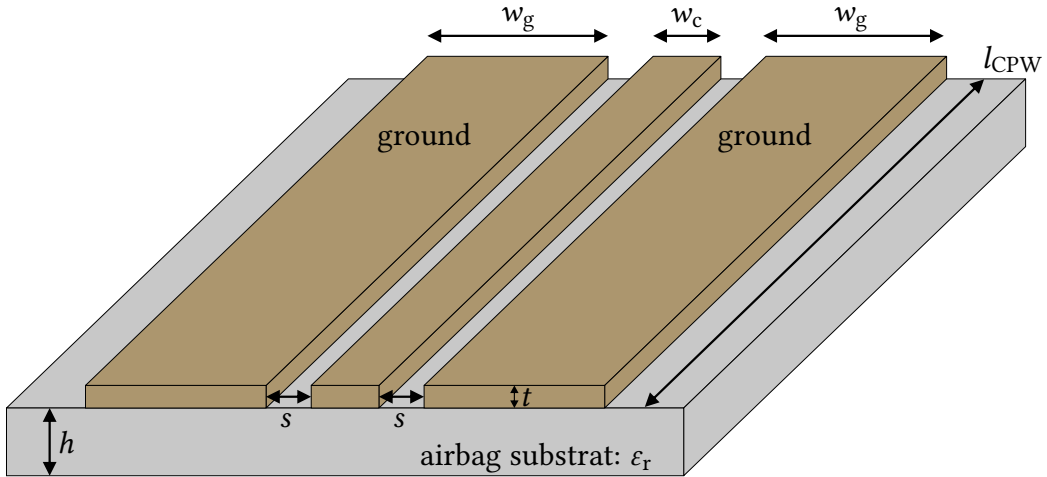


Fig. 4.2: Cross-section view of a schematic illustration of coplanar waveguide structure attached on airbag substrate with according dimensions [Gupta 1996; Simons 2001].

through the dielectric, whereas the remaining portion is propagating through air. Instead of the permittivity of the airbag substrate, an effective permittivity ϵ_{eff} needs to be taken into account, which considers both dielectrics, substrate, and air.

However, the strongest fields and hence most of the energy of the signal is predominantly restricted to the small gap of width s , seen in Fig. 4.2.

Analytic formulas for calculating the characteristic impedance Z_{CPW} of CPWs and the, therefore, needed effective permittivity ϵ_{eff} based on conformal mapping under the assumption of a quasi-static TEM mode are found, for instance, in [Bedair and Wolff 1992], [Simons 2001], or [Gupta 1996].

These formulas assume an ideal geometry with no surface roughness. They are excluded here for reasons of brevity. The characteristic impedance of CPWs is influenced by many parameters, mainly by its geometry, in the form of the conductor strip width w_c , the ground width w_g , the gap width s , the conductor thickness t , but also by the complex permittivity of the substrate $\epsilon'_r - j\epsilon''_r$ and its height h .

Additional reasons support the usage of a CPW design for the given airbag application. CPWs are simple and well-suitably to interconnect with SMA connectors, since both

offer a center conductor with a surrounding outer ground conductor and both carry unbalanced signals. Although CPWs are open structures and are not shielded, most of the energy of the signal is concentrated into a confined space in the two gaps between the center conductor and the respective two ground conductors. Since the airbag PA 66 substrate is a textile and highly flexible and stretchable, the attached CPW structure must also be made out of flexible yet well-conducting material, for instance, a conductive ink directly printed on the airbag or a very thin and hence flexible metal. The generic term and research field, which includes various printing methods, flexible substrates, and conductive inks to create and design electric and electronic devices, is named printed electronics [Suganuma 2014]. In the next subsection, an overview and introduction to the field of printed electronics are provided focusing on RF applications and printed RF TL realizations.

4.3.1 Overview of Printed Electronics

Printed electronics is an emerging topic and enables effective and facile manufacturing solutions for various applications comprising wearable sensors, for instance, for communication, medical monitoring, or security purposes. Printing on flexible substrates to produce wearable and tensile electronic devices allows lightweight, rapid, low-cost, and environmentally friendly manufacturing. This manufacturing technique is often accompanied by little material waste and also by better thermal and mechanical properties compared to conventional techniques, which require cleanroom environments [Cook et al. 2013; Haghzadeh et al. 2017; Nag et al. 2017; Suganuma 2014].

The benefits and capabilities of printing flexible electronics have also been exploited in the field of RF applications and devices, such as antennas [Yang et al. 2007], TLs [Belhaj et al. 2014; Kim et al. 2015; Locher and Tröster 2007; Sahu et al. 2017; Xu and Hamilton 2013; Xu et al. 2014], RF identification (RFID) tags [Yang et al. 2007], or other components such as varactors, phase shifters [Haghzadeh et al. 2017], capacitors [Cook et al. 2013], or inductors [Menicanin et al. 2013].

However, successfully printing such RF devices is a challenging task mainly due to the often times limited conductivity of flexible conducting material and also due to the lossy and sometimes unknown dielectric properties regarding higher frequencies of flexible substrates. Furthermore, strict geometrical requirements concerning the manufacturing accuracy and resulting surface roughness together with mechanical and thermal constraints pose a challenge, especially at RF frequencies.

For RF applications, the most common and famous printing techniques are inkjet [Belhaj et al. 2014; Haghzadeh et al. 2017; Kim et al. 2015; Sahu et al. 2017; Xu and Hamilton 2013] and screen printing [Amoli et al. 2019; Locher and Tröster 2007]. Preferably used substrates are flexible, clean, and smooth surface polyimides such as Kapton, or also polyethylene naphthalate (PEN) and polyethylene terephthalate (PET) substrates are frequently employed [Amoli et al. 2019; Haghzadeh et al. 2017; Nag et al. 2017; Sahu et al. 2017; Xu and Hamilton 2013]. Inexpensive, flexible, and wearable TLs are needed, for

instance, to feed flexible body-worn antennas for RFID or other communication purposes [Xu and Hamilton 2013; Xu et al. 2014]. Thereby, robustness against bending is essential for wearable electronics. In [Locher and Tröster 2007], an acryl-cotton woven fabric is used as a substrate for screen printing of a CPW, while in [Kim et al. 2015; Shao et al. 2008] rigid CPWs are ink-jet printed on glass. In the literature, printed CPWs for RF signals are reported, for instance, in [Kim et al. 2015; Locher and Tröster 2007; Sahu et al. 2017; Xu and Hamilton 2013; Xu et al. 2014].

The design process, especially the conductive ink composition, is commonly a trade-off between electrical performance and mechanical flexibility [Matsuhisa et al. 2017]. High mechanical flexibility, elasticity, mechanical durability, good adhesion, and robustness are often accompanied by poor conductivity and hence high losses and modest electrical performance.

It remains challenging to successfully print highly flexible, elastic, and yet electrically efficient TLs for RF signals, especially on rough textile substrates, in an economical printing process.

4.3.2 CPW Design and Stencil Printing Process

In this work, the printing method known as stencil printing is utilized to directly print a CPW consisting of a conductive ink on the airbag PA 66 substrate.

Stencil printing dates back to the 1960s and is related to the more popular and traditional screen printing. Instead of employing a woven mesh screen, a stencil is used, which is a solid foil, through which the printing material is attached to the substrate by using a squeegee. Stencil printing is a versatile and cost-effective method for solder paste deposition on various substrates and allows high volume assembly of possibly large structures and can handle more delicate dimensions with respect to screen printing [Kay and Desmulliez 2012; Pan et al. 2004].

The conductive ink (elastomer) or elastic conductor used in this work was synthesized according to instructions in [Matsuhisa et al. 2017]. Briefly described, silver (Ag) nanoparticle flakes with a particle size of 10 μm by Sigma Aldrich, St. Louis, USA, pre-cut fluorine rubber of type DAI-EL G-8002 by Daikin Chemical Europe GmbH, Düsseldorf, Germany, a 4-methyl-2-pentanone solvent by Sigma Aldrich, St. Louis, USA, and a fluorinated surfactant of type Zonyl FS-300 by abcr GmbH, Karlsruhe, Germany were added to a closed vessel at a ratio of 3:1:2:1 (w:w:w:w) and stirred for longer than 12 hours.

To structure the obtained elastomer on the airbag textile into a CPW arrangement, a stencil mask was cut into a PEN foil of type Q65HA by DuPont Teijin Films, Tokyo, Japan, with a thickness of 125 μm , employing a desktop cutting plotter of type Cameo 3 by Silhouette America, Lindon, USA.

Next, the PA 66 textile and the PEN mask were magnetically fixed onto a metal surface. In this process, the conductive elastomer was added and squeegeed through the mask utilizing a glass slide.

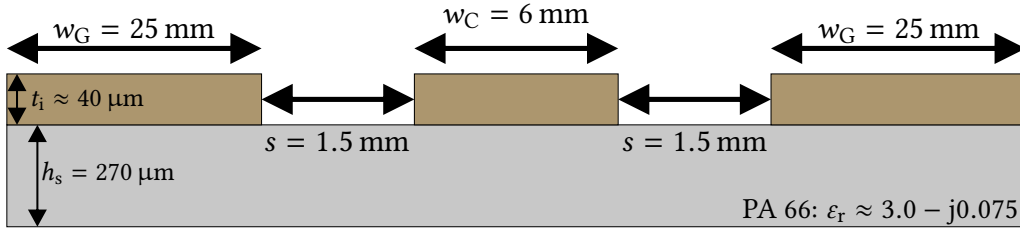


Fig. 4.3: Dimensions of stencil-printed CPW prototype on airbag PA 66 substrate in cross-sectional view assuming an ideal geometry within accuracy limits of the manual printing process.

Finally, after carefully removing the mask, the samples were cured at 80°C for 3 hours. Additional sintering is unnecessary. Moreover, the proposed ink of [Matsuhisa et al. 2017] could potentially also be used in screen and dispenser printing processes. The surface profile and the geometry of this so printed CPW structure are affected mainly by the printing process and the viscosity of the ink, surface roughness, surface energy, temperature of the substrate, and sintering temperature and duration [Kim et al. 2015; Pan et al. 2004].

The CPW was structured on the PA 66 airbag substrate with a thickness of $h_s = 0.27 \text{ mm}$ in this single-step and straightforward stencil printing process. The ink was chosen for this application primarily due to its good flexibility, stretchability, and mechanical durability. Thereby, this elastic ink still offers a maximum conductivity of about $\kappa_{i,\text{max}} = 6.168 \cdot 10^5 \text{ S/m}$ and a conductivity when stretched 400% of $\kappa_{i,\text{str}} = 9.35 \cdot 10^4 \text{ S/m}$ according to [Matsuhisa et al. 2017], together with high elasticity, robustness, good adhesion, and not peeling off or breaking when flexed.

In the design process of the CPW, a characteristic impedance in the range of 50Ω was aimed for, since most common commercial RF components and coaxial TLs reveal this impedance. However, due to the accuracy limitations in the manual stencil printing process and the large surface roughness of the PA 66 substrate, a gap-width of less than $s = 1.5 \text{ mm}$ was not feasible primarily due to the capillary motion of the ink and resulting short circuits, despite several attempts. However, a very small gap width of below 1 mm is crucial for establishing such small characteristic impedances on the order of 50Ω when using such thin dielectric substrates and under the condition of a relatively small center strip width w_c [Bedair and Wolff 1992; Simons 2001].

The total width of the center strip plus the two gaps of $(w_c + 2s)$ was chosen to meet the dimensions of a commercially available edge-launch SMA PCB mounting connector. These particular connectors are used to connect CPWs on PCBs to SMA connectors. In that respect, these edge-launch SMA PCB connectors offer a center pin and four surrounding ground pins revealing a total width of 9.5 mm.

The objective to match the dimensions of such edge-launch SMA PCB connectors was of higher priority than designing a CPW with a characteristic impedance of 50Ω . Furthermore, besides impedance matching, mode conversion issues need to be taken into account, as well. In this process, a relatively smooth mode transition from a coaxial TEM mode of the SMA connector to a quasi-TEM coplanar mode must be ascertained without a considerable change in geometry, not to cause significant field jumps/gaps [Drak and Liubina 2021; Gupta 1996].

A CPW prototype was designed, following the dimensions seen in Fig. 4.3. The center strip offers a width of $w_c = 6$ mm, while the two ground pads are of width $w_g = 25$ mm. Together with the gap-width of $s = 1.5$ mm and the permittivity of the PA 66 substrate of about $\epsilon_r \approx 3.0 - j0.075$, an ideal analytically calculated characteristic impedance of the CPW of about $Z_{CPW,a} = 92 \Omega$ was achieved. Lower values were aimed for but not realizable.

Thereby, it needs to be taken into account that the analytic formulas of [Simons 2001] and [Bedair and Wolff 1992] neglect the finite conductivity of the ink. They also ignore the surface roughness of both the PA 66 substrate and the eroded surface roughness and not perfect geometry of the attached ink since the dispersion of the printed ink is highly influenced by the surface roughness of the substrate. Instead, an ideal smooth and exact geometry is assumed.

In the design process, preserving the mechanical flexibility of the textile was of high priority due to the given application. Consequently, the thickness of the ink t_i was aimed to be as thin as possible, and the CPW was directly printed upon the airbag substrate without an additional dielectric.

Optical images of the CPW prototype were taken to further characterize and investigate the results of the stencil printing process in terms of accuracy, surface roughness, and fidelity. Together with according surface profiles of the CPW samples, the images were recorded using a confocal laser profilometer of type VK-X250 by Keyence, Osaka, Japan, equipped with an $10\times$ objective of type CF Plan Apo by Nikon, Minato, Japan. Pictures of both the left and the right gap were used to measure the actual gap width. The images can be seen in Fig. 4.4 and Fig. 4.5.

For all profilometric analyses, a first-order polynomial in x and y was fitted to the data showing only the PA 66 textile. Subsequently, this fit was then subtracted from the complete data set to remove the offset of the sample and the tilt. Furthermore, high-frequency noise was removed from the data by employing a 2D median filter of kernel size $50 \times 50 \text{ px}^2$, which is equivalent to $0.14 \times 0.14 \text{ mm}^2$. A picture of the periphery of the conductive structure was used to determine the root mean square (RMS) surface roughness (Rq) of both, the PA 66 textile and the conductor, respectively. The approximate layer thickness was determined by subtracting the average height level of the whole

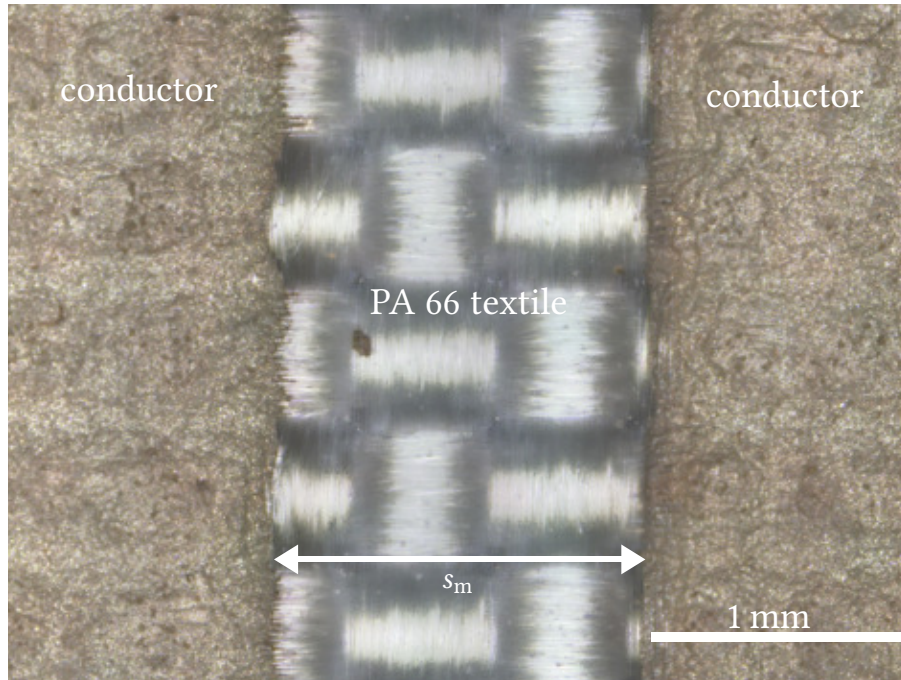


Fig. 4.4: Microscope image of the gap between two conducting strips together with a scale bar of 1 mm. A good edge fidelity and a homogeneous conducting surface can be seen, together with the woven and rough/rugged structure of the PA 66 substrate.

textile from the regions on which the conductive ink is printed. Examining the picture in Fig. 4.4, which shows an optical image of the gap of width s_m in between the conductive structures, a good edge fidelity and homogeneous coating of the conductive elastomer is noticeable. Such images of the two gaps on both sides were used to measure the actual width of these gaps, which accounts for about $s_m = 1.47$ mm.

In addition, Fig. 4.5 shows a profilometric image of the region shown in Fig. 4.4. A clear height difference between the coated and non-coated areas and the textile structure is visible. Especially the rough and wavy surface profile of both the ink and the textile is visible. The analysis of the profilometric data revealed an approximate layer thickness of $t_{i,m} = 38.5$ μm . Furthermore, the RMS surface roughnesses of the textile and of the conductor were found as $Rq_{s,m} = 41.2$ μm and $Rq_{i,m} = 18.2$ μm , respectively. Such non-planar and uneven surfaces are adverse for RF applications since RF currents flow predominantly near the surface due to the skin effect [Kim et al. 2015].

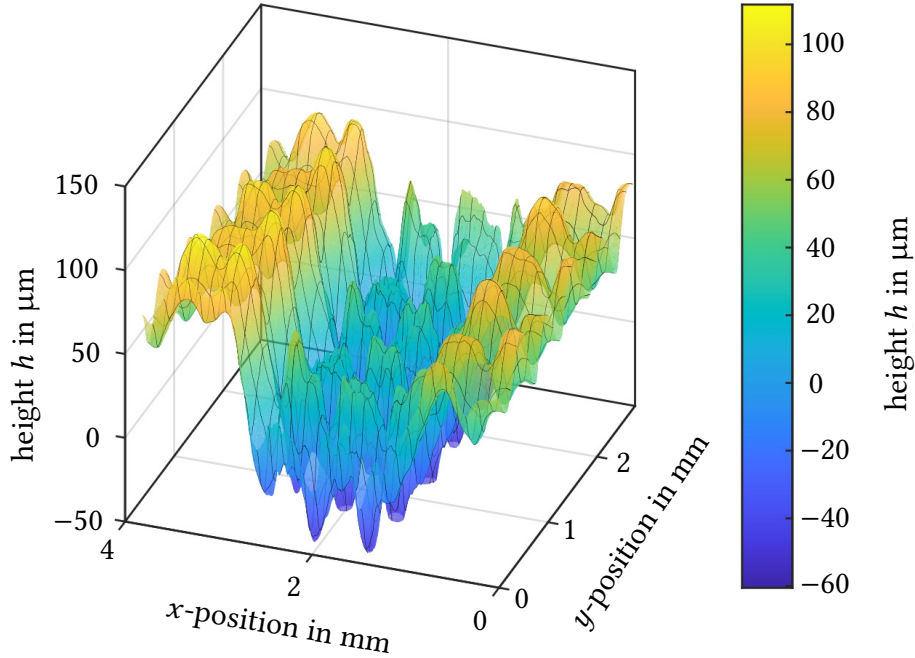


Fig. 4.5: 3D profilometric image of the gap between the two conducting strips as shown in Fig. 4.4. The surface roughness of both the ink and the substrate is apparent together with a clear height difference between the coated and non-coated areas. A somewhat trapezoidal cross-section is seen instead of an ideal rectangularly shaped one.

A realistically achievable and consistent conductivity of the ink on the order of about $\kappa_{i,\text{real}} \sim 10^5 \text{ S/m}$ at a frequency of 6 GHz results in a skin depth of about $20 \mu\text{m}$ according to (2.33), which is on the order of the RMS surface roughness of the ink [Pozar 2012]. The profilometric measurement data was processed and plotted with the software tool Matlab [The MathWorks, Inc. 2022].

The CPW prototype with the geometry shown in Fig. 4.3 offers a total mechanical length of $l_{\text{CPW}} = 129 \text{ mm}$. The transition from the three conductive strips of the unbalanced CPW to a coaxial TL is realized by gluing standard 50Ω SMA female PCB-connectors to both ends. Due to the small heat resistance of the conductive ink and textile substrate, soldering can not be employed as a jointing technology. Instead, gluing with conductive glue is used here to establish the connection of the three strips and the SMA connector. The connectors must be tapered in advance in order to meet the broader dimensions of

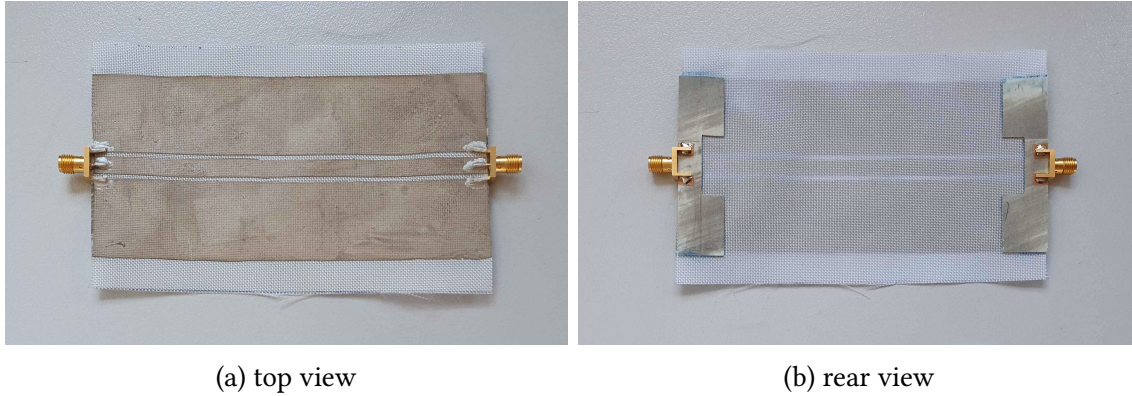


Fig. 4.6: Pictures of stencil-printed CPW prototype on airbag PA 66 substrate showing the auxiliary Rogers substrates for mounting and mechanically fixing the SMA connectors and mechanically relieving the conductive glue.

the $Z_{CPW,a} = 92 \Omega$ CPW. An electrically conducting polyurethane adhesive, Polytec PU 1000, is used for this. This silver-based adhesive offers a specific electrical resistance of about $\rho_g = 4 \cdot 10^{-4} \Omega\text{cm}$, which corresponds to a conductivity of $\kappa_g = 0.25 \cdot 10^6 \text{ S/m}$, yet offering good mechanical stability and robustness. To enhance the mechanical stability and strength, a supplemental Rogers substrate (RO4350B) is glued to the back of the substrate to solder the rear side for mechanically fixing the SMA connectors. A picture of the CPW prototype in top-view can be seen in Fig. 4.6(a) and the corresponding rear view is depicted in Fig. 4.6(b).

Together with the attached SMA connectors, the CPW has a length close to 150 mm. This backside view of the substrate with the two auxiliary Rogers laminates is depicted in Fig. 4.6(b). There, the transparency of the material is seen due to its small thickness. The Rogers substrates reveal a length of 60 mm, a width of 15 mm, and a thickness of 1 mm. Except for two solder pads for the connectors, all conductive material was lasered from the substrate to improve the impedance matching and impair the transmission behavior as little as possible. Since a locally thicker substrate reduces the characteristic impedance of the CPW and ensures a better impedance matching, because the thicker the substrate, the smaller the characteristic impedance of the CPW according to [Simons 2001].

The application demands more mechanical stability and tensile strength that a simple connection by conductive glue is not durable. Commonly, conductive glue is associated with limited mechanical adhesive power. To demonstrate the flexibility, elasticity, and



Fig. 4.7: Pictures of multiple folded stencil-printed CPW prototype on airbag PA 66 substrate in side and top view to demonstrate its flexibility, bending resistance, and mechanical endurance.

cyclic durability of the printed CPW, Fig. 4.7(a) and Fig. 4.7(b) show pictures in which the CPW prototype is bent multiple times. The two black universal clamps are just for the mechanical fixing of the prototype. The observed bending capabilities are very promising compared to the previous work of [Amoli et al. 2019] or [Xu and Hamilton 2013].

4.3.3 Numerical Simulation Model in CST

The commercially available EM analysis tool Computer Simulation Technology Microwave Studio (CST) [Dassault Systèmes 2022] was utilized to provide reference data for the printed CPW prototype. A picture of the created simulation model in CST is depicted in Fig. 4.8. The physical dimensions match those of the printed CPW prototype of Fig. 4.3. However, unlike the actual CPW, the CPW model in CST is excited by two waveguide ports on both ends instead of a coaxial SMA connector. The PA 66 substrate has a permittivity of about $\epsilon'_r \approx 3.0$ and a loss tangent of $\tan \delta = 0.025$. The dielectric properties of PA 66 are reported in [Curtis 1961; Ku et al. 1999] and are set to $\epsilon_r = 3.0 - j0.075$ in accordance with the data provided by the manufacturer. However, those values can deviate over such a wide frequency range due to the coating and the woven structure, especially at higher frequencies.

In the simulation model, the conductivity of the ink is set to $\kappa_{i,\text{real}} \approx 1 \cdot 10^5$ S/m based on an initial sheet resistance measurement of the conductive strips and averaging those values. The material parameters of the conductive ink, its surface roughness, and the PA 66 substrate are adjusted to the measured values of the prototype, as described in the previous subsection. Thereby, the RMS surface roughness of the ink is set to $Rq_{i,m} = 18 \mu\text{m}$, while the roughness of the PA 66 substrate is set to $Rq_{s,m} = 41 \mu\text{m}$.

The simulated scattering parameters of the model are presented in the following section, together with the measurement results. Due to the symmetry, passiveness, and equal waveguide ports, the parameters S_{21} and S_{12} match, and S_{11} equals S_{22} in the simulation. In CST, the wave impedance of the CPW was calculated as $Z_{\text{CPW},s} = 90.7 \Omega$, which differs from the analytic result since CST takes the low conductivity and high surface roughness of the materials into account. The simulated port matching $S_{11,s} = S_{22,s}$ together with the simulated transmission $S_{21,s}$ of this model are shown Fig. 4.9.

4.3.4 VNA Measurement Setup and Results

Measurements were performed with a VNA of model ZVA 24 by Rohde & Schwarz together with a prior calibration procedure employing the calibration unit ZV-Z52 by Rohde & Schwarz to shift the reference plane to the SMA connectors of the CPW [Hiebel 2016]. The measured scattering parameters (subscript m) spanning from 10 MHz to 8 GHz are shown in Fig. 4.9, together with the simulation results (subscript s) from the CST model of the previous subsection for comparison purposes.

In order to make the simulation model in CST, which is excited by waveguide ports, comparable to the actual CPW fed by coaxial SMA connectors, both S -parameters, the measured and the simulated ones, are renormalized to the same reference impedance employing Matlab [The MathWorks, Inc. 2022]. In this way, the simulated port matching values are comparable to the results from the measurement setup. This is also done to consider the impact of the poor matching values due to the impedance jump on the

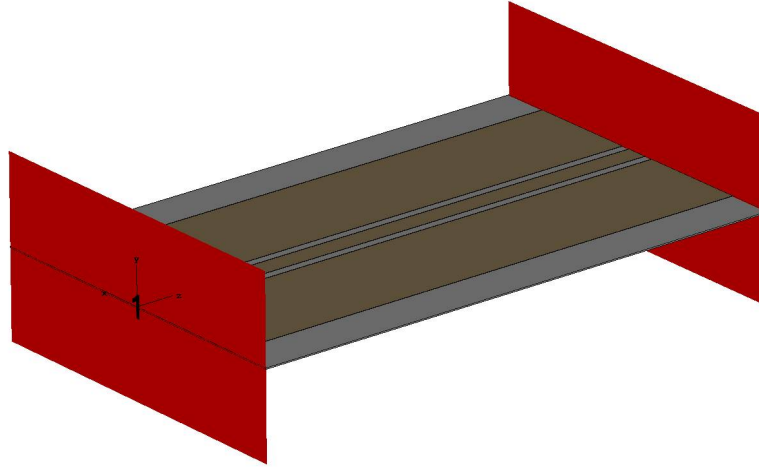


Fig. 4.8: Simulation model in CST of a stencil-printed CPW on PA 66 substrate excited by waveguide ports.

transmission properties of the CPW. This renormalizing is also performed to alleviate the significant mismatch of the measurement results arising from the impedance jump of connecting a standard $50\ \Omega$ coaxial SMA connector to a $92\ \Omega$ planar CPW as well as the mode transition from a coaxial TEM mode to a quasi-TEM CPW mode

When inspecting the plot in Fig. 4.9, the measured port matching on both ends, $S_{11,m}$ and $S_{22,m}$, reveal a high symmetry, especially taking the modest and basic manufacturing process, the curved up/tapered connectors, and the connection by conductive glue into account. Also, slight differences are noticeable when inspecting $S_{11,m}$ and $S_{22,m}$, which reveal sensitivity to the port matching values due to the gluing process of the SMA connectors. However, the overall port matching offers relatively modest values, primarily due to the impedance mismatch of connecting a standard $50\ \Omega$ SMA connector to a CPW with a characteristic impedance of about $Z_{CPW,a} = 92\ \Omega$ together with the corresponding mode transition from a coaxial TEM mode to a quasi-TEM planar CPW mode.

The simulated port matching values $S_{11,s} = S_{22,s}$ show a good agreement with the measured port matching, especially at low frequencies. However, since the employed materials suffer from dispersion and are affected by losses, the measured parameters deviate from the simulated ones when exceeding about 4 GHz, and the congruence decreases when inspecting the plot in Fig. 4.9. Yet the order of mismatch remains the same. The dispersion behavior in the simulation deviates from the actual dispersion behavior. Furthermore, the actual matching is impaired by the considerable surface roughness of both the ink

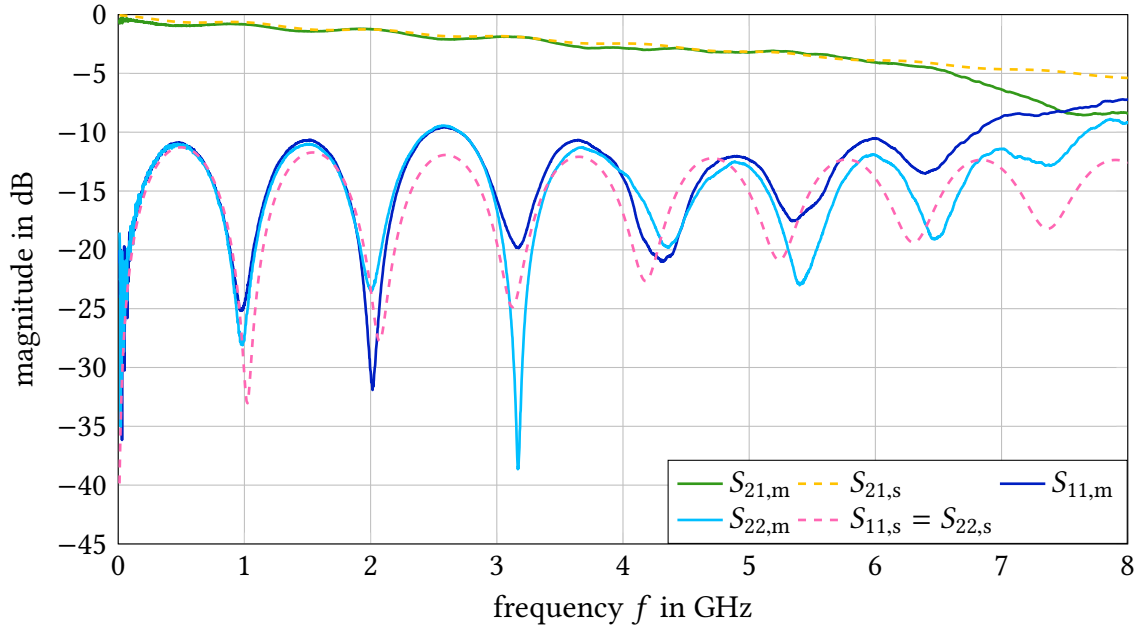


Fig. 4.9: Comparison of measured (subscript m) and simulated (subscript s) port matching and transmission scattering parameters of printed CPW prototype.

and the nylon 66 substrate, together with the limited conductivity of the ink. When comparing the measured port matching $S_{11,m}$ and $S_{22,m}$ to the simulated port matching $S_{11,s} = S_{22,s}$, the same and typical behavior for TLs of multiple resonances at a distance of about 1 GHz due to multiple reflections is seen.

The measured transmission performance $S_{12,m} = S_{21,m}$ offers reasonable and predictable values throughout the frequency range. Due to the limited conductivity of the used ink of about $\kappa_{i,\text{real}} \approx 1 \cdot 10^5 \text{ S/m}$, losses linearly increase with frequency primarily due to the skin effect, which induces an increase of the characteristic impedance. In addition, at higher frequencies, the skin depth is on the order of the ink's surface roughness, which induces further attenuation [Amoli et al. 2019].

The measured transmission $S_{21,m}$ matches the simulated transmission $S_{21,s}$ remarkably well over a wide frequency range reaching from 10 MHz to about 6.9 GHz. Both curves reveal minor dips that arise from the poor port matching at about 500 MHz, 1.65 GHz, 2.8 GHz, and about 3.9 GHz in terms of the measurement. Since the simulated port matching results deviate from the measured results with increasing frequency, the dips in the transmission at higher frequencies are also slightly shifted along the frequency

axis. Overall, the simulated transmission $S_{21,s}$ reveals a linear and plausible decrease over frequency.

The effective permittivity $\epsilon_{r,\text{eff}}$ decreases with increasing frequency, as typical for CPWs and as seen in Fig. 4.9 when inspecting the location of the resonances for both measurement and simulation results. Ripples at a distance of about 1 GHz correspond to multiple reflections between the two connectors with a CPW length of $\lambda_{\text{eff}}/2 \approx l_{\text{CPW}} \approx 150$ mm. Altogether, even at a relatively high frequency of 6 GHz, still, an insertion loss of less than 4 dB along the CPW with the SMA connectors of length $l_{\text{CPW,SMA}} = 150$ mm is attained. This performance is remarkable considering the rough and lossy substrate, the limited conductivity of the ink, the defective geometry, and also the rough surface of the TL due to the manual printing process, and the significant mismatch due to not impedance matched and provisionally glued on and curved-up(tapered) SMA connectors.

A rough cost estimate of the CPW, including conductive ink, SMA connectors, conductive glue, and PA 66 substrate, does not exceed 100 Euro per meter. Albeit, even superior values should be achievable by improving the port matching, the manufacturing process, and the conductivity of the ink. At higher frequencies above 7 GHz, the impact of the limited conductivity of the ink and the conductive glue comes into effect. Also, the frequency limits of the SMA connector severely worsen the matching performance and, by that, also impair the transmission behavior as seen on the top right of Fig. 4.9.

Overall, the simulation and measurement results match relatively well, and all observed differences of both are well explainable. As mentioned in the previous subsection, the CPW prototype offers a non-ideal geometry in terms of cross-section (trapezoidal instead of rectangular) along the three traces. Still, the measured electrical performance seems robust against deviations from ideal geometry.

4.4 Twisted-Pair Cable out of Enameled Wire

In the search for a well-fitting sensing TL for the intended airbag application, further investigations were performed in the field of flexible twisted-pair cables (TPC), which were initially invented for telephone communications [Chamberlin et al. 1995].

This research was motivated by the promising features of this TL type, such as high mechanical flexibility, reduced coupling and, therefore, cross-talk due to twisting, as well as cheap and straightforward manufacturing [Lago et al. 2009; Paul and McKnight 1979]. Most importantly, the TPC design was chosen here due to its reduced phase velocity resulting from the twisting and thereby increased conductor length. Although TPCs are usually used and specified for lower frequencies of several hundreds of MHz, they can also be used up to GHz frequencies [Chamberlin et al. 1995; Siebert 2003].

Furthermore, their compact two-wire and non-uniform arrangement appears to be electrically sensitive to mechanical bends. In case of deformations, the wire spacing alters, resulting in a locally changed characteristic impedance, a desirable property for reflectometry purposes.

In this process, various TPC prototypes out of enameled coated copper wires were simulated in CST [Dassault Systèmes 2022], manufactured in the laboratory employing an electric drill, and measured using a VNA to test their applicability and suitability as a sensing TL for the given airbag application.

A focus was laid on the electrical response to mechanical bends rather than a good matching and transmission performance. Thereby, two essential configurations were tested. First, conventional TPC designs of transposing two enameled wires of different diameters and different twist rates were examined. In addition, a TPC structure around a dielectric core was created by transposing enameled wires in a helical way around a dielectric string, e.g., a low-density polyethylene (LDPE) or a polytetrafluoroethylene (PTFE)/ Teflon yarn [Lago et al. 2009]. A CST model of such a TPC structure including a dielectric core together with its cross-section view can be seen in Fig. 4.10(a). Three examples of manufactured TPC prototypes with a dielectric core, each of different twist rate equipped with SMA connectors, are depicted in Fig. 4.10(b).

4.4.1 TPC Prototype with Dielectric Core

For overview purposes, one TPC prototype is investigated and discussed here in greater detail. Other prototypes of different wire diameters, dielectrics, and twist rates are excluded for reasons of conciseness and brevity.

The here chosen prototype is seen in Fig. 4.10(b). It offers an enameled wire diameter of $d_w = 0.6$ mm and a diameter of the dielectric core of $d_d = 0.6$ mm.

Thereby, the mechanical flexibility of the TPC is mainly determined by its wire diameter $d_w = 0.6$ mm together with the corresponding twist rate. A rather small wire diameter is chosen together with a moderate twist rate to still ensure a high flexibility. Although, this poses a different problem, since, a decrease in wire diameter is accompanied by an

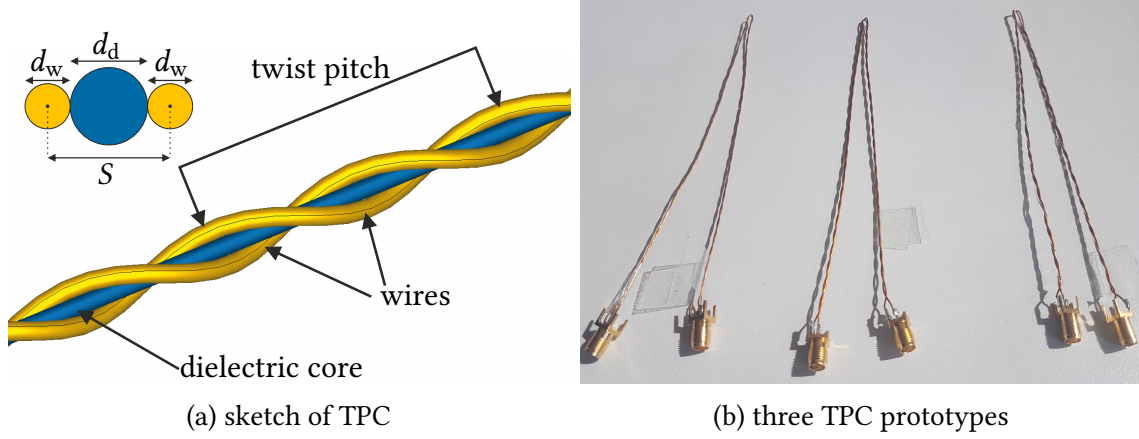


Fig. 4.10: (a) Image of the simulation model in CST of the TPC with a dielectric core of enamelled wires and cross-section view with according dimensions. (b) Image of three TPC prototypes of different twist rates with SMA connectors on either end.

increase in characteristic impedance Z_{TPC} of the TPC according to

$$Z_{\text{TPC}} = \frac{120}{\sqrt{\epsilon_{r,\text{eff}}}} \operatorname{arcosh} \left(\frac{S}{d_w} \right), \quad (4.1)$$

and following the notation of Fig. 4.10(a) in which S accounts for the spacing of the two wires, from conductor center to conductor center, and d_w represents the diameter of the wire [Lefferson 1971].

As stated before, a characteristic impedance on the order of 50Ω is aimed for, in order to establish a suitable impedance matching with the reflectometer of *Chapter 3*. The variable $\epsilon_{r,\text{eff}}$ accounts for the inhomogeneous dielectric since the wave along the two wires partly runs through air and partially in the dielectric.

The dielectric core is made of LDPE dielectric yarn with a permittivity of about $\epsilon_r = 2.3$ and a loss tangent of about $\tan \delta = 0.0004$ [Dassault Systèmes 2022; Pozar 2012]. The twist rate is chosen as $n = 100 \text{ m}^{-1}$. This twist rate is always a trade-off between mechanical flexibility on the one hand and electrical slow-wave properties on the other hand. Thus, the larger the twist rate, the more stiff and rugged is the TL, resulting in reduced sensitivity to mechanical deformation but also resulting in a slower phase velocity along the line due to the longer wires [Lago et al. 2009]. The dielectric core is mainly used

for two reasons. First, the phase velocity along the TPC is further reduced due to the dielectric, which in turn increases the range resolution. Besides, the core shall ensure a higher sensitivity to mechanical bends and kinks due to the reduced stiffness while still preserving a uniform geometry and hence a uniform characteristic impedance.

In the CST simulation model [Dassault Systèmes 2022], the time-domain solver was employed to obtain reference data in the frequency range from 0 to 6 GHz. Thereby, the characteristic impedance accounts for about $Z_{\text{TPC},s} = 140 \Omega$ according to the port mode solver, considering that this model is excited by waveguide ports. The waveguide ports establish a proper matching performance on the order of -20 dB throughout the frequency range. In addition, an attenuation of about 5 dB per meter is achieved.

The propagation velocity accounts for about $c_{\text{TPC},s} = 2.35 \cdot 10^8$ m/s, which results from an effective permittivity of $\epsilon_{r,\text{eff}} = 1.64$ in conjunction with a VF_s of 78%. Thereby, the effective permittivity considers the inhomogeneous dielectric since the signal travels partially through the air and partially through the dielectric when inspecting the structure in Fig. 4.10(a).

In contrast to the simulation model, in reality SMA connectors are directly soldered to the TPC structure, which induces mismatch due to the impedance jump and due to directly connecting an unbalanced to a balanced TL [Siebert 2003]. However, broadband RF impedance transformers or particular baluns, enhancing the matching performance, are very challenging to fabricate and hard to find in the given frequency range from several hundred MHz up to 6 GHz covering almost three octaves. Nevertheless, in the scope of this work, testing the TPC structure in terms of its bend sensitivity and, therefore, as a possible sensing TL structure was of greater interest than a well-matched TL.

4.4.2 VNA Measurement Results of TPC

VNA measurements of the TPC prototype described above were performed to obtain the two-port S -parameters by employing a VNA of type ZVL by Rohde & Schwarz together with prior calibration. Thereby, the employed bandwidth spans from 10 kHz up to 5 GHz resulting in a range resolution on the order of $\Delta r = 2$ cm due to a measured velocity of propagation along the TPC of $c_{\text{TPC},m} \approx 2 \cdot 10^8$ m/s. The TPC reveals a measured VF_m of about 66.7%. The primary line constants and by this means the velocity of propagation can be extracted from the measured S -parameters by employing Matlab [The MathWorks, Inc. 2022] and according to [Degerstrom et al. 2008; Eisenstadt and Eo 1992].

The recorded TDR results of the TPC prototype obtained by converting the measured S_{11} -parameter into a down-range scale can be seen in Fig. 4.11. Thereby, the TPC prototype is measured in three different states. First, its S -parameters are recorded in an unbent/straight form, subsequently with a 90° bend right in the middle, and finally with a severe bend in the middle of close to 180° .

Two effects are well seen when inspecting the plot in Fig. 4.11. First, the two SMA connectors constituting the beginning and the end of the TPC prototype are clearly seen due

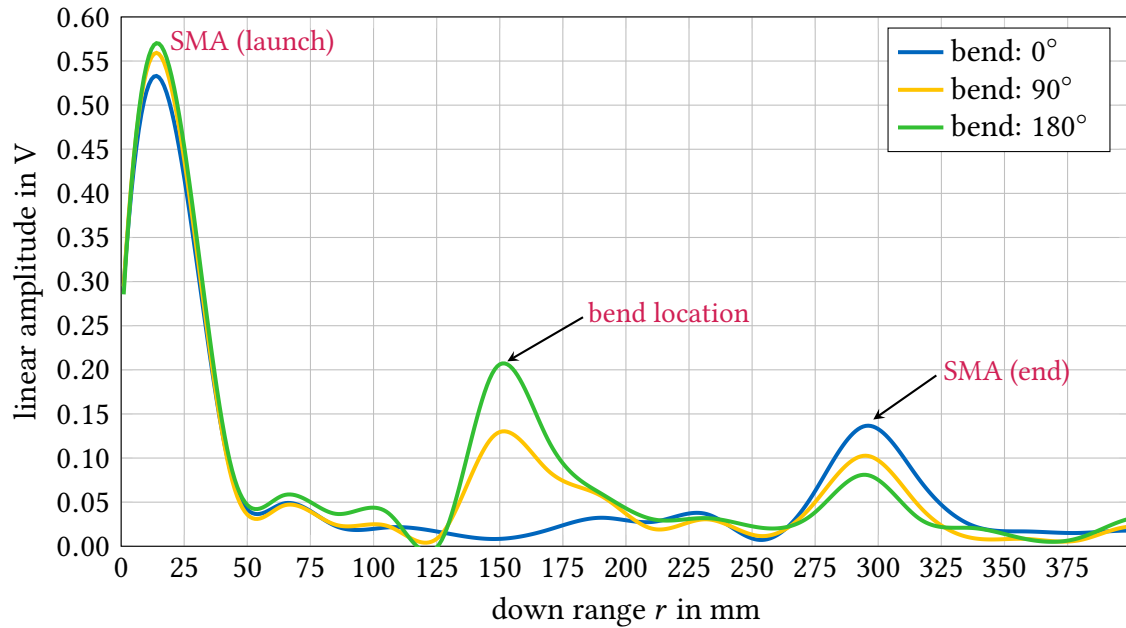


Fig. 4.11: TDR results of measured input reflection coefficient S_{11} of the TPC prototype of length 30 cm of Fig. 4.10(b) as transformed into time-domain and converted into a down-range scale. Three curves are seen. The blue one belongs to the straight version of the TPC with a bend angle of 0° , the yellow one represents the TPC being bent to about 90° in the middle, and the TPC being heavily bent of close to 180° is shown in green.

to the significant amount of mismatch they induce. Comparing these two peak heights at a location of about 0 mm and 300 mm, respectively, considerable losses along the TPC are noticeable, e.g., due to the skin effect [Schutt-Aine 2001]. The latter peak due to the rear SMA connector is significantly lower than the first one. This is caused by the high attenuation a signal undergoes after traveling two times the TPC length of about 600 mm. More importantly, when inspecting the results in Fig. 4.11, a clear difference of the bend status at the bend location at about 150 mm is detectable. Meaning, a more severe bend causes a larger local reflection. Even a linear relationship between bend angle and change in impedance is visible since the amplitude of the 180° is almost twice as strong as the amplitude of the 90° bend.

These results prove and demonstrate the suitability of such a TPC structure as a sensing TL. However, the losses along this TPC are so high in the given frequency range that it

can not be used for the intended application. Further TDR results of other TPCs are also reported, for instance, in [Schutt-Aine 2001] and [Siebert 2003].

To sum up, the TPC prototypes show promising features, e.g., they are straightforward, simple, and cheap to manufacture, and most importantly, they are mechanically lightweight and flexible. Furthermore, due to the twisting and dielectric core, so-called slow-wave properties are realized; hence, the propagation velocity along the TPC is reduced. Such a reduction of the phase velocity along the line results in an equal increase in range resolution, in accordance with (2.8). Also, it was seen that the twist rate highly influences the bend sensitivity. The simulation results could verify this.

On the other hand, the produced TPC prototypes account for several disadvantages as well. The promising simulation results could not be met in reality. First of all, the most significant obstacles concerning the aimed for airbag application are the very high losses at frequencies above 2 GHz to 3 GHz concerning both the matching and the transmission performance. The employed bandwidth of the FMCW reflectometer device of *Chapter 3*, spanning from 800 MHz to 6 GHz, can not even be exploited to its half, since above a frequency of 3 GHz, the matching and transmission performance revealed such poor values that the TL structure is not favorable for applications employing the device.

Furthermore, a broadband matching in the above specified frequency range is also challenging to achieve since broadband baluns or broadband connector types inter-mating between an unbalanced coaxial TL and a balance TPC structure are challenging to realize [Siebert 2003]. Besides, the TPC became mechanically very stiff and tough to bend or kink with increasing twist rate. Also, the manufacturing process turned out to be error-prone, such that an ideal, homogeneous, and twisted geometry around a dielectric core over the total length of a TPC is hard to achieve.

Taking all these features into account, the completed TPC design turns out to be unfavorable for the given application. Due to this outcome, follow-up research in the field of TPCs was not performed within the scope of this work.

4.5 Chapter Summary

The major results of the two presented flexible transmission lines are now put in a nutshell. First, a stencil-printed, single-layer, highly flexible, elastic, and compact CPW directly attached to the surface of a car airbag was presented. Compared to other inks, the here employed ink offers a high conductivity considering its good mechanical properties such as good flexibility, elasticity, and strong adhesiveness. The suggested CPW prototype offers promising electrical and mechanical characteristics, especially considering the rough textile and lossy substrate, the irregular ink distribution, and also the manual, facile, and very cheap manufacturing process. The suggested CPW prototype on the car airbag substrate is applicable for frequencies up to 6 GHz. Stencil printing of RF planar TLs is a versatile manufacturing method and can be used for other applications as well, and possibly also for various other substrates. In addition, a twisted-pair cable out of enameled wire around a dielectric core was presented. Thereby, the transmission losses at frequencies above 2 GHz to 3 GHz were so high that other favorable features like slow-wave properties or simple and straightforward manufacturing could not be compensated. However, the manufactured twisted-pair cables showed a good bend sensitivity so that a distinction between a severe and a moderate bend was possible.

Measurement Results

Experimental measurement results recorded with the proposed FMCW reflectometer of *Chapter 3* are presented in the following. At first, static measurements of commercially available coaxial transmission lines are presented to demonstrate ranging capabilities, accuracy, sensitivity, as well as limitations, inherent systematic effects, or shortcomings. Afterwards, dynamic measurements are shown comprising a manually loosed and re-fixed match termination at the end of a transmission line, as well as discontinuities produced manually by hitting a line with a hammer. In the end, a monostatic FMCW radar setup is built by attaching an antenna instead of a transmission line to the output port. By this means, a manually rapidly moved corner reflector is tracked and traced. All here presented results have been acquired in a laboratory. Measurements of airbag-deployment procedures at test benches could not yet be performed. Similiar results as presented in this chapter have previously been published in [Möhring et al. 2021] and [Möhring et al. 2022].

5.1 Static Transmission Lines in Laboratory

The measurement results presented in this chapter have been obtained by employing the setup depicted in Fig. 3.5. Again, the high-speed DSO by Teledyne LeCroy of type WaveMaster 808Zi-A [LeCroy Corporation 2022] was utilized for recording these results due to its versatility in terms of sampling rate of up to 40 GS/s, its large bandwidth of 8 GHz, and its memory depth of 20 MS. Further processing, such as FFT-computing, filtering, and plotting of the so obtained results, was performed in Matlab [The MathWorks, Inc. 2022]. As stated previously, the full results of these static measurement scenarios can be obtained from recording a single-shot measurement.

5.1.1 Transmission Lines with Match Termination

The first measurement setup shall provide an overview and showcase the performance features of the designed and fabricated FMCW reflectometer. A focus is laid on its accuracy, ranging capabilities, sensitivity, and suitability for the proposed application. Furthermore, existing limitations, systematic errors, or other effects are also demonstrated. Since this work deals primarily with detecting and ranging soft-faults, hence weakly reflective targets, the here investigated transmission lines are terminated by a match to avoid significant reflections from an open-circuited or short-circuited end. Furthermore, due to the given application within very short-range, occurring large reflections would lead to strong multiple reflections bouncing back and forth, thereby impairing the accuracy as well as readability of these results.

The first simplified measurement setup is seen in Fig. 5.1. It comprises the final assembly of the FMCW reflectometer together with an attached TLUT. Again, this TLUT consists of two transmission lines of identical construction, each of length $l_1 = 61$ cm connected by a joint connector of length $l_2 = 2.2$ cm, and terminated by a match at the rear end. All these parts were manufactured by Mini-Circuits. The two lines are of type Mini-Circuits 086-24KM+ containing a low-loss PTFE dielectric with a permittivity of $\epsilon_r = 2$. Following (2.58), this permittivity results in a VF of about 0.707 and a corresponding velocity of propagation along the line of $c_{TL} = 2.119853 \cdot 10^8$ m/s. This VF information is essential for converting the obtained beat-frequency data into a correct down-range line scale.

All parts used here, such as the two lines, the joint, and the match termination, are standard 50 Ω -parts equipped with 2.92 mm-connectors, specified for frequencies of up to 40 GHz in the Ka-band. These parts were selected for the measurement due to their superior manufacturing accuracy and resulting good electrical performance in terms of RL , all offering an RL of at least 35 dB in the employed frequency range. More importantly, according to [Hiebel 2016], a match termination with an attenuation of better than 30 dB above 4 GHz is challenging to realize.

An LFM sawtooth chirp signal with a bandwidth of $B_{TX} = 5.2$ GHz, spanning from 800 MHz to 6 GHz, and a sweep time of $T_s = 1$ ms functions as the TX signal. Its bandwidth together with the propagation speed c_{TL} on the TL due to the VF, results in a range resolution of about $\Delta r = 2.04$ cm along the line, following (2.8). Thereby, the TX signal is coupled into both the TLUT and the LO port of the receiving mixer, respectively. At the corresponding discontinuities or transitions, a part of the TX signal is reflected back to the receiver taking the respective round trip times of (2.11), constituting the RX signal in accordance with (2.9). The amount of reflection at each discontinuity can be computed by the local reflection coefficient of (2.10) or likewise of (2.60).

The down-range profile of the TLUT of Fig. 5.1 has been acquired by first of all recording the resulting IF beat signal, following (2.12). Subsequently, performing an FFT of the IF beat signal yields the individual beat frequencies as provoked by each discontinuity. According to (2.13), the Doppler frequency component within the beat frequency is zero, $f_D = 0$, due to considering static discontinuities and transitions only. The beat frequency data in the frequency-domain can be converted into the desired down-range scale of the

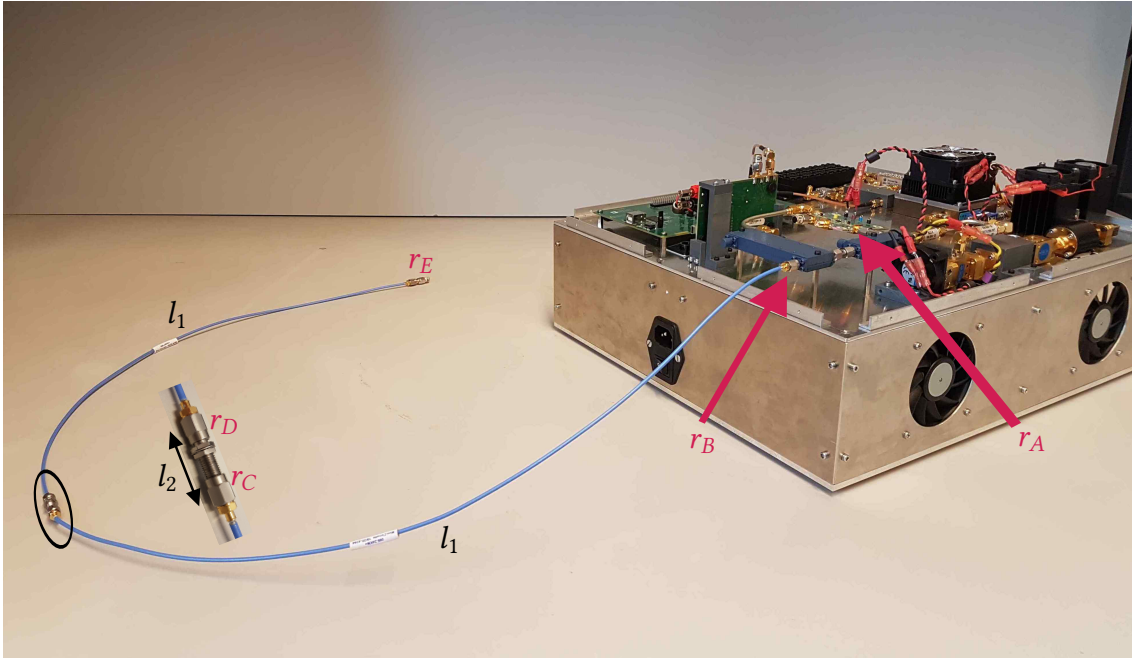


Fig. 5.1: Photograph of simplified measurement setup comprising FMCW reflectometer together with an attached TLUT. This TLUT comprises two identical transmission lines, each of length $l_1 = 61$ cm connected by a joint connector of length $l_2 = 2.2$ cm, and terminated by a match. The variables r_A to r_E mark possible discontinuities due to interconnection locations.

TLUT by employing (2.13) and inserting the known TX chirp parameters like bandwidth $B_{\text{TX}} = 5.2$ GHz and sweep time $T_s = 1$ ms. Thereby, the IF signal needs to be sampled at least by 200 kHz, since for this setup the maximum beat frequency $f_{b_{\text{max}}}$ can reach up to 100 kHz, following (2.14), when setting the maximum range r_{max} to 2 m.

The resulting down-range plot in a linear scale can be seen in Fig. 5.2. Five significant peaks are seen there, r_A to r_E . All five peaks vary in height since they all represent different discontinuities. At zero down-range, the first peak location r_A accounts for the inherent leaked-through LO signal into the RX path, known as direct spillover or TX-to-RX spillover, which is common in monostatic FMCW radar or reflectometer setups, as mentioned in the previous chapters [Beasley et al. 1990; Li and Wu 2008; Lin et al. 2006; Park et al. 2019, 2021]. This leakage arises from the limited isolation of the RX

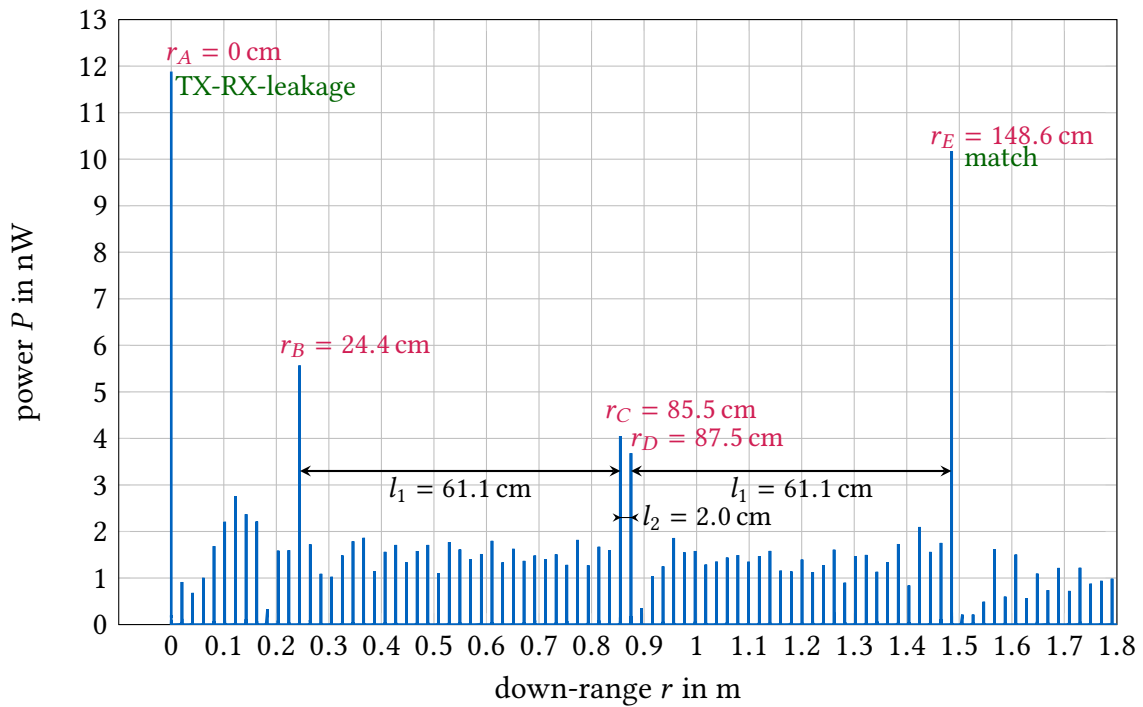


Fig. 5.2: Measured down-range profile of two interconnected transmission lines, each of length $l_1 = 61$ cm. A joint of length $l_2 = 2.2$ cm is used for interconnecting and a match terminates the rear line. The five peak locations in down-range, r_A to r_E , mark the TX-to-RX-spillover (r_A), the transition from the output coupler to the first TL (r_B), both ends of the short joint connector (r_C and r_D), and the final match termination (r_E).

from the TX port, as observed by the S-parameter S_{31} of Fig. 3.6. This leaked-through LO signal also causes an elevation of the neighboring noise level at about 10 cm to 20 cm when investigating the plot in Fig. 5.2.

The second peak at $r_B = 24.4$ cm marks the output port of the 3 dB-coupler and constitutes the input/output port of the reflectometer. This impedance mismatch results from connecting a 2.92 mm-connector of the first TL to an SMA-connector of the 3 dB-coupler. SMA-connectors and 2.92 mm-connectors are mechanically well intermateable but reveal slightly different dimensions together with minor electrical performance differences according to [Pino 2007].

This peak r_B can be considered the output port of the device. The measured range of about 24 cm correlates with the path length that the signal travels within the dual-directional coupler structure, as seen in Fig. 3.8.

The closely neighboring peaks r_C and r_D indicate both ends of the employed short joint connector of length $l_2 = 2.2$ cm. These results highlight the reflectometer's accurate ranging capabilities due to the significant bandwidth of the TX signal of 5.2 GHz. A joint connector offering a length slightly larger than the range resolution can still be resolved as two distinct targets, as seen in Fig. 5.2. The final peak r_E marks the match termination of the latter transmission line. It is of considerable height since the absorbing capabilities vary over such a wide frequency range spanning from 800 MHz to 6 GHz. These variations are compressed into a single frequency- and thereby range-bin.

The measured lengths of the employed transmission lines can be computed by subtracting the peak location r_B from r_C for the first line and subtracting r_D from r_E for the second line, respectively. It is evident that the measured cable lengths of the two cables of length $l_1 = 61$ cm and the joint connector of length $l_2 = 2.2$ cm come close to the actual physical cable lengths of 61.2 cm and 2.2 cm, respectively.

All in all, these results show that even small discontinuities like the cable transitions or the match termination are well detectable with the reflectometer, which proves the good sensitivity in a very short-range of less than two meters. Furthermore, a correct ranging of the cable and joint lengths is recognizable.

A series of measurements of the setup in Fig. 5.1 were recorded to identify the measurement uncertainty. Thereby, a good repeatability of the results of Fig. 5.2 was noticeable. Nevertheless, peak deviations of single discontinuities in respect of magnitude on the order of up to ± 0.7 nW were measured, while the range jitter or range fluctuation margin was throughout less than the size of one range cell.

The linear scale of Fig. 5.2 can also be converted into a logarithmic dBm scale. Herein, a peak height of, for instance, 1 nW correlates with a dBm value of -60 dBm, which comes close to the noise level, i.e., the lower sensitivity bound of the device for this setup in very short range. The sensitivity or noise level mainly arises from the TX signal power of about -3 dBm as injected into the TLUT in conjunction with its SFDR. As seen in Fig. 3.12, this SFDR is impaired by spurious content arising from the DDS itself and also from the frequency multiplier chain.

Furthermore, the sensitivity or noise level also depends on the sweep time, the distance from the DC bin, and also on the ambient temperature. Especially cable loss and attenuation effects are temperature dependent. Discontinuities resulting in a mismatch below that threshold can not be detected with the reflectometer and get lost in the noise floor. Besides, unlike commercial VNAs that employ calibration standards to eliminate systematic errors present in the measurement, the results obtained here with the reflectometer are performed without a prior calibration procedure.

5.1.2 Transmission Lines with Bend Location

A second measurement was performed following the setup shown in Fig. 5.3. Thereby, a first TL of length $l_3 = 183.5$ cm is connected to a second TL through a joint offering a length of $l_4 = 1.4$ cm. This latter line has a length of $l_5 = 49$ cm and is interconnected to a final match termination via a second joint of length $l_6 = 2.9$ cm. As seen in Fig. 5.3, this rear line is bent halfway at a distance of about $l_5/2$. All these parts are equipped with standard SMA-connectors and offer an RL performance in the given frequency range of 40 dB and above according to the data sheet.

This setup is selected to showcase the capabilities of the reflectometer to detect and reliably range bend locations along a TL, but furthermore to also highlight the limited range resolution capabilities in case of considering discontinuities smaller than the inherent system range resolution. In this context, the first joint of length $l_4 = 1.4$ cm is slightly shorter than one range cell size, while the latter joint of length $l_6 = 2.9$ cm stretches over about 1.5 range cell lengths.

Again, an LFM sawtooth chirp signal with a bandwidth of $B_{TX} = 5.2$ GHz was injected into the TLUT, resulting in the same range cell size as in the setup above of $\Delta r = 2.04$ cm due to a permittivity of the TLUTs of $\epsilon_r = 2$. This time, the chirp reveals a sweep time of $T_s = 2$ ms. The acquired down-range plot of the TLUT of the setup of Fig. 5.3 is depicted in Fig. 5.4.

At this point, the range plot is calibrated to the reflectometer output port; hence, the first peak r_A at zero range marks the transition to the first transmission line. The second peak at r_B indicates the transition from the first TL to the second TL via the first joint connector. Since the utilized joint connector is of length $l_4 = 1.4$ cm and thereby smaller than one range cell, it can not be resolved as two separated discontinuities as in the previous case but smears into one target.

This effect is common in FDR systems and results from the limited employed bandwidth by which means two reflections merge into a single bin/lobe of the FFT. The authors of [Ybarra et al. 1995] and [Vanhamme 1990] also address this shortcoming and suggest optimization approaches. Furthermore, this second peak at r_B also reveals the measured cable length of the first TL to $l_3 = 184.9$ cm, which differs from the actual physical length of 183.5 cm within the mentioned range resolution accuracy.

The highest peak and hence most potent reflection marks the bend location at r_C due to the mechanical squeezing and bending of the TL. Like in the actual setup, it lies about halfway between the peaks of r_B and r_D . The resulting measured cable length for this second TL amounts to 46.2 cm, deviating from the actual cable length of $l_5 = 49$ cm due to the limited range resolution on both ends.

The final match termination is marked by the peak r_E , which is interconnected to the second transmission line employing a joint with the actual length of $l_6 = 2.9$ cm. In contrast, the device ranges this latter joint connector to a length of 4 cm, which accounts for two range cells, by subtraction peak r_E from peak r_D .

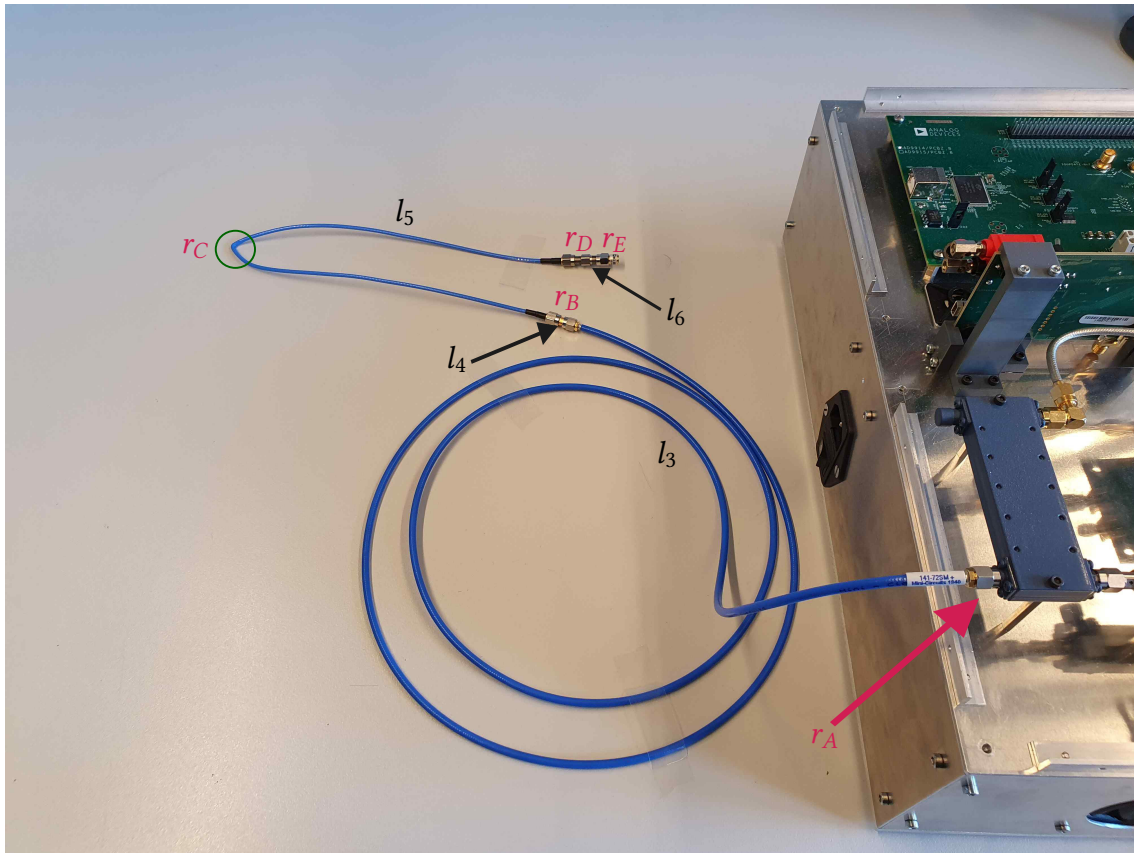


Fig. 5.3: Photograph of simplified measurement setup comprising FMCW reflectometer together with a TLUT. This TLUT consists of two transmission lines of different lengths, $l_3 = 183.5$ cm and $l_5 = 49$ cm, which in turn are interconnected by joints of lengths $l_4 = 1.4$ cm and $l_6 = 2.9$ cm, respectively. The latter line is terminated by a match and bent halfway at a distance of about $l_5/2$. The marks r_A and r_E highlight possible discontinuities. All parts were manufactured by Mini-Circuits and are equipped with standard SMA-connectors.

The results prove the possibility of detecting and ranging soft-faults in the form of a bent transmission line with the reflectometer with a range resolution on the order of 2 cm. Furthermore, it was shown that discontinuities shorter than the range resolution, for instance, the first joint transition of length $l_4 = 1.4$ cm with its two connections on both sides, can not be resolved as two separate targets.

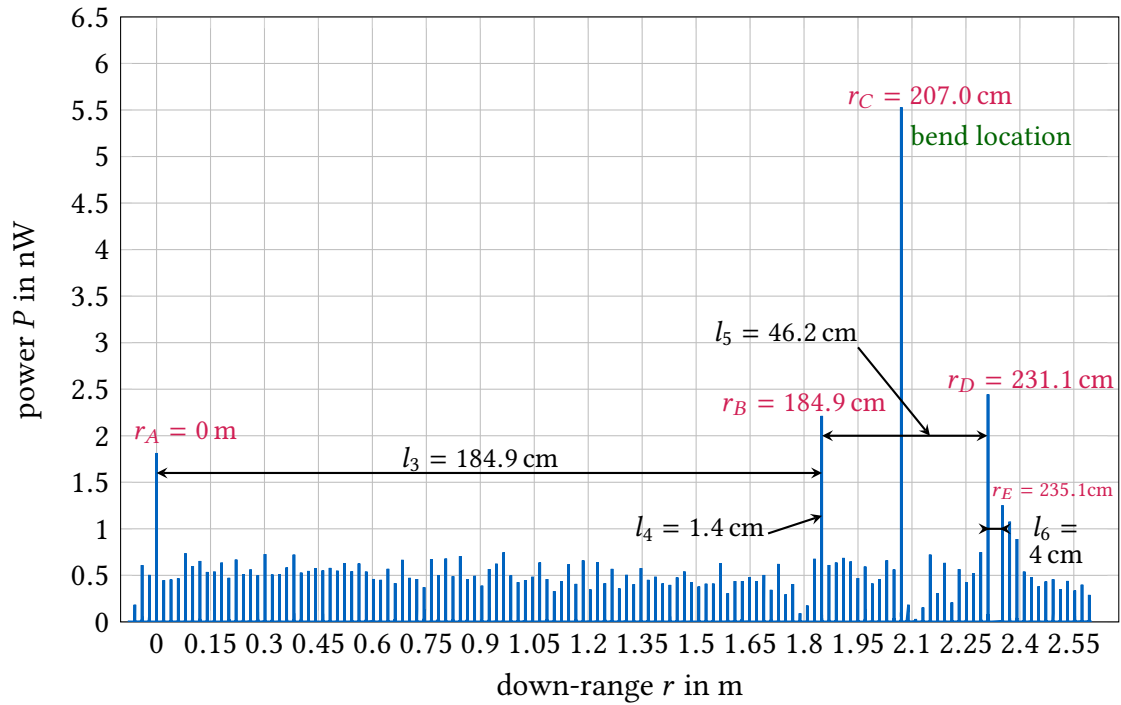


Fig. 5.4: Measured down-range profile of TLUT setup of Fig. 5.3. The first peak r_A marks the transition from the output port to the TLUT. The bend location is marked by the peak at r_C , while both ends of the latter TL are indicated by the discontinuities at r_B and r_D . The peak at r_E represents the match termination.

A comparable range resolution on the order of a few centimeters is reported, for instance, in [Furse et al. 2003] or [Smith et al. 2005], while [Tsai et al. 2005] reports a resolution of about 10 cm. The authors of [Lee et al. 2013] and [Shin et al. 2005] achieved an error of several centimeters, while in [Sharma et al. 2007] an accuracy of up to one foot is demonstrated.

The results shown in Fig. 5.3 were well repeatable after recording the same setup several times. Thereby, the range jitter was consistently less than the range cell size. In terms of magnitude, peak deviations of individual discontinuities in terms of the magnitude of up to ± 0.8 nW were noticed, mainly arising from the bend location at r_C , which tends to be sensitive to minor mechanical movement, the bend degree, and the physical arrangement of the whole TLUT in the laboratory.

5.2 Dynamic Discontinuities along Transmission Line

In the following, not only static discontinuities along transmission lines are investigated and tracked, but also time-varying ones are monitored. These results shall demonstrate the capabilities of locating, ranging, and tracking varying faults along transmission lines with the reflectometer by exploiting its fast sweeping capacity with multiple shots.

5.2.1 Loose Match Termination

With this in mind, the measurement setup shown in Fig. 5.3 is modified. Now the latter line of length l_5 is removed and the first line of length $l_3 = 183.5$ cm is terminated by a match at location r_B .

This match termination is now two times gradually and carefully loosened and re-fixed again by hand via slightly off- and on-screwing the termination with an SMA-connector. However, the match is never fully unscrewed but only loosened a bit in order to not produce a significant reflection but rather a tiny and time-varying discontinuity that can be considered a soft-fault. This loose match shall represent a broken or loose transition, a damaged connector, or a loose match termination with a limited and unstable absorbing performance. The beat frequencies f_b as provoked by this loose match termination recorded over time in a spectrogram representation can be seen in Fig. 5.5.

Examining the plot in Fig. 5.5, two horizontal lines at about 11.98 kHz and 101.83 kHz are noticeable, marked by the variables r_A and r_B . Those two reflections indicate the beginning and the end of the transmission line of the actual physical length of $l_3 = 183.5$ cm. The lower one at r_A is static, while the intensity of the upper at r_B is varying over time. By considering the bandwidth of the TX signal $B_{TX} = 5.2$ GHz and the sweep time of $T_s = 2$ ms, the beat frequency scale can be converted into a range scale by employing (2.13). Thereby, a measured beat frequency of $f_{b,A} = 11.98$ kHz corresponds to a down-range of $r_A = 24.4$ cm, while the down-range at the match location accounts for $r_B = 207.6$ cm in accordance with a beat frequency of $f_{b,B} = 101.83$ kHz. Subtracting these two ranges from one another results in a measured cable length of 183.2 cm, which matches the actual cable length quite well.

Furthermore, the gradually increasing reflection intensity is seen, starting at about 0 s and 3 s, respectively, marking the match termination's manually loosening. Besides, the re-fixing of the match termination is recorded. It starts at about 1.5 s and 4.5 s, respectively, as shown by a decrease in power of the beat frequency.

Within the time interval of 2.4 s to 3.1 s, the match is fully fixed and screwed on tight to the TLUT, resulting in a low local reflection, as is the case after 5.5 s.

A second measurement result, analogous to the one described above, is shown in Fig. 5.6 in a mesh surface spectrogram plot. Through the 3D visualization of the obtained results, the gradually increasing and decreasing reflection intensity through manually off- and on-screwing of the match is nicely seen. Furthermore, the static discontinuity from the connection of the TLUT to the reflectometer is seen at about 0.25 m.

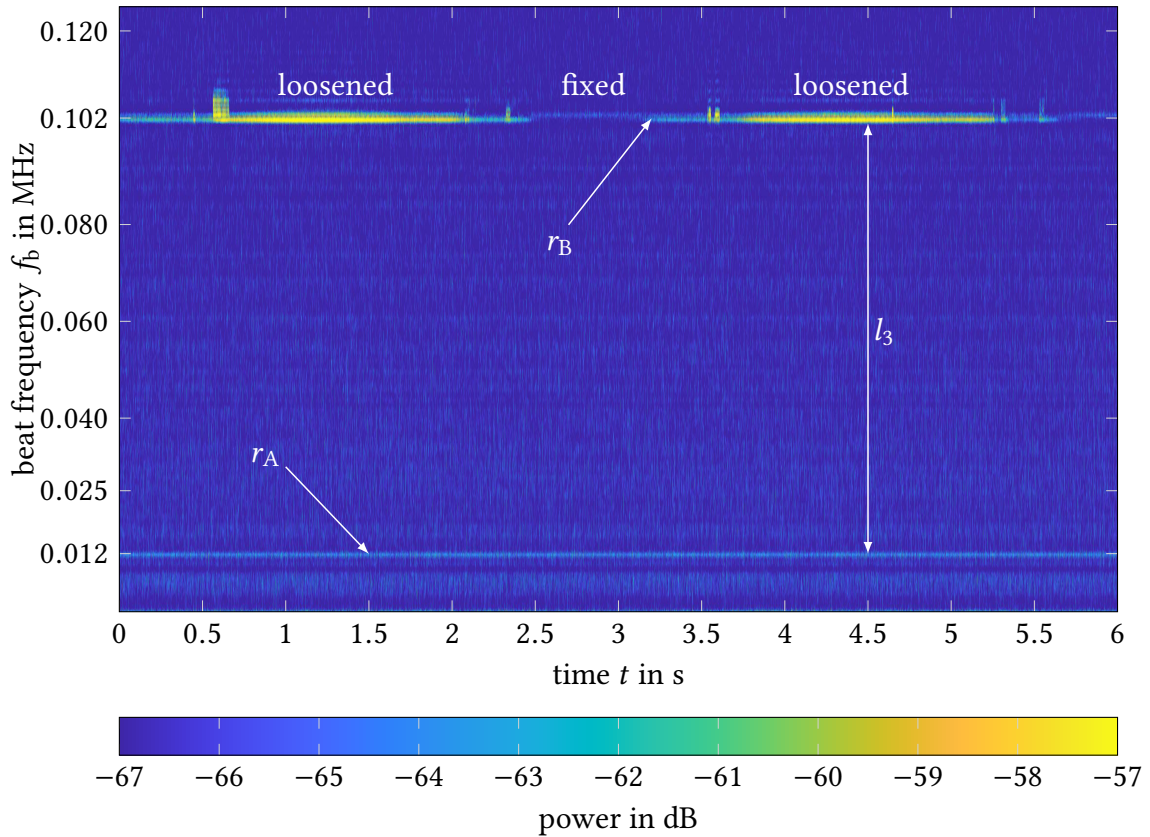


Fig. 5.5: Spectrogram plot of recorded beat frequencies f_b of transmission line of length l_3 with a loose match termination, as shown in Fig. 5.3. The match termination is two times slightly loosened and re-fixed by hand, resulting in a gradual increase and decrease over time, respectively, of the measured beat frequency at location r_B .

The high peak just under 1 s is a significant mismatch resulting from the manually and hence imprecise and unsteady screwing process.

Another effect is also apparent when inspecting the plot in Fig. 5.6. The noise floor decreases with distance from the 0 m bin or DC bin due to the TX-to-RX leakage at the first few range cells, which elevates the noise floor significantly. For that reason, other groups add additional length to the TLUT to avoid or at least remedy that shortcoming in very short range. In other words, the overall sensitivity of this device increases with distance from the DC bin.

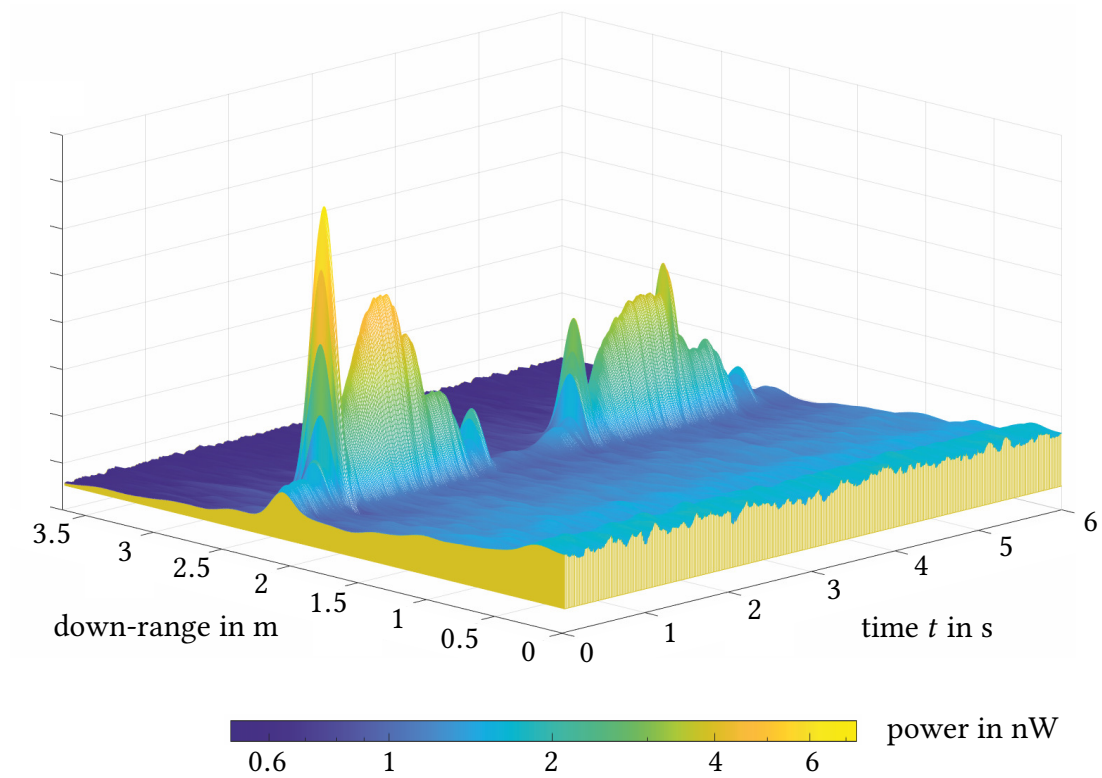


Fig. 5.6: Mesh surface spectrogram plot of recorded beat frequencies f_b converted into a down-range scale as provoked by a loose match termination at about 2.1 m range in accordance with the setup depicted in Fig. 5.3.

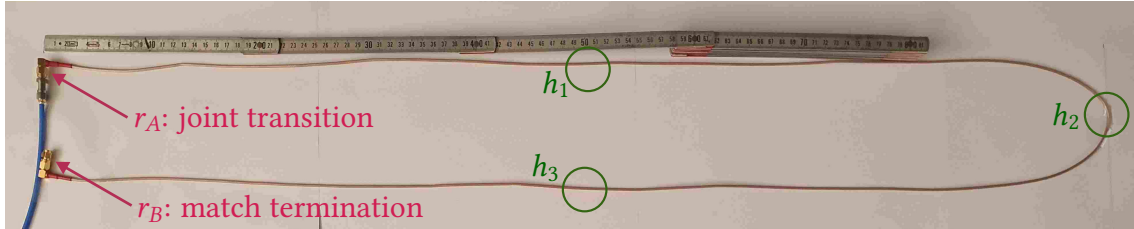


Fig. 5.7: Measurement setup comprising a transmission line of length $l_7 = 205$ cm terminated by a match and connected to the reflectometer by a blue feed line. By hand, three discontinuities are produced by slightly hitting the line with a hammer at about h_1 , h_2 , and h_3 . These hit locations are separated from one another by about 50 cm and also from the beginning at r_A and the end of the line at r_B , respectively.

5.2.2 Manually Produced Faults by Hammer Hits

Another dynamic measurement was performed according to the setup depicted in Fig. 5.7. A TLUT of length $l_7 = 205$ cm (80.7 inch) is connected to the reflectometer by a blue feed line, which is again terminated by a match at the rear end.

In that respect, the two indicated down-ranges r_A and r_B mark the beginning and the end of the TLUT, highlighting the joint transition and the match termination, respectively. Furthermore, three circles indexed h_1 to h_3 , indicating marks along the TLUT, are sketched.

These circles reveal a distance from one another of about 50 cm. Besides, the first mark h_1 has a distance of about 50 cm from the beginning of the TLUT (r_A), as well, as shown with the featured yardstick in Fig. 5.7. Likewise, the latter mark h_3 is separated from the match termination at the rear end by about 50 cm. These marks indicate the hit locations of the hammer hits which were performed during the measurement in order to produce suddenly occurring discontinuities along the TLUT.

The hits were performed with increasing intensity, meaning that the first hit at h_1 was performed very gently, while the second one at h_2 was conducted with a bit more strength. The final hit was performed with considerable severity.

A number of $L = 3000$ sawtooth-modulated TX chirp signals, each offering a sweep time

of $T_s = 2$ ms and bandwidth $B_{TX} = 5.2$ GHz, were injected into the TLUT, resulting in a total measurement time of $t_{mt} = 6$ s.

The measured beat frequencies of this setup converted into a down-range scale and calibrated to the beginning of the TLUT are shown in a spectrogram representation over the total measurement time in Fig. 5.8.

Due to the poor quality of the TLUT, the respective jointing locations at r_A and r_B are well seen in Fig. 5.8 as the two horizontal lines due to the resulting very poor RL performance at the connectors. The first transition at r_A reveals power values of about -40 dBm, while the match termination at r_B offers values of about -47 dBm. Furthermore, the three hammer hit locations are indicated, reflecting the increasing hit intensity.

The first hit h_1 at a measured down-range of about 54 cm from the joint transition at r_A is of minor magnitude of -59 dBm and is only present at the time of hit right after 0.5 s. No permanent damage of the TLUT is noticeable in Fig. 5.8; this fault was fully recovered. In contrast, the second hit at h_2 as performed right after 2.5 s was of a bit more intensity on the order of -56 dBm. This hit location is well seen in Fig. 5.8 at a range of about 102 cm. From that time on, a static discontinuity in the form of a horizontal line is visible, meaning that this fault was now permanent. The third hit was done at about 4.2 s at a measured down-range of 152 cm. This hit was of strong intensity and offers a measured value of -35 dBm. This hit resulted in a significant reflection and a local damage of the cable. This damage is well seen and it extends over several range cells, overshadowing the final match termination at r_B , as well. Due to this significant mismatch, a considerable amount of energy is reflected back, and less is transmitted further on to the final match termination. For that reason, the horizontal line, as seen in Fig. 5.8, immediately offers less intensity as soon as the cable is hit at h_3 at about 4.2 s. This problem is common and concerns all reflectometry methods. As soon as a significant discontinuity or fault is present along a TLUT, the remaining discontinuities after this significant fault are provided with a signal with less power than the ones before that fault. This means that the accuracy of reflectometry methods is impaired after a significant fault or discontinuity along a transmission line. This effect is nicely seen in Fig. 5.8.

The measured cable length of 202 cm and the hit locations differ within the ranging capabilities of the reflectometer. Furthermore, the hammer hit locations are also underlying some uncertainty and error due to its manual and hence imprecise execution. Also, the exact permittivity of the TLUT together with its corresponding VF is not known precisely, and therefore prone to errors and deviations. Again, a PTFE dielectric is assumed with a permittivity of $\epsilon_r = 2$.

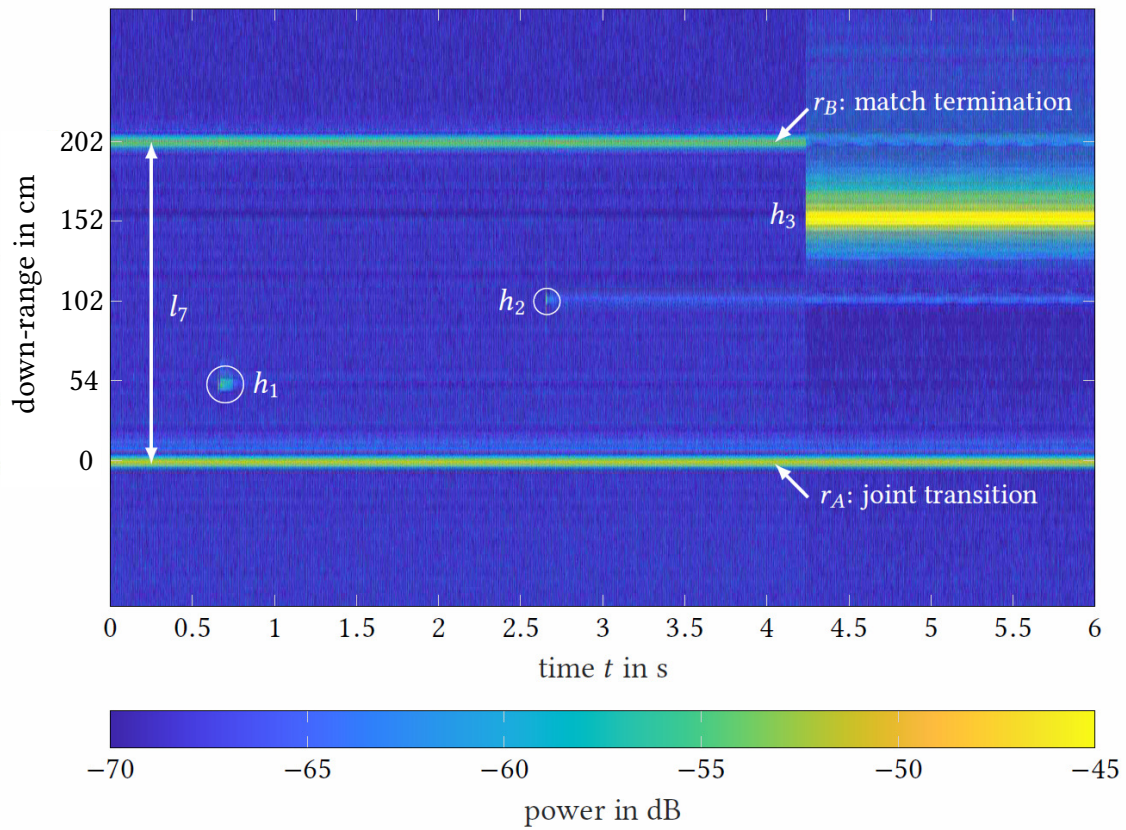


Fig. 5.8: Spectrogram plot of measured beat frequencies f_b of transmission line of length $l_5 = 205$ cm (80.7 inch) with a final match termination as depicted in Fig. 5.7 converted into a down-range scale. The cable was hit three times manually by a hammer with increasing intensity at about h_1 , h_2 , and h_3 , resulting in three local faults of different intensities. The two static lines mark the beginning and the end of the cable.

5.3 Monostatic FMCW Radar Setup

In the following, the basic structure of the FMCW reflectometer as shown in Fig. 3.5 and used in the previous measurement setups is modified. Now, instead of a TLUT, an antenna is connected to the output port of the reflectometer via a coaxial feed line. By this means, a monostatic FMCW radar setup is established, similar to the one shown in Fig. 2.1. This is done, in order to demonstrate the versatility of the proposed reflectometer for free-space radar operations. As a reference target, a trihedral corner reflector is employed.

Dynamic Tracking of Corner Reflector

Now, the FMCW radar is used to locate, track, and monitor the movement of a dynamically moved trihedral corner reflector in very short-range. Motivated is this setup for testing the designed FMCW radar for rapidly moving targets and fast ongoing procedures in free-space. Furthermore, besides the aimed for application of monitoring airbag deployment scenarios by means of FMCW reflectometry, it remains challenging to implement transmission line based measurement setups with rapidly occurring or moving faults or discontinuities in the laboratory.

A block diagram representation of the newly created measurement setup is depicted in Fig. 5.9. Besides the established reflectometer structure, an antenna and a trihedral corner reflector functioning as the reference target are seen. The authors of [Piotrowsky et al. 2019] present a resembling measurement setup that also comprises an FMCW radar and a corner reflector as a reference target placed on a linear track axis. This work also deals with accurate distance measurements in very short-range.

In the setup of Fig. 5.9, a linearly polarized double ridged horn antenna of model DRH400 by RFspin [RFspin 2022] is used to transmit the TX signal and to receive the RX signal. The antenna is specified for frequencies reaching from 400 MHz up to 6 GHz and thereby fully covers the frequency range of the reflectometer spanning from 800 MHz to 6 GHz. According to the datasheet, the antenna offers gain values reaching from about 9.6 dBi up to 14.2 dBi within the frequency range of the reflectometer [RFspin 2022].

The employed trihedral corner reflector is self-built, fabricated out of metal, and offers an edge length of $l = 29.7$ cm with a corresponding outer length of $L = l\sqrt{2} = 42$ cm, as indicated in Fig. 5.9. Recalling the formula for calculating the RCSs of such trihedral corner reflectors of (2.3), at the lower frequency bound of 800 MHz, the RCS accounts for about $\sigma_{\min, 800 \text{ MHz}} = -6.34$ dBsm. In contrast, at the upper frequency limit of 6 GHz the RCS rises to about $\sigma_{\max, 6 \text{ GHz}} = 11.16$ dBsm.

This calculated RCS value of the reflector varies significantly over the employed large frequency bandwidth of the reflectometer. Especially at the lower frequency bound, the RCS offers relatively poor values since the corner's edge length is shorter than one wavelength.

A photograph of this setup is seen in Fig. 5.10 to illustrate the dimensions of the antenna and the corner reflector, respectively, in contrast to the ones of the reflectometer. In this

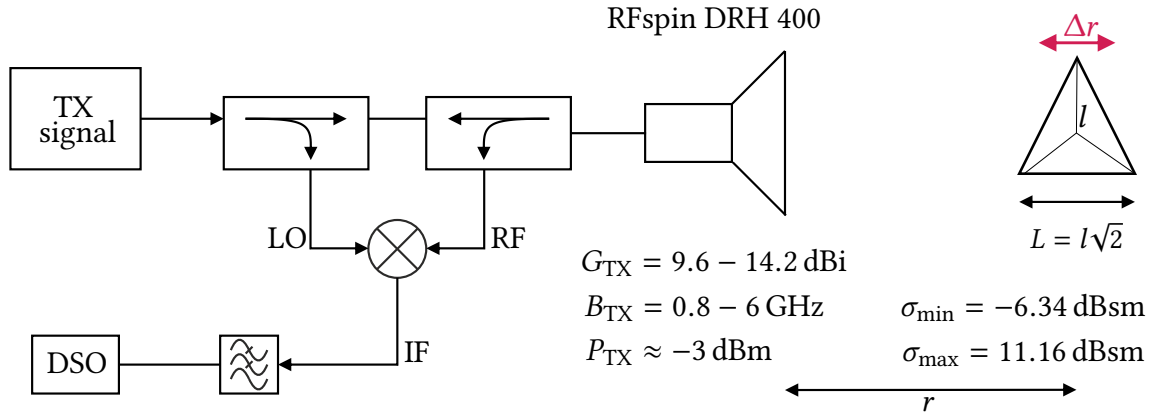


Fig. 5.9: Block diagram of monostatic FMCW radar setup comprising the FMCW radar including an antenna of type DRH400 by RFspin [RFspin 2022]. As a reference target, a trihedral corner reflector is employed and placed at a distance r right in front of the antenna. The reflector is manually, rapidly moved back and forth (Δr) in front of the antenna in very short-range.

picture, the reflectometer, the antenna, the corner reflector, the recording DSO on the far left, and a laptop are seen together with other measurement equipment.

Now, as indicated in Fig. 5.9 with the red arrow and the variable Δr , the corner reflector is rapidly moved back and forth by hand right in front of the antenna at a distance of about 2 m to close to 3 m during the measurement. This process is done manually with associated imperfections and variations but with considerable speed. Again, the TX signal offers a bandwidth of $B_{TX} = 5.2 \text{ GHz}$, reveals a sweep time of $T_s = 1 \text{ ms}$, and a transmit power of about $P_{TX} \approx -3 \text{ dBm}$ is fed to the antenna.

The recorded beat frequencies f_b over time due to the corner reflector movement in a spectrogram representation of this measurement scenario can be seen in Fig. 5.11. There, a sinusoidal behavior with 8.5 complete cycles within about 4 s is apparent, matching the reflector's rapid back and forth movement. Taking the length of the feed line into account, a frequency of 140 kHz correlates with a down-range of about 2 m, while the upper end of the beat frequency of 160 kHz of the plot in Fig. 5.11 corresponds with a down-range

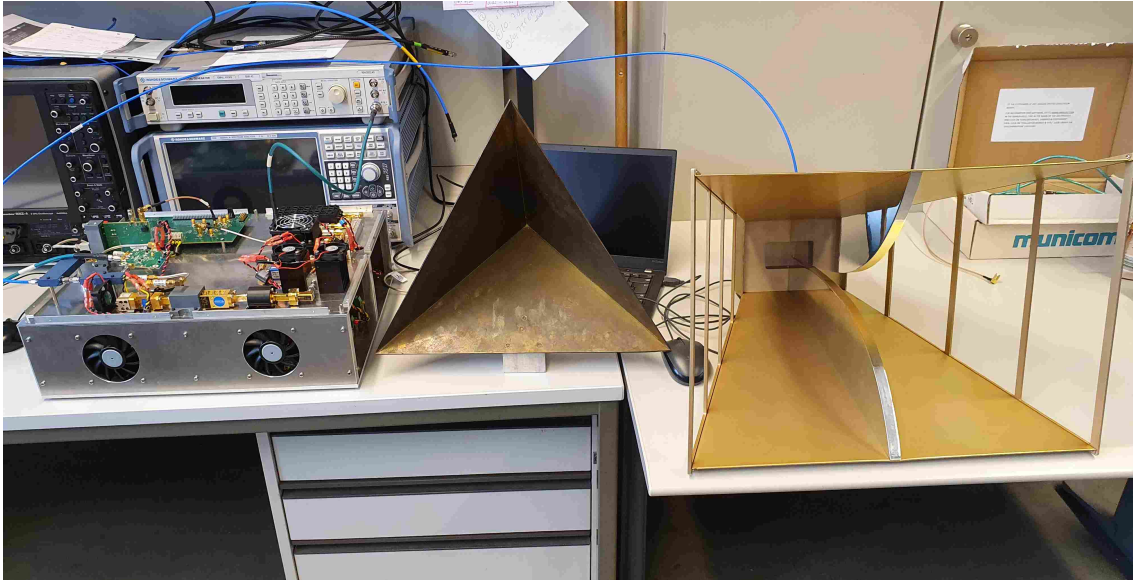


Fig. 5.10: Photograph of measurement setup in the laboratory of the block diagram of Fig. 5.9 comprising the FMCW reflectometer, the double rigged horn antenna by RFspin, the trihedral corner reflector, the DSO on the far left, and a laptop.

of 2.7 m, which represents the amplitude and extent of the movement of about 35 cm. However, due to the relatively low transmit power of about $P_{TX} \approx -3$ dBm, the significant fluctuation of the RCS of the reflector within one sweep, and the significant free-space loss, the setup is not ideal for measuring distances beyond several meters. It is limited to short-range scenarios.

Furthermore, it needs to be stated that the RCS is defined as a far-field quantity. Considering the size of the aperture of the antenna of about $D = 1$ m, the far-field region at the lower frequency limit of 800 MHz accounts for at least 5 m. In addition, at a frequency of 6 GHz, the far-field region begins even at a distance of over 40 m from the antenna. This means that the moving corner reflector is not located in the far field but instead in the near field of the antenna, which can also impair and alter the reflection behavior of the reflector. Also, the environment in the laboratory is not ideal for such measurement scenarios.

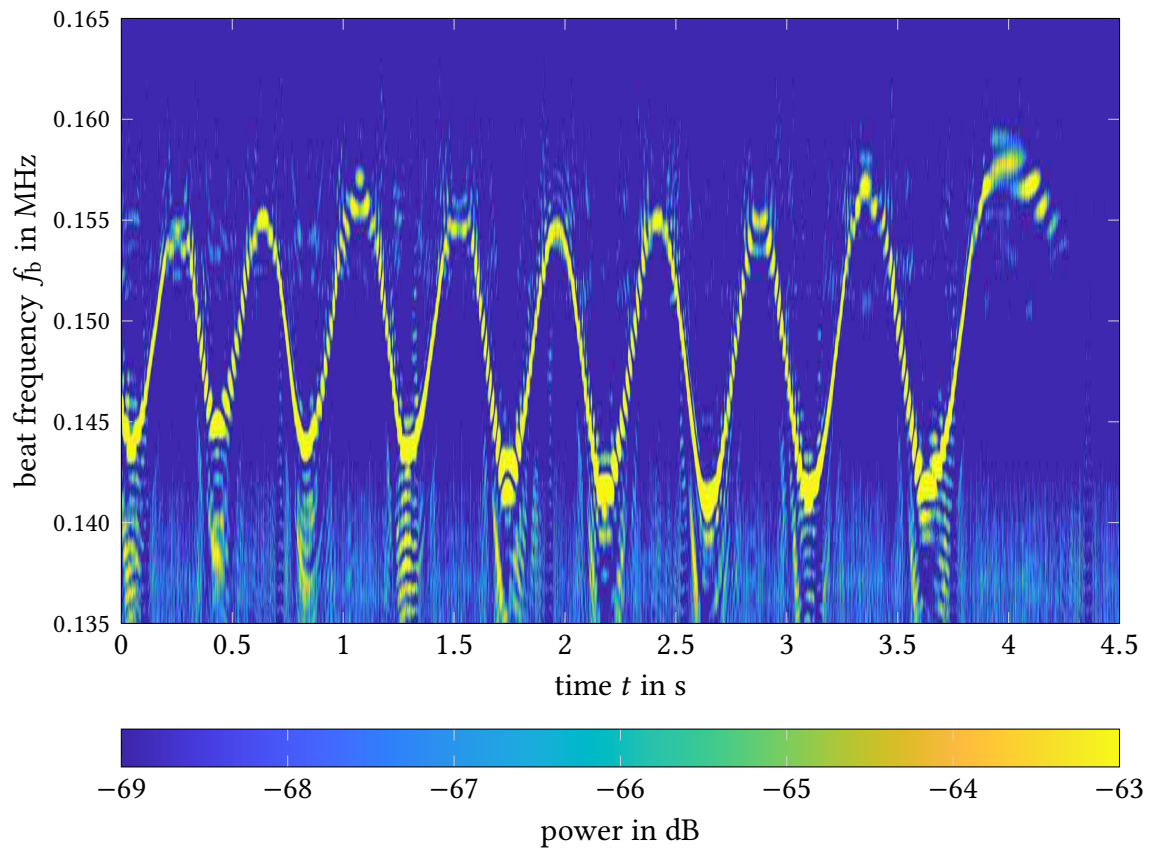


Fig. 5.11: Spectrogram plot of recorded beat frequencies f_b of rapidly moved corner reflector in close proximity of FMCW radar in accordance with the setup seen in Fig. 5.9.

5.4 Chapter Summary

Various measurement results have been presented with the realized reflectometer. A fine range resolution on the order of 2 cm due to the large signal bandwidth of 5.2 GHz was seen when employing commercial transmission lines. Also, high sensitivity for soft-faults like connector transitions, bends, discontinuities, or a loose match termination was observable due to the large dynamic range. Furthermore, because of the fast sweeping capabilities on the order of microseconds, quickly varying targets can also be tracked and monitored over time with this device. According results were presented in the form of a manually loosened and re-fixed match termination, manually produced hammer hits along a transmission line, or a dynamic tracking of a rapidly moving corner reflector in very short-range.

Conclusions and Outlook

6.1 Conclusion

A portable fast chirp FMCW radar measurement device for detecting and tracking discontinuities on transmission lines has been presented. The work was motivated by implementing and establishing an additional measurement technique for airbag deployment processes at test benches. Still present uncertainties about the rapid and difficult-to-access deployment procedure of a car airbag together with various shortcomings and limitations of available measurement and simulation approaches demanded additional research in this field. To address these demands, a transmission line-based reflectometry measurement device was designed and built to be used as a supplemental measurement technique to monitor airbag deployment processes. Therefore, the fast chirp FMCW radar principle is adopted to transmission lines constituting a novel FDR method. A particular focus was laid on the signal generation of the radar. The airbag monitoring application demands very fast swept transmitting signals to track agile and fast varying targets with sufficient update rate in conjunction with a fine range resolution on the order of centimeters.

In this process, a DDS-driven analog frequency multiplier chain was designed to enhance bandwidth and thereby range resolution and to preserve inherent benefits of DDS technology, such as high linearity, superior phase noise performance, immunity against aging, temperature drifts, and most importantly, high-speed sweeping capabilities. In the design process, particular attention was laid on the dynamic range of the TX signal since a high dynamic range is needed for the detection of soft-faults, small discontinuities, or bends of the transmission line, which only result in minor impedance variations. As a result, the radar operates on highly linear either triangular or sawtooth-modulated chirp signals with a signal bandwidth of 5.2 GHz spanning from 800 MHz to 6 GHz and a fast sweep time of down to 10 μ s. All needed RF and other supplemental components of this radar were assembled in a compact and portable housing for in-field measurements, including DC supply, cooling, and further auxiliary devices.

Various other bandwidth enhancement solutions employing a DDS as a signal source were outlined and tested in the design and research process of this work. Those solutions were not put into practice since they were outperformed by the overall results of the DDS-driven frequency multiplier chain. Those approaches comprise a direct signal duplication in baseband, a self-mixing attempt, an SNO of the DDS, as well as an IQ up-conversion and subsequent multiplication approach.

Measurement results of the realized FMCW radar in the laboratory demonstrate the effectiveness and versatility of the approach. Thereby, various static discontinuities such as cable transitions, bends, match terminations, or other discontinuities were correctly detected and ranged with the device with a fine range resolution on the order of 2 cm. Also, time-varying discontinuities in the form of manually and suddenly occurring faults produced by hammer hits or an on and off screwed match termination were monitored over time. In addition, a free-space monostatic FMCW radar setup was arranged in the laboratory. Thereby, a manually and rapidly back and forth moved trihedral corner reflector was tracked in a very short-range, highlighting the capabilities of tracing and monitoring fast-moving targets.

The presented FMCW reflectometer approach is a promising alternative to conventional time- or frequency-domain reflectometry techniques in locating faults and discontinuities on cables or transmission lines.

The second part of this work dealt with investigating and designing flexible transmission line structures for airbag surfaces. Thereby, a stencil-printed CPW was directly attached to the surface of the airbag employing a conductive ink. The so designed CPW offers good electrical performance and, besides, promising mechanical properties like good flexibility, elasticity, and strong adhesiveness considering the rough and lossy airbag substrate, the irregular ink distribution, and also the manual, facile, and very cheap manufacturing process. The suggested CPW prototype on the car airbag substrate is applicable for frequencies up to 6 GHz taking into account moderate losses.

In addition, TPCs around a dielectric core out of enameled wire were developed as a possible bend sensor for this application. The electrical transmission behavior above frequencies of two to three GHz was so adverse that investigations and applications of this TL structure were not further pursued. However, experiments of bend behavior showed that a severe bend could well be discriminated from a medium bend or unbent TPC. Nonetheless, this TPC prototype also showed favorable features like slow-wave properties or simple and straightforward manufacturing.

6.2 Outlook and Future Research

In the future, the here presented radar device is to be tested for the aimed airbag deployment monitoring application at test benches to assess its efficacy for this highly dynamic unfolding process. Therefore, off-the-shelf commercial coaxial transmission lines can be used, but also a larger version of the stencil-printed CPW of *Chapter 4*. Furthermore, additional research is needed to find a well-suited transmission line structure that is electrically well performing but also mechanically sensitive to bends and kinks. This appears to be challenging since RF transmission line structures were not as favorable as a bend indicator, especially for small and minor bends and kinks. Furthermore, a highly flexible and low-loss RF transmission line structure is difficult to realize simultaneously since well-conducting material is often rather stiff and hard to deform. In contrast, printed and flexible inks only offer a very limited conductivity, inducing significant losses, especially at higher frequencies. As other groups show, a large dynamic range is needed to detect and locate such minor bends and soft-faults which arise from a bent transmission line. Since commercial DDS chips only offer a limited dynamic range as compared to analog sources, further research and improvement is needed in that field. Besides, this fast chirp FMCW radar can be used for various monitoring and tracking purposes of fast ongoing procedures in very short range. Also, it could be extended to long-range operations when using additional amplifiers.

Nomenclature and List of Symbols

Nomenclature, Mathematical, and Physical Constants

Symbol	Description
x or X	scalar
\mathbf{x} or \mathbf{X}	vector
\mathbf{x} or \mathbf{X}	matrix
$ X $	magnitude of a vector
$\hat{\mathbf{x}}$	unit vector
*	complex conjugate
$f(\cdot)$	function
j	imaginary unit, $j = \sqrt{-1}$
e	Euler's number, $e \approx 2.178$
π	pi, $\pi \approx 3.14159$
c_0	speed of light in vacuum, $c_0 = 299\,792\,458$ m/s
ϵ_0	permittivity of vacuum, $\epsilon_0 \approx 8.854 \cdot 10^{-12}$ As/(Vm)
μ_0	permeability of vacuum, $\mu_0 = 4\pi \cdot 10^{-7}$ Vs/(Am)
η_0	characteristic impedance of vacuum, $\eta_0 = 120\pi \Omega = 376.73 \Omega$

List of Roman Symbols

Symbol	Unit	Description
a_i, b_i	\sqrt{W}	incident, reflected power waves at port i
a_{RX}	V	amplitude of received signal
a_{TX}	V	amplitude of transmitted signal
B	Vs/m ²	magnetic flux density
B	Hz	signal bandwidth

Symbol	Unit	Description
B_{DDS}	Hz	signal bandwidth of DDS
B_{TX}	Hz	transmitted signal bandwidth
c	m/s	velocity of propagation
c_{TL}	m/s	velocity of propagation along transmission line
C'	As/(Vm)	capacitance per unit length
D	As/m ²	electric flux density
D	m	antenna diameter
E	V/m	electrical field
E_{inc}	V/m	magnitude of incident electric field
E_{sca}	V/m	magnitude of scattered electric field
f	Hz	frequency
f_{b}	Hz	beat frequency
f_{clk}	Hz	clock frequency
f_{D}	Hz	Doppler frequency
f_{LO}	Hz	local oscillator frequency
f_{r}	Hz	range frequency shift
f_{SMP}	Hz	sampling frequency
f_{sta}	Hz	start frequency
f_{stp}	Hz	stop frequency
G'	A/(Vm)	conductance per unit length
G_{RX}	dBi	gain receiving antenna
G_{TX}	dBi	gain transmitting antenna
H	A/m	magnetic field
h_i	m	hit locations
i		arbitrary count variable
I	A	electric current
IL	dB	insertion loss (IL)
J	A/m ²	electric current density
k	1/m	wave number
\mathbf{k}	1/m	wave vector
l	m	edge length, length
L		number of transmitted chirps
L'	Vs/(Am)	inductance per unit length
M		arbitrary count variable
\mathbf{M}	A/m	magnetization vector
$\hat{\mathbf{n}}$		normal unit vector
P	As/m ²	polarization density
P_{inc}	VA	incident power
P_{out}	VA	output power

Symbol	Unit	Description
P_{ref}	VA	reflected power
P_{RX}	VA	received power
P_{tra}	VA	transmitted power
P_{TX}	VA	transmitted power
r	m	distance, down-range
r_d	m	range to discontinuity
r_{max}	m	maximum range
R'	V/(Am)	resistance per unit length
RL	dB	return loss (RL)
r	m	observation point
$S_{i,j}$		scattering parameter from port j to port i
s_{IF}	V	intermediate frequency signal
s_{RX}	V	received signal
s_{TX}	V	transmitted signal
t	s	time variable
t_{mt}	s	total measurement time
T_d		transmission coefficient at discontinuity
T_s	s	sweep time, chirp duration
$\tan \delta_e$		dielectric loss-tangent
$\tan \delta_m$		magnetic loss-tangent
U	V	electric voltage
v_g	m/s	group velocity
v_p	m/s	phase velocity
v_r	m/s	radial velocity
$VSWR$		voltage standing wave ratio
x, y, z		cartesian coordinates
Z_0	V/A	reference impedance
Z_d	V/A	characteristic impedance of discontinuity
Z_{TL}	V/A	characteristic impedance of transmission line

List of Greek Symbols

Symbol	Unit	Description
α	1/m	attenuation constant
β	1/m	propagation constant
γ	1/m	complex propagation constant
Γ		reflection coefficient
Γ_d		reflection coefficient at discontinuity
δ_s	m	skin depth
Δf	Hz	frequency difference
Δf_D	Hz	Doppler frequency difference
Δr	m	range resolution
Δv	m/s	velocity resolution
Δz	m	infinitesimal small length
ϵ	As/(Vm)	permittivity
ϵ'	As/(Vm)	real part of permittivity
ϵ''	As/(Vm)	imaginary part of permittivity
ϵ_r	As/(Vm)	relative permittivity
η	V/A	characteristic impedance
κ	A/(Vm)	electric conductivity
λ	m	wavelength
μ	Vs/(Am)	permeability
μ'	Vs/(Am)	real part of permeability
μ''	Vs/(Am)	imaginary part of permeability
μ_r	Vs/(Am)	relative permeability
ρ	As/m ³	electric charge density
σ	m ²	radar-cross section (RCS)
τ_d	s	round trip time
φ	rad	instantaneous phase
φ_0	rad	initial phase
χ_e		electric susceptibility
χ_m		magnetic susceptibility
ω	1/s	angular frequency

Glossary of Abbreviations and Acronyms

AC	alternating current
ADC	analog-to-digital converter
CAD	computer-aided design
CPW	coplanar waveguide
CT	computed tomography scan
CW	continuous-wave
DAC	digital-to-analog converter
DC	direct current
DDS	direct digital synthesis
DSO	digital storage oscilloscope
DSP	digital signal processing
DTF	distance to fault
DUT	device under test
EMI	electromagnetic interference
FDR	frequency-domain reflectometry
FFT	fast Fourier transform
FM	frequency-modulated
FMCW	frequency-modulated continuous-wave
FSK	frequency shift keying
IF	intermediate frequency
IQ	in-phase and quadrature components
LDO	low-dropout regulator
LED	light-emitting diode
LFM	linear frequency-modulation
LO	local oscillator
NF	noise figure
PCB	printed circuit board
PLL	phase-locked loop
PTFE	polytetrafluoroethylene
radar	radio detection and ranging
RCS	radar cross-section
RF	radio frequency

RMS	root m ean square
RX	receiver, receiving mode
SFCW	stepped-frequency c ontinuous-wave
SFDR	spurious-free d ynamic r ange
SMA	subminiature version A
SNO	super-Nyquist o peration
SNR	signal-to- n oise r atio
SSM	single-sideband m ixer
TDR	time- d omain reflectometry
TE	transverse e lectric
TEM	transverse e lectromagnetic
TL	transmission line
TLUT	transmission line u nder t est
TM	transverse m agnetic
TPC	twisted- p air cable
TUM	Technical University of Munich
TX	transmitter, transmitting mode
VCO	voltage-controlled o scillator
VF	velocity factor
VNA	vector n etwork analyzer
YIG	yttrium iron g arnet

Bibliography

- Aguasca, A., R. Acevo-Herrera, A. Broquetas, J. J. Mallorqui, and X. Fabregas (2013), “ARBRES: Light-weight CW/FM SAR sensors for small UAVs”, *Sensors*, vol. 13, no. 3, pp. 3204–3216.
- Amoli, N. A., S. Sivapurapu, R. Chen, Y. Zhou, M. L. F. Bellaredj, P. A. Kohl, S. K. Sitaraman, and M. Swaminathan (2019), “Screen-printed flexible coplanar waveguide transmission lines: Multi-physics modeling and measurement”, *69th Electronic Components and Technology Conference (ECTC)*, Las Vegas, NV, USA, pp. 249–257.
- Analog Devices, Inc. (2022a), *Datasheet of AD9914*, Wilmington, MA, USA, URL: <http://www.analog.com/en/products/ad9914.html> (visited on 08/08/2022).
- Analog Devices, Inc. (2022b), *Datasheet of ADF4351*, Wilmington, MA, USA, URL: <http://www.analog.com/en/products/adf4351.html> (visited on 08/08/2022).
- Analog Devices, Inc. (2022c), *Datasheet of ADL5801*, Wilmington, MA, USA, URL: <http://www.analog.com/en/products/adl5801.html> (visited on 08/08/2022).
- Anghel, A., G. Vasile, R. Cacoveanu, C. Ioana, and S. Ciochina (2014), “Short-range wide-band FMCW radar for millimetric displacement measurements”, *IEEE Transactions on Geoscience and Remote Sensing*, vol. 52, no. 9, pp. 5633–5642.
- Ash, M., M. Ritchie, K. Chetty, and P. V. Brennan (2015), “A new multistatic FMCW radar architecture by over-the-air deramping”, *IEEE Sensors Journal*, vol. 15, no. 12, pp. 7045–7053.
- Autodesk, Inc. (2022), *PCB Design and Schematic Software EAGLE*, San Rafael, CA, USA, URL: <http://www.autodesk.com/products/eagle/> (visited on 08/08/2022).
- Ayhan, S., S. Scherr, A. Bhutani, B. Fischbach, M. Pauli, and T. Zwick (2016), “Impact of frequency ramp nonlinearity, phase noise, and SNR on FMCW radar accuracy”, *IEEE Transactions on Microwave Theory and Techniques*, vol. 64, no. 10, pp. 3290–3301.
- Balon, S., K. Mouthaan, C. Heng, and Z. N. Chen (2018), “A C-band FMCW SAR transmitter with 2-GHz bandwidth using injection-locking and synthetic bandwidth techniques”, *IEEE Transactions on Microwave Theory and Techniques*, vol. 66, no. 11, pp. 5095–5105.

Bibliography

- Bao, F. (2015), “Sparse Overcomplete Representation Applied to FMCW Reflectometry for Non-Uniform Transmission Lines”, Doctoral Dissertation, Technische Universität München, Germany.
- Bao, F., L. Arend, S. Bertl, and J. Detlefsen (2011), “Application of FMCW radar principle for fast inhomogeneity identification on transmission lines”, *German Microwave Conference (GeMiC)*, Darmstadt, Germany, pp. 1–4.
- Bao, F., A. Kirschner, E. Bluemcke, and J. Detlefsen (2013), “Iterative reweighted l_1 norm deconvolution for localization of mechanical deformation on transmission lines”, *14th International Radar Symposium (IRS)*, Dresden, Germany, pp. 897–902.
- Bao, F., E. Bluemcke, and J. Detlefsen (2014), “Non-negative sparse deconvolution for localization of airbag surface deformations during inflation”, *German Microwave Conference (GeMiC)*, Aachen, Germany, pp. 1–4.
- Beasley, P. D. L., A. G. Stove, B. J. Reits, and B-O. As (1990), “Solving the problems of a single antenna frequency modulated CW radar”, *IEEE International Conference on Radar*, Arlington, VA, USA, pp. 391–395.
- Beaty, H. W. and D. G. Fink (2012), *Standard Handbook for Electrical Engineers*, 16th ed., New York, NY, USA: McGraw-Hill, Inc.
- Bedair, S. S. and I. Wolff (1992), “Fast, accurate and simple approximate analytic formulas for calculating the parameters of supported coplanar waveguides for (M)MIC’s”, *IEEE Transactions on Microwave Theory and Techniques*, vol. 40, no. 1, pp. 41–48.
- Belhaj, M. M., W. Wei, E. Pallecchi, C. Mismer, I. Roch-Jeune, and H. Happy (2014), “Inkjet printed flexible transmission lines for high frequency applications up to 67 GHz”, *44th European Microwave Conference*, Rome, Italy, pp. 1528–1531.
- Bendjaballah, D., A. Bouchoucha, M. L. Sahli, and J-C. Gelin (2017), “Numerical analysis of side airbags deployment in out-of-position situations”, *International Journal of Mechanical and Materials Engineering*, vol. 12, no. 1, pp. 1–9.
- Braver, E. R. and S. Y. Kyrychenko (2004), “Efficacy of side air bags in reducing driver deaths in driver-side collisions”, *American Journal of Epidemiology*, vol. 159, no. 6, pp. 556–564.
- Bronstein, I. N., K.A. Semendjajew, G. Musiol, and H. Mühlig (2001), *Taschenbuch der Mathematik*, 5th ed., Thun and Frankfurt am Main, Germany: Harri Deutsch.
- Brooker, G. M. (2005), “Understanding millimetre wave FMCW radars”, *1st international Conference on Sensing Technology*, Palmerston North, New Zealand, pp. 152–157.

- Bruton, J. T., T. G. Nelson, T. K. Zimmerman, J. D. Fernelius, S. P. Magleby, and L. L. Howell (2016), “Packing and deploying soft Origami to and from cylindrical volumes with application to automotive airbags”, *Royal Society Open Science*, vol. 3, no. 9, p. 160429.
- Cataldo, A. and E. De Benedetto (2011), “Broadband reflectometry for diagnostics and monitoring applications”, *IEEE Sensors Journal*, vol. 11, no. 2, pp. 451–459.
- Chamberlin, K., K. Komisarek, and K. Sivaprasad (1995), “A method-of-moments solution to the twisted-pair transmission line”, *IEEE Transactions on Electromagnetic Compatibility*, vol. 37, no. 1, pp. 121–126.
- Chan, C.-Y. (2007), “Trends in crash detection and occupant restraint technology”, *Proceedings of the IEEE*, vol. 95, no. 2, pp. 388–396.
- Chenakin, A. (2007), “Frequency synthesis: Current solutions and new trends”, *Microwave Journal*, vol. 50, no. 5, pp. 256–260.
- Cook, B. S., J. R. Cooper, and M. M. Tentzeris (2013), “Multi-layer RF capacitors on flexible substrates utilizing inkjet printed dielectric polymers”, *IEEE Microwave and Wireless Components Letters*, vol. 23, no. 7, pp. 353–355.
- Cordesses, L. (2004a), “Direct digital synthesis: A tool for periodic wave generation (part 1)”, *IEEE Signal Processing Magazine*, vol. 21, no. 4, pp. 50–54.
- Cordesses, L. (2004b), “Direct digital synthesis: A tool for periodic wave generation (part 2)”, *IEEE Signal Processing Magazine*, vol. 21, no. 5, pp. 110–112.
- Crandall, C. S., L. M. Olson, and D. P. Sklar (2001), “Mortality reduction with air bag and seat belt use in head-on passenger car collisions”, *American Journal of Epidemiology*, vol. 153, no. 3, pp. 219–224.
- Curtis, A. J. (1961), “Dielectric properties of polyamides: Polyhexamethylene adipamide and polyhexamethylene sebacamide”, *Journal of Research of the National Bureau of Standards. Section A, Physics and chemistry*, vol. 65, no. 3, pp. 185–196.
- Dao, M.-T., D.-H. Shin, Y.-T. Im, and S.-O. Park (2013), “A two sweeping VCO source for heterodyne FMCW radar”, *IEEE Transactions on Instrumentation and Measurement*, vol. 62, no. 1, pp. 230–239.
- Dassault Systèmes (2022), *CST Studio Suite® 2020*, Vélizy-Villacoublay, France, URL: <https://www.3ds.com/products-services/simulia/products/cst-studio-suite/> (visited on 08/08/2022).
- Degerstrom, M. J., B. K. Gilbert, and E. S. Daniel (2008), “Accurate resistance, inductance, capacitance, and conductance (RLCG) from uniform transmission line measurements”, *IEEE-EPEP Electrical Performance of Electronic Packaging*, San Jose, CA, USA, pp. 77–80.

Bibliography

- Detlefsen, J. and U. Siart (2012), *Grundlagen der Hochfrequenztechnik*, 4th ed., Munich, Germany: Oldenbourg Wissenschaftsverlag GmbH.
- Dill, S., E. Schreiber, M. Engel, A. Heinzl, and M. Peichl (2019), “A drone carried multi-channel synthetic aperture radar for advanced buried object detection”, *IEEE Radar Conference (RadarConf)*, Boston, MA, USA, pp. 1–6.
- Drak, O. T. and L. M. Liubina (2021), “Coaxial to microstrip transition matching method”, *IEEE Conference of Russian Young Researchers in Electrical and Electronic Engineering (ElConRus)*, St. Petersburg, Russia, pp. 1252–1255.
- Dubey, A., W. Wang, and R. Murch (2021), “Transmission line fault imaging using phaseless inverse scattering and temporal sparsity”, *IEEE Transactions on Microwave Theory and Techniques*, vol. 69, no. 1, pp. 284–296.
- Eisenstadt, W. R. and Y. Eo (1992), “S-parameter-based IC interconnect transmission line characterization”, *IEEE Transactions on Components, Hybrids, and Manufacturing Technology*, vol. 15, no. 4, pp. 483–490.
- Evelt, S. R. (2003), “Soil water measurement by time domain reflectometry”, *Encyclopedia of Water Science*, Marcel Dekker Inc., New York, NY, USA, pp. 894–898.
- F. Perez-Martinez, M. Burgos-Garcia, and A. Asensio-Lopez (2001), “Group delay effects on the performance of wideband CW-LFM radars”, *IEE Proceedings-Radar, Sonar and Navigation*, vol. 148, no. 2, pp. 95–100.
- Farmer, M. E. and A. K. Jain (2007), “Smart automotive airbags: Occupant classification and tracking”, *IEEE Transactions on Vehicular Technology*, vol. 56, no. 1, pp. 60–80.
- Furse, C. and R. Haupt (2001), “Down to the wire [aircraft wiring]”, *IEEE Spectrum*, vol. 38, no. 2, pp. 34–39.
- Furse, C., Y. C. Chung, R. Dangol, M. Nielsen, G. Mabey, and R. Woodward (2003), “Frequency-domain reflectometry for on-board testing of aging aircraft wiring”, *IEEE Transactions on Electromagnetic Compatibility*, vol. 45, no. 2, pp. 306–315.
- Furse, C., Y. C. Chung, and P. Pendayala (2006), “A critical comparison of reflectometry methods for location of wiring faults”, *Smart Structures and Systems*, vol. 2, no. 1, pp. 25–46.
- Furse, C. M., M. Kafal, R. Razzaghi, and Y. J. Shin (2021), “Fault diagnosis for electrical systems and power networks: A review”, *IEEE Sensors Journal*, vol. 21, no. 2, pp. 888–906.
- Gao, Y. and R. Zoughi (2017), “Millimeter wave reflectometry and imaging for noninvasive diagnosis of skin burn injuries”, *IEEE Transactions on Instrumentation and Measurement*, vol. 66, no. 1, pp. 77–84.

- Gentile, K. (2007), “Super-Nyquist operation of the AD9912 yields a high RF output signal”, *Analog Devices Application Note, AN-939*, URL: <https://www.analog.com/media/en/technical-documentation/application-notes/AN-939.pdf> (visited on 08/08/2022).
- Gilgen, H.H., R.P. Novak, R.P. Salathe, W. Hodel, and P. Beaud (1989), “Submillimeter optical reflectometry”, *Journal of Lightwave Technology*, vol. 7, no. 8, pp. 1225–1233.
- Gomez-Garcia, D., C. Leuschen, F. Rodriguez-Morales, J.-B. Yan, and P. Gogineni (2014), “Linear chirp generator based on direct digital synthesis and frequency multiplication for airborne FMCW snow probing radar”, *IEEE MTT-S International Microwave Symposium (IMS)*, Tampa, FL, USA, pp. 1–4.
- Griffiths, L. A., R. Parakh, C. Furse, and B. Baker (2006), “The invisible fray: A critical analysis of the use of reflectometry for fray location”, *IEEE Sensors Journal*, vol. 6, no. 3, pp. 697–706.
- Gupta, K.C. (1996), *Microstrip Lines and Slotlines*, vol. 2, Norwood, MA, USA: Artech House, Inc.
- Haghzadeh, M., C. Armiento, and A. Akyurtlu (2017), “All-printed flexible microwave varactors and phase shifters based on a tunable BST/polymer”, *IEEE Transactions on Microwave Theory and Techniques*, vol. 65, no. 6, pp. 2030–2042.
- Hasch, J. (2015), “Driving towards 2020: Automotive radar technology trends”, *IEEE MTT-S International Conference on Microwaves for Intelligent Mobility (ICMIM)*, Heidelberg, Germany, pp. 1–4.
- Henderson, B. C. and J. A. Cook (1985), “Image-reject and single-sideband mixers”, *WJ Tech. Note*, vol. 12, no. 3.
- Hiebel, M. (2016), *Fundamentals of Vector Network Analysis*, 7th ed., Munich, Germany: Rohde & Schwarz GmbH & Co. KG.
- Huang, D.-J., J.-L. Kuo, and H. Wang (2012), “A 24-GHz low power and high isolation active quasi-circulator”, *IEEE/MTT-S International Microwave Symposium Digest*, Montreal, QC, Canada, pp. 1–3.
- Hülsmeier, C. (1904), “Verfahren, um entfernte metallische Gegenstände mittels elektrischer Wellen einem Beobachter zu melden”, *German Patent*, vol. 165546, p. 30.
- IEEE (2017), “IEEE Standard for Radar Definitions”, *IEEE Std 686-2017 (Revision of IEEE Std 686-2008)*, pp. 1–54.
- IEEE (2020), “IEEE Standard Letter Designations for Radar-Frequency Bands”, *IEEE Std 521-2019 (Revision of IEEE Std 521-2002)*, pp. 1–15.
- Jankiraman, M. (2018), *FMCW Radar Design*, Norwood, MA, USA: Artech House.

Bibliography

- Jiang, W., S. R. Pennock, and P. R. Shepherd (2012), “FMCW radar range performance improvement with modified adaptive sampling method”, *IEEE Geoscience and Remote Sensing Letters*, vol. 9, no. 4, pp. 668–671.
- Jin, J.-M. (2015), *Theory and Computation of Electromagnetic Fields*, 2nd ed., Hoboken, NJ, USA: John Wiley & Sons.
- Jones, S. B., J. M. Wraith, and D. Or (2002), “Time domain reflectometry measurement principles and applications”, *Hydrological Processes*, vol. 16, no. 1, pp. 141–153.
- Jorgesen, D. (2018), “IQ, image reject, and single-sideband mixer primer”, *Marki Microwave, Inc. Application Note*, URL: https://www.markimicrowave.com/assets/appnotes/IQ_IR_SSB_Mixer_Primer.pdf (visited on 08/08/2022).
- Jung, D.-H., D.-H. Kim, M. T. Azim, J. Park, and S.-O. Park (2021), “A novel signal processing technique for Ku-band automobile FMCW fully polarimetric SAR system using triangular LFM”, *IEEE Transactions on Instrumentation and Measurement*, vol. 70, pp. 1–10.
- Kay, R. and M. Desmulliez (2012), “A review of stencil printing for microelectronic packaging”, *Soldering & Surface Mount Technology*, vol. 24, no. 1, pp. 38–50.
- Keysight Technologies, Inc. (2022), *Advanced Design System (ADS) 2016.01*, Santa Rosa, CA, USA, URL: <https://www.keysight.com/de/de/products/software/pathwave-design-software/pathwave-advanced-design-system.html> (visited on 08/08/2022).
- Khan, M.U. and M. Moatamedi (2008), “A review of airbag test and analysis”, *International Journal of Crashworthiness*, vol. 13, no. 1, pp. 67–76.
- Kim, D.-W., Y. Son, H. Kang, and S. Nam (2022), “Low-spurious wideband DDS-based Ku-band chirp generator for short-range radar application”, *IEEE Microwave and Wireless Components Letters*, vol. 32, no. 3, pp. 206–209.
- Kim, H., G.-Y. Yun, S.-H. Lee, and J.-M. Kim (2015), “High-resolution CPW fabricated by silver inkjet printing on selectively treated substrate”, *Sensors and Actuators A: Physical*, vol. 224, pp. 1–5.
- Knott, E. F., J. F. Schaeffer, and M. T. Tulley (2004), *Radar Cross Section*, 2nd ed., Raleigh, NC, USA: SciTech Publishing, Inc.
- Komarov, I. V. and S. M. Smolskiy (2003), *Fundamentals of Short-Range FM Radar*, Norwood, MA, USA: Artech House.
- Kronauge, M. and H. Rohling (2014), “New chirp sequence radar waveform”, *IEEE Transactions on Aerospace and Electronic Systems*, vol. 50, no. 4, pp. 2870–2877.

- Ku, H. S., J. A. R. Ball, E. Siores, and B. Horsfield (1999), "Microwave processing and permittivity measurement of thermoplastic composites at elevated temperature", *Journal of Materials Processing Technology*, vol. 89, pp. 419–424.
- Lago, A., C. M. Penalver, J. Marcos, J. Doval-Gandoy, A. N. Melendez, O. Lopez, F. Santiago, F. D. Freijedo, J. M. Vilas, and J. C. Lorenzo (2009), "Geometric analysis and manufacturing considerations for optimizing the characteristics of a twisted pair", *IEEE Transactions on Electronics Packaging Manufacturing*, vol. 32, no. 1, pp. 22–31.
- LeCroy Corporation (2022), *WaveMaster 808Zi-A*, Chestnut Ridge, NY, USA, URL: <https://teledynelecroy.com/oscilloscope/wavemaster-sda-dda-8-zi-b-oscilloscopes> (visited on 08/08/2022).
- Lee, C. K., K. S. Kwak, T. S. Yoon, and J. B. Park (2013), "Cable fault localization using instantaneous frequency estimation in Gaussian-enveloped linear chirp reflectometry", *IEEE Transactions on Instrumentation and Measurement*, vol. 62, no. 1, pp. 129–139.
- Lefferson, P. (1971), "Twisted magnet wire transmission line", *IEEE Transactions on Parts, Hybrids, and Packaging*, vol. 7, no. 4, pp. 148–154.
- Li, Q., D. Yang, X. H. Mu, and Q. L. Huo (2012), "Design of the L-band wideband LFM signal generator based on DDS and frequency multiplication", *International Conference on Microwave and Millimeter Wave Technology (ICMMT)*, Shenzhen, China, pp. 1–4.
- Li, Z. and K. Wu (2008), "On the leakage of FMCW radar front-end receiver", *Global Symposium on Millimeter Waves*, Nanjing, China, pp. 127–130.
- Lin, K., Y. E. Wang, C.-K. Pao, and Y.-C. Shih (2006), "A Ka-band FMCW radar front-end with adaptive leakage cancellation", *IEEE Transactions on Microwave Theory and Techniques*, vol. 54, no. 12, pp. 4041–4048.
- Liu, L. and S. Liu (2014), "Remote detection of human vital sign with stepped-frequency continuous wave radar", *IEEE Journal of Selected Topics in Applied Earth Observations and Remote Sensing*, vol. 7, no. 3, pp. 775–782.
- Liu, Y., D. Goshi, K. Mai, L. Bui, and Y. Shih (2009), "Linearity study of DDS-based W-band FMCW sensor", *IEEE MTT-S International Microwave Symposium Digest*, Boston, MA, USA, pp. 1697–1700.
- Lo, C. and C. Furse (2005), "Noise-domain reflectometry for locating wiring faults", *IEEE Transactions on Electromagnetic Compatibility*, vol. 47, no. 1, pp. 97–104.
- Locher, I. and G. Tröster (2007), "Screen-printed textile transmission lines", *Textile Research Journal*, vol. 77, no. 11, pp. 837–842.

Bibliography

- LPKF Laser & Electronics AG (2022), *Protolaser S*, Garbsen, Germany, URL: <https://www.lpkf.com/de/branchen-technologien/forschung-in-house-pcb-prototyping/produkte/lpkf-protolaser> (visited on 08/08/2022).
- Lundstedt, J. (1995), “Condition for distortionless transmission line with a nonuniform characteristic impedance”, *IEEE Transactions on Microwave Theory and Techniques*, vol. 43, no. 6, pp. 1386–1389.
- Lutz, S., D. Ellenrieder, T. Walter, and R. Weigel (2014), “On fast chirp modulations and compressed sensing for automotive radar applications”, *15th International Radar Symposium (IRS)*, Gdansk, Poland, pp. 1–6.
- Mackay, N. A. M. and S. R. Penstone (1974), “A high-sensitivity narrow-band time-domain reflectometer”, *IEEE Transactions on Instrumentation and Measurement*, vol. 23, no. 2, pp. 155–158.
- Mao, Y. and H. Appel (2002), “The influence of different airbag folding patterns on the potential dangers of airbags”, *ATZ worldwide*, vol. 104, no. 5, pp. 26–28.
- Marcuvitz, N. (1951), *Waveguide Handbook*, New York, NY, USA: McGraw-Hill Book Company Inc.
- Matsuhisa, N., D. Inoue, P. Zalar, H. Jin, Y. Matsuba, A. Itoh, T. Yokota, D. Hashizume, and T. Someya (2017), “Printable elastic conductors by in situ formation of silver nanoparticles from silver flakes”, *Nature Materials*, vol. 16, no. 8, pp. 834–840.
- Menicanin, A. B., L. D. Zivanov, M. S. Damnjanovic, and A. M. Maric (2013), “Low-cost CPW meander inductors utilizing ink-jet printing on flexible substrate for high-frequency applications”, *IEEE Transactions on Electron Devices*, vol. 60, no. 2, pp. 827–832.
- Meta, A., P. Hoogeboom, and L. P. Ligthart (2007), “Signal processing for FMCW SAR”, *IEEE Transactions on Geoscience and Remote Sensing*, vol. 45, no. 11, pp. 3519–3532.
- Mikhail, J. N. and D. F. Huelke (1997), “Air bags: An update”, *Journal of Emergency Nursing*, vol. 23, no. 5, pp. 439–445.
- Möhring, B., C. Moroder, U. Siart, and T. Eibert (2019a), “Broadband, fast, and linear chirp generation based on DDS for FMCW radar applications”, *IEEE Radar Conference (RadarConf)*, Boston, MA, USA, pp. 1–4.
- Möhring, B., C. Moroder, U. Siart, and T. Eibert (2019b), “DDS based wideband and fast chirp FMCW radar for tracing discontinuities on transmission lines”, *Photonics & Electromagnetics Research Symposium (PIERS)*, Rome, Italy.

- Möhring, B., C. Moroder, U. Siart, and T. Eibert (2019c), “Transmission line based FMCW radar for localization of airbag surface deformations”, *Kleinheubacher Tagung*, Miltenberg, Germany.
- Möhring, B., U. Siart, S. Schweizer, and T. F. Eibert (2022), “Transmission line based frequency modulated continuous wave radar for monitoring airbag deployment processes”, *18th European Radar Conference (EuRAD)*, London, UK, pp. 481–484.
- Möhring, B. N., U. Siart, and T. F. Eibert (2021), “Fast chirp frequency-modulated continuous-wave reflectometer for monitoring fast varying discontinuities on transmission lines”, *IEEE Transactions on Instrumentation and Measurement*, vol. 70, pp. 1–11.
- Mroz, K. and B. Pipkorn (2007), “Mathematical modelling of the early phase deployment of a passenger airbag-folding using Origami theory and inflation using LS-DYNA particle method”, *6th European LS-DYNA Users’ Conference*, Gothenburg, Sweden, pp. 29–30.
- Muñoz, D, J Carlón, A Negro, A Mansilla, and R Martín (2007), “Application of numerical methods to the simulation of the earliest stages of the airbag deployment”, *ESV Paper*, no. 07-0309, pp. 1–15.
- Nag, A., S. C. Mukhopadhyay, and J. Kosel (2017), “Wearable flexible sensors: A review”, *IEEE Sensors Journal*, vol. 17, no. 13, pp. 3949–3960.
- Naik, S., C. M. Furse, and B. Farhang-Boroujeny (2006), “Multicarrier reflectometry”, *IEEE Sensors Journal*, vol. 6, no. 3, pp. 812–818.
- Nemarich, C. P. (2001), “Time domain reflectometry liquid level sensors”, *IEEE Instrumentation Measurement Magazine*, vol. 4, no. 4, pp. 40–44.
- Nicolson, A. M. and G. F. Ross (1970), “Measurement of the intrinsic properties of materials by time-domain techniques”, *IEEE Transactions on Instrumentation and Measurement*, vol. 19, no. 4, pp. 377–382.
- Orfanidis, S. J. (2016), *Electromagnetic Waves and Antennas*, <http://eceweb1.rutgers.edu/orfanidi/ewa/>, Piscataway, NJ, USA: Rutgers University, New Brunswick, (visited on 08/08/2022).
- Pan, J., G. L. Tonkay, R. H. Storer, R. M. Sallade, and D. J. Leandri (2004), “Critical variables of solder paste stencil printing for micro-BGA and fine-pitch QFP”, *IEEE Transactions on Electronics Packaging Manufacturing*, vol. 27, no. 2, pp. 125–132.
- Pan, T.-W., C.-W. Hsue, and J.-F. Huang (2002), “Time-domain reflectometry using arbitrary incident waveforms”, *IEEE Transactions on Microwave Theory and Techniques*, vol. 50, no. 11, pp. 2558–2563.

Bibliography

- Papazyan, R., P. Pettersson, H. Edin, R. Eriksson, and U. Gafvert (2004), "Extraction of high frequency power cable characteristics from s-parameter measurements", *IEEE Transactions on Dielectrics and Electrical Insulation*, vol. 11, no. 3, pp. 461–470.
- Park, J., S. Park, D. Kim, and S. Park (2019), "Leakage mitigation in heterodyne FMCW radar for small drone detection with stationary point concentration technique", *IEEE Transactions on Microwave Theory and Techniques*, vol. 67, no. 3, pp. 1221–1232.
- Park, J., J.-S. Park, K.-B. Bae, and S.-O. Park (2021), "Advanced stationary point concentration technique for leakage mitigation and small drone detection with FMCW radar", *IEEE Transactions on Microwave Theory and Techniques*, vol. 69, no. 3, pp. 1791–1804.
- Paul, C. R. and J. M. McKnight (1979), "Prediction of crosstalk involving twisted pairs of wires - Part I: A transmission-line model for twisted-wire pairs", *IEEE Transactions on Electromagnetic Compatibility*, vol. EMC-21, no. 2, pp. 92–105.
- Paulter, N. G. (2001), "An assessment on the accuracy of time-domain reflectometry for measuring the characteristic impedance of transmission lines", *IEEE Transactions on Instrumentation and Measurement*, vol. 50, no. 5, pp. 1381–1388.
- Pearlman, J. A., K.G. Au Eong, F. Kuhn, and D. J. Pieramici (2001), "Airbags and eye injuries: Epidemiology, spectrum of injury, and analysis of risk factors", *Survey of Ophthalmology*, vol. 46, no. 3, pp. 234–242.
- Pino, P. (2007), "Intermateability of SMA, 3.5 mm and 2.92 mm connectors", *Microwave Journal*, vol. 10, no. 3, pp. 18–22.
- Piotrowsky, L., T. Jaeschke, S. Kueppers, J. Siska, and N. Pohl (2019), "Enabling high accuracy distance measurements with FMCW radar sensors", *IEEE Transactions on Microwave Theory and Techniques*, vol. 67, no. 12, pp. 5360–5371.
- Piper, S. O. (1993), "Receiver frequency resolution for range resolution in homodyne FMCW radar", *Conference Proceedings National Telesystems Conference*, Atlanta, GA, USA, pp. 169–173.
- Piper, S. O. (1995), "Homodyne FMCW radar range resolution effects with sinusoidal nonlinearities in the frequency sweep", *Proceedings International Radar Conference*, Alexandria, VA, USA, pp. 563–567.
- Porrnzl, M., C. Wagner, H. Jaeger, and A. Stelzer (2015), "An active quasi-circulator for 77 GHz automotive FMCW radar systems in SiGe technology", *IEEE Microwave and Wireless Components Letters*, vol. 25, no. 5, pp. 313–315.
- Pozar, D. M. (2012), *Microwave Engineering*, 4th ed., Hoboken, NJ, USA: John Wiley & Sons, Inc.

- Pulutan, D. K. A. and J. S. Marciano (2013), "Design trade-offs in a combined FMCW and pulse Doppler radar front-end", *IEEE Tencon-Spring*, Sydney, NSW, Australia, pp. 567–571.
- RFspin (2022), "Model DRH400, Double Ridged Waveguide Horn Antenna", URL: <https://www.rfspin.cz/en/antennas> (visited on 08/08/2022).
- Rincon-Mora, G. A. (2009), *Analog IC Design with Low-Dropout Regulators (LDOs)*, New York, NY, USA: McGraw-Hill, Inc.
- Rodriguez-Morales, F., C. Leuschen, C. L. Carabajal, J. Paden, J. A. Wolf, S. Garrison, and J. W. McDaniel (2020), "An improved UWB microwave radar for very long-range measurements of snow cover", *IEEE Transactions on Instrumentation and Measurement*, vol. 69, no. 10, pp. 7761–7772.
- Rohling, H. and M.-M. Meinecke (2001), "Waveform design principles for automotive radar systems", *CIE International Conference on Radar Proceedings*, Beijing, China, pp. 1–4.
- Roos, F., J. Bechter, C. Knill, B. Schweizer, and C. Waldschmidt (2019), "Radar sensors for autonomous driving: Modulation schemes and interference mitigation", *IEEE Microwave Magazine*, vol. 20, no. 9, pp. 58–72.
- Ruff, C., A. Eichberger, and T. Jost (2007), "Simulation of an airbag deployment in out-of-position situations", *Vehicle system dynamics*, vol. 45, no. 10, pp. 953–967.
- Sahu, A., P. H. Aaen, A. Lewandowski, M. Shkunov, G. Rigas, P. T. Blanchard, T. M. Wallis, and V. K. Devabhaktuni (2017), "Robust microwave characterization of inkjet-printed coplanar waveguides on flexible substrates", *IEEE Transactions on Instrumentation and Measurement*, vol. 66, no. 12, pp. 3271–3279.
- Scheiblhofer, S., S. Schuster, and A. Stelzer (2007), "High-speed FMCW radar frequency synthesizer with DDS based linearization", *IEEE Microwave and Wireless Components Letters*, vol. 17, no. 5, pp. 397–399.
- Schiek, B. (1999), *Grundlagen der Hochfrequenz-Messtechnik*, Heidelberg, Germany: Springer-Verlag.
- Schneider, M. (2005), "Automotive radar-status and trends", *German Microwave Conference (GeMiC)*, Ulm, Germany, pp. 144–147.
- Schroeder, C. and H. Rohling (2010), "X-band FMCW radar system with variable chirp duration", *IEEE Radar Conference*, Arlington, VA, USA, pp. 1255–1259.
- Schutt-Aine, J. E. (2001), "High-frequency characterization of twisted-pair cables", *IEEE Transactions on Communications*, vol. 49, no. 4, pp. 598–601.

Bibliography

- Shabany, Y. (2010), *Heat Transfer: Thermal Management of Electronics*, Boca Raton, FL, USA: CRC press.
- Shao, B., R. Weerasekera, L.-R. Zheng, R. Liu, W. Zapka, and P. Lindberg (2008), “High frequency characterization of inkjet printed coplanar waveguides”, *12th IEEE Workshop on Signal Propagation on Interconnects*, Avignon, France, pp. 1–4.
- Sharma, C. R., C. Furse, and R. R. Harrison (2007), “Low-power STDR CMOS sensor for locating faults in aging aircraft wiring”, *IEEE Sensors Journal*, vol. 7, no. 1, pp. 43–50.
- Shin, Y.-J., E. J. Powers, T.-S. Choe, C.-Y. Hong, E.-S. Song, J.-G. Yook, and J. B. Park (2005), “Application of time-frequency domain reflectometry for detection and localization of a fault on a coaxial cable”, *IEEE Transactions on Instrumentation and Measurement*, vol. 54, no. 6, pp. 2493–2500.
- Siebert, W. P. (2003), “High frequency cable connector for twisted pair cables”, *IEEE Transactions on Components and Packaging Technologies*, vol. 26, no. 3, pp. 642–650.
- Simons, R. N. (2001), *Coplanar Waveguide Circuits, Components, and Systems*, New York, NY, USA: John Wiley & Sons.
- Skolnik, M. I. (1990), *Radar Handbook*, 2nd ed., Boston, MA, USA: McGraw-Hill.
- Skolnik, M. I. (2001), *Introduction to Radar Systems*, 3rd ed., Boston, MA, USA: McGraw-Hill.
- Smith, P., C. Furse, and J. Gunther (2005), “Analysis of spread spectrum time domain reflectometry for wire fault location”, *IEEE Sensors Journal*, vol. 5, no. 6, pp. 1469–1478.
- Stove, A. G. (1992), “Linear FMCW radar techniques”, *IEE Proceedings-F (Radar and Signal Processing)*, vol. 139, no. 5, pp. 343–350.
- Stove, A. G. (2004), “Modern FMCW radar - techniques and applications”, *First European Radar Conference (EuRAD)*, Amsterdam, Netherlands, pp. 149–152.
- Strickland, J. A. (1970), *Time-Domain Reflectometry Measurements*, Beaverton, OR, USA: Tektronix, Inc.
- Suganuma, K. (2014), *Introduction to Printed Electronics*, New York, USA: Springer Science + Business Media.
- Teele, D. W. and J. Teele (1984), “Detection of middle ear effusion by acoustic reflectometry”, *The Journal of Pediatrics*, vol. 104, no. 6, pp. 832–838.
- The MathWorks, Inc. (2022), *MATLAB® R2020b*, Natick, MA, USA, URL: <http://www.mathworks.com/products/matlab/> (visited on 08/08/2022).

- Thomas, S. (2006), "Antenna system measurements using frequency domain reflectometry vs. time domain reflectometry", *IEEE International Automatic Testing Conference (AUTOTESTCON)*, Anaheim, CA, USA, pp. 230–236.
- Thurn, K., D. Shmakov, G. Li, S. Max, M. Meinecke, and M. Vossiek (2016), "Concept and implementation of a PLL-controlled interlaced chirp sequence radar for optimized range-Doppler measurements", *IEEE Transactions on Microwave Theory and Techniques*, vol. 64, no. 10, pp. 3280–3289.
- Tierney, J., C. Rader, and B. Gold (1971), "A digital frequency synthesizer", *IEEE Transactions on Audio and Electroacoustics*, vol. 19, no. 1, pp. 48–57.
- Tong, Z., R. Reuter, and M. Fujimoto (2015), "Fast chirp FMCW radar in automotive applications", *IET International Radar Conference*, Hangzhou, China, pp. 1–4.
- Tsai, P., C. Lo, Y. C. Chung, and C. Furse (2005), "Mixed-signal reflectometer for location of faults on aging wiring", *IEEE Sensors Journal*, vol. 5, no. 6, pp. 1479–1482.
- Unger, H.-G. and J. H. Hinken (1991), *Elektromagnetische Wellen auf Leitungen*, 3rd ed., Heidelberg, Germany: Hüthig Buch Verlag GmbH.
- Vanhamme, H. (1990), "High resolution frequency-domain reflectometry", *IEEE Transactions on Instrumentation and Measurement*, vol. 39, no. 2, pp. 369–375.
- Wallis, L. A. and I. Greaves (2002), "Injuries associated with airbag deployment", *Emergency Medicine Journal*, vol. 19, no. 6, pp. 490–493.
- Wenger, J. (2005), "Automotive radar - status and perspectives", *IEEE Compound Semiconductor Integrated Circuit (CSIC) Symposium*, Palm Springs, CA, USA, pp. 21–24.
- Wheeler, H. A. (1942), "Formulas for the skin effect", *Proceedings of the IRE*, vol. 30, no. 9, pp. 412–424.
- Winkler, V. (2007), "Range Doppler detection for automotive FMCW radars", *European Radar Conference (EuRAD)*, Munich, Germany, pp. 166–169.
- Xu, P. and M. C. Hamilton (2013), "Reduced-loss ink-jet printed flexible CPW with copper coating", *IEEE Microwave and Wireless Components Letters*, vol. 23, no. 4, pp. 178–180.
- Xu, Z., T. Kaufmann, and C. Fumeaux (2014), "Wearable textile shielded stripline for broadband operation", *IEEE Microwave and Wireless Components Letters*, vol. 24, no. 8, pp. 566–568.
- Yan, J., D. Gomez-García Alvestegui, J. W. McDaniel, Y. Li, S. Gogineni, F. Rodriguez-Morales, J. Brozena, and C. J. Leuschen (2017), "Ultrawideband FMCW radar for airborne measurements of snow over sea ice and land", *IEEE Transactions on Geoscience and Remote Sensing*, vol. 55, no. 2, pp. 834–843.

Bibliography

- Yang, L., A. Rida, R. Vyas, and M. M. Tentzeris (2007), “RFID tag and RF structures on a paper substrate using inkjet-printing technology”, *IEEE Transactions on Microwave Theory and Techniques*, vol. 55, no. 12, pp. 2894–2901.
- Ybarra, G. A., S. M. Wu, G. L. Bilbro, S. H. Ardalan, C. P. Hearn, and R. T. Neece (1995), “Optimal signal processing of frequency-stepped CW radar data”, *IEEE Transactions on Microwave Theory and Techniques*, vol. 43, no. 1, pp. 94–105.
- Zhang, Q., M. Sorine, and M. Admane (2011), “Inverse scattering for soft fault diagnosis in electric transmission lines”, *IEEE Transactions on Antennas and Propagation*, vol. 59, no. 1, pp. 141–148.
- Zhou, X.-L. and S.-H. Chen (1995), “Theoretical foundation of X-ray and neutron reflectometry”, *Physics Reports*, vol. 257, no. 4-5, pp. 223–348.
- Zinke, O. and H. Brunswig (1965), *Lehrbuch der Hochfrequenztechnik*, Heidelberg, Germany: Springer-Verlag.

Publications by the Author

- Kornprobst, Jonas, Raimund A. M. Mauermayer, Emre Kilic, Björn Möhring, and Thomas F. Eibert (2019), “Improved-accuracy Calderon projector with Rao-Wilton-Glisson discretization for inverse equivalent current methods”, *Photonics & Electromagnetics Research Symposium (PIERS)*, Rome, Italy.
- Möhring, Björn, Markus Limbach, Bernd Gabler, and Alberto Di Maria (2017), “Modular simulation of a compact antenna test range”, *11th European Conference on Antennas and Propagation (EuCAP)*, Paris, France, pp. 2576–2580.
- Möhring, Björn, Clemens Moroder, Uwe Siart, and Thomas Eibert (2019a), “Broadband, fast, and linear chirp generation based on DDS for FMCW radar applications”, *IEEE Radar Conference (RadarConf)*, Boston, MA, USA, pp. 1–4.
- Möhring, Björn, Clemens Moroder, Uwe Siart, and Thomas Eibert (2019b), “Transmission line based FMCW radar for localization of airbag surface deformations”, *Kleinheubacher Tagung*, Miltenberg, Germany.
- Möhring, Björn, Clemens Moroder, Uwe Siart, and Thomas Eibert (2019c), “DDS based wideband and fast chirp FMCW radar for tracing discontinuities on transmission lines”, *Photonics & Electromagnetics Research Symposium (PIERS)*, Rome, Italy.
- Möhring, Björn, Bernd Gabler, and Markus Limbach (2020), “Aircraft antenna placement investigation utilizing measured sources in simulation model”, *Antenna Measurement Techniques Association Symposium (AMTA)*, Newport, RI, USA, pp. 1–4.
- Möhring, Björn, Bernd Gabler, and Markus Limbach (2021a), “Antenna in-situ performance analysis for the hypersonic flight vehicle HEXAFLY: Employing measurement data in a simulation model”, *IEEE Antennas and Propagation Magazine*, vol. 63, no. 4, pp. 89–99.
- Möhring, Björn, Uwe Siart, and Thomas F. Eibert (2021b), “Fast chirp frequency-modulated continuous-wave reflectometer for monitoring fast varying discontinuities on transmission lines”, *IEEE Transactions on Instrumentation and Measurement*, vol. 70, pp. 1–11.

Möhring, Björn, Uwe Siart, Sebastian Schweizer, and Thomas F. Eibert (2022), “Transmission line based frequency modulated continuous wave radar for monitoring airbag deployment processes”, *18th European Radar Conference (EuRAD)*, London, UK, pp. 481–484.

van de Coevering, Leopold G. T., Bernd Gabler, and Björn Möhring (2021), “Improving measurement results by applying hybrid compact range modelling methods”, *15th European Conference on Antennas and Propagation (EuCAP)*, Düsseldorf, Germany, pp. 1–5.

List of Supervised Student Projects

- Klein, J. (2022), "Simulation and design of flexible transmission lines and investigation of bend behavior for airbag surfaces", Master's Thesis, Technical University of Munich.
- Meyer-Giesow, A. (2019), "Investigation of transmission line technologies and their suitability for detecting bends employing a twisted-pair cable", Bachelor's Thesis, Technical University of Munich.
- Moosbühler, M. (2018), "Investigation of twisted-pair transmission lines for the use in FMCW reflectometry", Research Internship, Technical University of Munich.
- Peychev, D. (2017), "An ultra-wideband directional coupler", Bachelor's Thesis, Technical University of Munich.
- Peychev, D. (2019), "Simulation and synthesis of an ultra-wideband directional coupler", Research Internship, Technical University of Munich.
- Pircher, M. (2021), "Characterization and modeling of the compact test range at the German Aerospace Center in Ansys HFSS", Research Internship, Technical University of Munich.
- Steinfeldner, S. (2018), "On the use of passive mixing circuits for frequency multiplication", Bachelor's Thesis, Technical University of Munich.
- Zimmermann, M. (2021), "Design of a frequency-modulated continuous-wave radar system simulator", Research Internship, Technical University of Munich.

